

Award Number: W81XWH-10-1-0741

TITLE: A Brain-Machine-Brain Interface for Rewiring of Cortical Circuitry after Traumatic Brain Injury

PRINCIPAL INVESTIGATOR: Pedram Mohseni, Ph.D.

CONTRACTING ORGANIZATION: Case Western Reserve University  
Cleveland, OH 44106

REPORT DATE: November 2015

TYPE OF REPORT: Final

PREPARED FOR: U.S. Army Medical Research and Materiel Command  
Fort Detrick, Maryland 21702-5012

DISTRIBUTION STATEMENT: Approved for Public Release;  
Distribution Unlimited

The views, opinions and/or findings contained in this report are those of the author(s) and should not be construed as an official Department of the Army position, policy or decision unless so designated by other documentation.

# REPORT DOCUMENTATION PAGE

*Form Approved  
OMB No. 0704-0188*

Public reporting burden for this collection of information is estimated to average 1 hour per response, including the time for reviewing instructions, searching existing data sources, gathering and maintaining the data needed, and completing and reviewing this collection of information. Send comments regarding this burden estimate or any other aspect of this collection of information, including suggestions for reducing this burden to Department of Defense, Washington Headquarters Services, Directorate for Information Operations and Reports (0704-0188), 1215 Jefferson Davis Highway, Suite 1204, Arlington, VA 22202-4302. Respondents should be aware that notwithstanding any other provision of law, no person shall be subject to any penalty for failing to comply with a collection of information if it does not display a currently valid OMB control number. **PLEASE DO NOT RETURN YOUR FORM TO THE ABOVE ADDRESS.**

<b>1. REPORT DATE (DD-MM-YYYY)</b> November 2015			<b>2. REPORT TYPE</b> Final			<b>3. DATES COVERED (From - To)</b> 1 Sep 2010 – 31 Aug 2015		
<b>4. TITLE AND SUBTITLE</b>  A Brain-Machine-Brain Interface for Rewiring of Cortical Circuitry after Traumatic Brain Injury			<b>5a. CONTRACT NUMBER</b>					
			<b>5b. GRANT NUMBER</b> W81XWH-10-1-0741					
			<b>5c. PROGRAM ELEMENT NUMBER</b>					
<b>6. AUTHOR(S)</b>  Pedram Mohseni, PhD Randolph J. Nudo, PhD  pxm89@case.edu			<b>5d. PROJECT NUMBER</b>					
			<b>5e. TASK NUMBER</b>					
			<b>5f. WORK UNIT NUMBER</b>					
<b>7. PERFORMING ORGANIZATION NAME(S) AND ADDRESS(ES)</b>  Case Western Reserve University 10900 Euclid Avenue Cleveland, OH 44106			<b>8. PERFORMING ORGANIZATION REPORT</b>					
			University of Kansas Medical Center Research Institute  3901 Rainbow Boulevard, MSN 1039  Kansas City, KS 66103-2937					
<b>9. SPONSORING / MONITORING AGENCY NAME(S) AND ADDRESS(ES)</b>  US Army Medical Research and Materiel Command Fort Detrick, Maryland 21702-5012			<b>10. SPONSOR/MONITOR'S ACRONYM(S)</b>					
			<b>11. SPONSOR/MONITOR'S REPORT NUMBER(S)</b>					
<b>12. DISTRIBUTION / AVAILABILITY STATEMENT</b>  Approved for Public Release; Distribution Unlimited								
<b>13. SUPPLEMENTARY NOTES</b>								
<b>14. ABSTRACT</b>  A small, lightweight microsystem has been developed for activity-dependent stimulation (ADS) and successfully tested for functionality in both anesthetized and ambulatory rats. Furthermore, in semi-chronic experiments in rats with traumatic brain injury (TBI) using this microsystem, an unprecedented, potent effect of ADS on motor performance has been demonstrated, as compared to control rats (injured but no microsystem) and open-loop stimulation (OLS) rats. Specifically, OLS does result in some recovery after injury, but ADS is significantly more efficacious, resulting in recovery to normal ranges of performance within 2 weeks after injury. Prior to implementation in clinical trials, translation to non-human primates (NHPs) is critical. In the last phase of this study, we finalized the optimal design and partitioning of an NHP microsystem that is small enough to fit inside a custom-designed, skull-mounted, plastic chamber and can continuously operate for two months from a single 1,600mAh battery placed inside a primate jacket. Follow-on support will allow testing of ADS with this new microsystem in the NHP model.								
<b>15. SUBJECT TERMS</b>  Anatomical rewiring; Implantable microsystem; Neuroplasticity; Rehabilitation; Traumatic brain injury								
<b>16. SECURITY CLASSIFICATION OF:</b>			<b>17. LIMITATION OF ABSTRACT</b> UU	<b>18. NUMBER OF PAGES</b> 70	<b>19a. NAME OF RESPONSIBLE PERSON</b> USAMRMC			
<b>a. REPORT</b> U					<b>19b. TELEPHONE NUMBER (include area code)</b>			
<b>b. ABSTRACT</b> U								
<b>c. THIS PAGE</b> U								

Standard Form 298 (Rev. 8-98)

Prescribed by ANSI Std. Z39.18

## Table of Contents

	<u>Page</u>
<b>Introduction.....</b>	4
<b>Body.....</b>	4
<b>Key Research Accomplishments.....</b>	18
<b>Reportable Outcomes.....</b>	18
<b>Conclusion.....</b>	19
<b>References.....</b>	19
<b>Appendices.....</b>	20–24

# A Brain-Machine-Brain Interface for Rewiring of Cortical Circuitry after Traumatic Brain Injury

Principal Investigator: Pedram Mohseni, Ph.D.

*Department of Electrical Engineering and Computer Science, Case Western Reserve University*

Co-Principal Investigator: Randolph J. Nudo, Ph.D.

*Department of Rehabilitation Medicine, University of Kansas Medical Center*

## Introduction

The goal of this project was to use an implantable brain-machine-brain interface to enhance behavioral recovery after traumatic brain injury by reshaping long-range intracortical connectivity patterns. We hypothesized that activity-dependent stimulation (ADS) of distant cortical locations would aid in functional recovery, and that recovery would be correlated with enhanced synaptic facilitation between the two areas. We also hypothesized that spontaneously sprouting axons would migrate toward and terminate in the coupled region, and that such directed sprouting can support recovery (**Figure 1**).

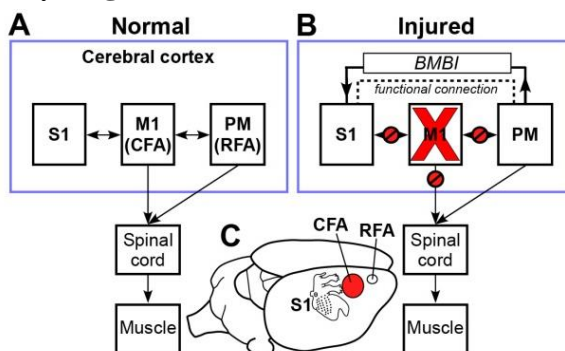


**Figure 1.** Experimental design to record action potentials from the spared premotor area (RFA) and stimulate the somatosensory forepaw area (S1) with ADS after a controlled cortical impact in the primary motor cortex (CFA). From Appendix I: Guggenmos et al., PNAS, December 2013.

## Body

In this section of the final report, we describe the research accomplishments associated with each of the two research thrusts, namely, *Electronics Development / Testing* and *Microsystem Packaging*, for each phase of the project performance period, as well as describe the research accomplishments associated with the *Neurobiology* tasks of the study and collaborative experiments with the team at the University of Kansas Medical Center. The research tasks are outlined in the approved Statement of Work.

### Phase I

#### 1. Electronics Development / Testing

For **Tasks 1.1** and **1.2** in **Phase I**, a fully integrated neural recording front-end comprising a low-noise two-stage amplification circuitry and a 10-bit successive approximation register-based analog-to-digital converter (ADC) was designed and fabricated using the AMS 0.35  $\mu\text{m}$  2P/4M CMOS process. The ac-coupled amplification circuitry provided a maximum mid-band ac gain of  $\sim 66$  dB at 1 kHz and featured a measured input-referred noise voltage of  $\sim 3.1 \mu\text{V}_{\text{rms}}$  from 0.5 Hz to 50 kHz, while dissipating  $\sim 27 \mu\text{W}$  from 1.5 V. **Figure 2** depicts the measured frequency response and input noise voltage of the analog recording front-end for various bandwidth settings. The ADC featured an effective number of bits (ENOB) of 9.2 for sampling frequency of 35.7 kSa/s, while dissipating only 6  $\mu\text{W}$ .

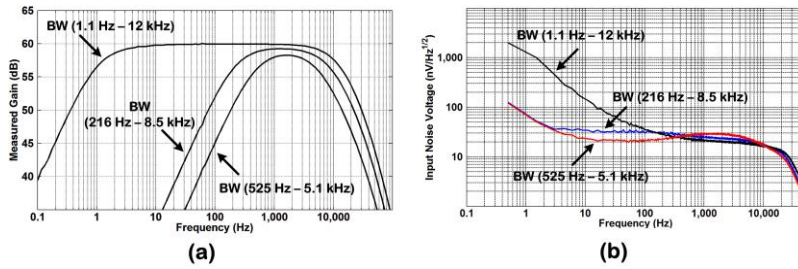


**Figure 2.** Measured (a) frequency response and (b) input noise voltage of the analog recording front-end with different bandwidth settings.

Monolithic circuitry was also designed using standard digital cells to identify the presence of large action potentials in the recorded digitized data with a spike discrimination algorithm based on two programmable threshold levels and time-amplitude windows. A first-order digital highpass filter was also designed to remove any dc/low-frequency artifacts prior to spike discrimination. The measured power consumption per channel was less than 1  $\mu$ W with a 1.5 V supply and ADC sampling frequency of 35.7 kSa/s.

For **Task 1.3** in **Phase I**, an infinite impulse response (IIR) temporal filtering technique for real-time stimulus artifact rejection (SAR) based on template subtraction was developed. A system architecture for the IIR SAR algorithm was also developed, and the operation of the algorithm with fixed-point computation was analyzed to obtain the number of bits for the internal nodes of the system, considering dynamic range and fraction length requirements for optimum performance. Furthermore, memory initialization with the first recorded stimulus artifact was implemented to significantly decrease the IIR system response time, especially when artifacts were highly reproducible in consecutive stimulation cycles. The proposed system architecture was hardware-implemented on a field-programmable gate array (FPGA) and tested using two sets of prerecorded neural data from a rat and an *Aplysia californica* (a marine mollusk) obtained from two different laboratories. Measured results from the FPGA are shown in **Figure 3**, verifying that the system could indeed remove the stimulus artifacts from the contaminated neural data in real-time and recover the neural action potentials that occurred on the tail end of the artifact (as close as within 0.5 ms after the artifact spike). The root-mean-square (rms) value of the pre-processed stimulus artifact was reduced on average by a factor of 17 (*Aplysia californica*) and 5.3 (rat) post-processing. Details of the IIR SAR algorithm, its FPGA implementation and testing with prerecorded neural datasets were reported in Appendix II (Limnuson, et al., *IEEE Trans. Biomed. Circuits and Systems*, June 2014).

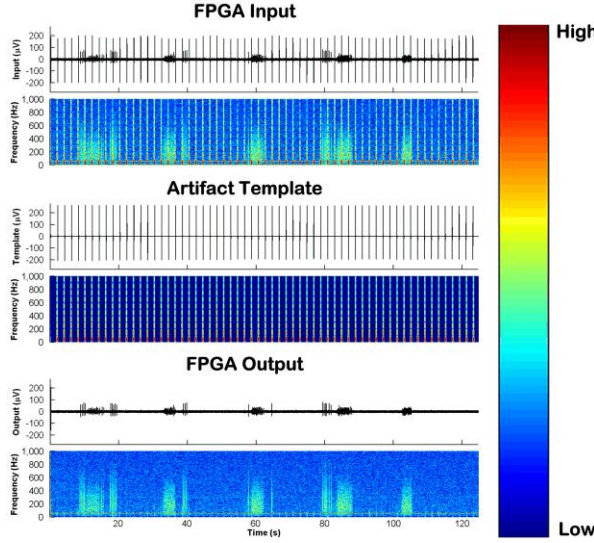


**Figure 3.** FPGA measurement results using the prerecorded *Aplysia* neural dataset and their corresponding spectrograms.

Next, the SAR algorithm was integrated on a second IC that combined spike recording, electrical microstimulation, and real-time SAR for bidirectional interfacing with the nervous system. Fabricated using the AMS 0.35  $\mu$ m 2P/4M CMOS process, the SAR IC integrated a spike-recording front-end with input noise voltage of 3.42  $\mu$ V<sub>rms</sub> (0.5 Hz–50 kHz), microstimulating back-end for delivering charge-balanced monophasic or asymmetric biphasic current pulses up to ~100  $\mu$ A with passive discharge, and  $\mu$ W-level digital signal processing

(DSP) unit for real-time SAR based on template subtraction. The  $3.1 \times 3.1 \text{ mm}^2$  IC was tested via benchtop and biological experiments in isolated buccal ganglia of an *Aplysia californica*.

**Figure 4** shows measurement results from the benchtop tests. With the bandwidth of the analog recording front-end set to 390 Hz–6.4 kHz, the input noise voltage measured in 0.5 Hz–50 kHz was  $3.42 \mu\text{V}_{\text{rms}}$ , resulting in noise efficiency factor (NEF) of 2.75. To evaluate the DSP unit power consumption, two prerecorded neural datasets from a rat (sampled at ~24.41 kHz and obtained during 4 Hz cortical stimulation) and an *Aplysia californica* (sampled at 2 kHz and obtained during 0.5 Hz stimulation) were used. The system clock frequency was set to ~684 kHz and 56 kHz for the rat and *Aplysia* datasets, respectively. **Figure 4** shows the measured DSP unit power consumption versus requisite memory length, when processing each neural dataset for artifact removal. The measured power was in the range of 1.6–2.2  $\mu\text{W}$  for the *Aplysia* neural dataset and increased to 16.1–21.2  $\mu\text{W}$  for the rat neural dataset due to the higher system clock frequency.

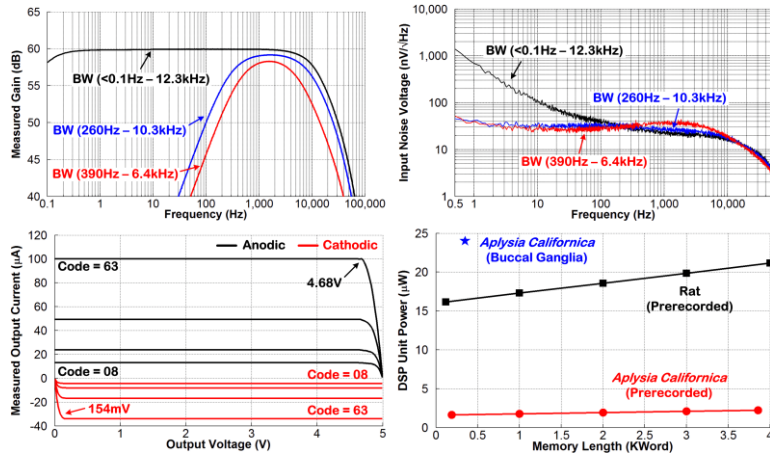


**Figure 4.** Top – Measured gain (left) and input noise voltage (right) of the analog recording front-end. Bottom – Measured microstimulator output current vs. output voltage in anodic and cathodic phases (left) and DSP unit power

The SAR IC functionality was subsequently verified in a neurobiological experiment with isolated buccal ganglia of an *Aplysia californica*. Custom-made hook electrodes were used for external stimulation in buccal nerve 2 (BN2) at 2 Hz and recording from buccal nerve 3 (BN3). The stimulus pulsewidth was 1 ms. Gain and bandwidth of the analog recording front-end were nominally set to maximum value and minimum range, respectively. The DSP unit was programmed for a low cutoff frequency of 366 Hz in the digital highpass filter,  $K$  factor of 1/16 and blanking duration of 2.5 ms synchronized with the rising edge of the *Stimulus Timing* signal. Furthermore, the DSP unit was set to operate for 10 ms in processing each artifact, which closely matched the stimulus artifact duration (obtained *a priori*) to save power consumption. **Figure 5** depicts measured results from the neurobiological experiment, demonstrating that the IC was fully capable of removing large stimulus artifacts in real-time after template subtraction and residual blanking, and recovering the neural spikes that occurred on the tail end of the artifacts (as close as within ~4 ms of stimulus onset). A statistical analysis of 60 recorded artifacts revealed an average rms value of  $143 \mu\text{V}$  and  $6 \mu\text{V}$  for the stimulus artifacts pre- and post-SAR processing, respectively, demonstrating an artifact rejection factor of ~24 by the IC. Details of the IC implementation and its *in vivo* testing were published in Appendix III (Limnuson, et al., *J. Analog Integr. Circ. Sig. Process.*, February 2015).

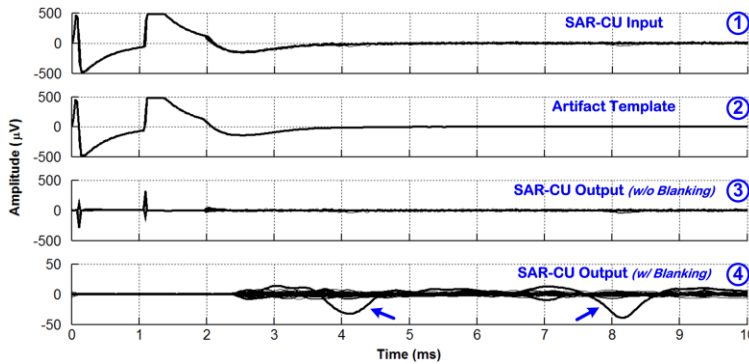


**Figure 5.** Measured results from neurobiological experimentation. Plot #1 shows a 10 ms window of the input data to the SAR IC, showing a total of 62 highpass-filtered stimulus artifacts superimposed, with some (barely visible) neural spikes riding on their tail ends. Plot #2 depicts the 62 stimulus artifact templates generated by the DSP unit and superimposed. Plot #3 shows the SAR IC output signal without blanking, showing significant rejection.

For **Tasks 1.4** and **1.5** in **Phase I**, a decision-making circuitry was implemented as a programmable gate array to provide any logic combination of the four spike discriminator outputs (SDO 1~4) as a trigger signal for stimulation activation using a 16b combination code for each stimulation channel. A high-output-impedance current microstimulator was also designed and fabricated using the AMS 0.35  $\mu\text{m}$  2P/4M CMOS process. It delivered a maximum current of 94.5  $\mu\text{A}$  to the target cortical tissue with current efficiency of 95.6% and voltage compliance of 4.68 V with a 5 V supply, when configured for monophasic stimulation with passive discharge. The programmable microstimulator could also be configured to deliver charge-balanced asymmetric biphasic stimulus with programmable time/amplitude parameters. The stimulus current could be programmed via a 6-bit digital-to-analog converter (DAC) with accuracy better than 1.6 least-significant bit (LSB). **Figure 6** shows the measured microstimulator output current versus the output voltage in the anodic and cathodic phases for four different values of the DAC input code.

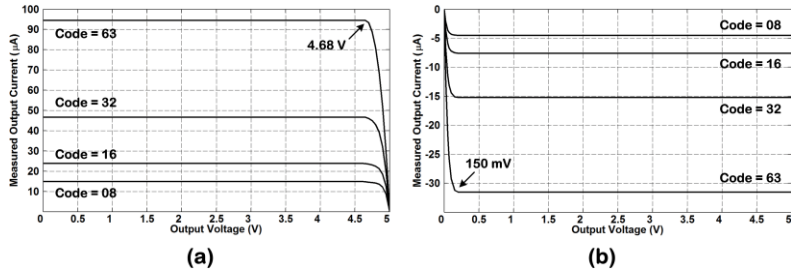


**Figure 6.** Measured microstimulator output current vs. output voltage for four different DAC input codes in a) anodic and b) cathodic phases.

For **Task 1.6** in **Phase I**, a highly integrated voltage converter was designed and fabricated using the AMS 0.35  $\mu\text{m}$  2P/4M CMOS process to generate a 5 V supply for the stimulating back-end from a miniature primary battery (1.5 V) that powers the entire system. The voltage converter employed only one external capacitor (1  $\mu\text{F}$ ) for storage, and delivered a maximum dc load current of  $\sim 88 \mu\text{A}$  with power efficiency of 31% with its output voltage adjusted to 5.05 V. This current drive capability could afford simultaneous stimulation on all eight channels of the system with current amplitude up to  $\sim 100 \mu\text{A}$  and average stimulus rate  $>500 \text{ Hz}$ , which is comfortably higher than firing rate of cortical neurons (up to 150 spikes per second). **Figure 7** shows the measured transient output voltage of the converter with an external storage capacitor of 1  $\mu\text{F}$ , while delivering a dc load current of 10  $\mu\text{A}$ .

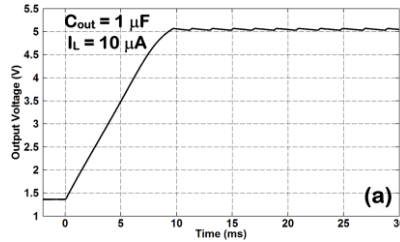


**Figure 7.** Measured transient output voltage of the 1.5-to-5 V converter with a 1  $\mu\text{F}$  external storage capacitor when delivering a dc load current of 10  $\mu\text{A}$ .

For **Task 1.7** in **Phase I**, all electronic circuitry (except for that related to **Task 1.3**) was fabricated using the AMS 0.35  $\mu\text{m}$  2P/4M CMOS process measuring  $3.3 \times 3.3 \text{ mm}^2$ . Details of circuit and system architectures along with more in-depth electrical performance characterization results were reported in [1]. Details of *in vivo* measurement results with intact, anesthetized rats for **Task 1.1** in **Phase II** were also reported in [1].

## 2. Neurobiology

For **Task 2.1** in **Phase I**, prior to the initiation of animal experiments, we obtained protocol approval for rodent studies from our local Institutional Animal Care and Use Committee (07/20/10) and subsequently from

For **Task 2.2 in Phase I**, we developed a paradigm for testing neurophysiological changes within pre-motor cortex (PM) of the rat (RFA, rostral forelimb area) resulting from distant stimulation within several regions of somatosensory cortex to assess the synaptic efficacy of our activity-dependent stimulation (ADS) paradigm. For this set of experiments, a commercial neural recording/stimulation system (Tucker-Davis Technologies (TDT), Alachua, FL) was used for ease and flexibility of programming the various experimental conditions, allowing us to complete this task in parallel with microdevice development tasks at Case Western Reserve University. Verification of our ability to record action potentials from single neurons (spikes) and stimulate different cortical fields was completed using commercial equipment in intact, anesthetized rats. Intracortical microstimulation (ICMS) was used to determine the functional boundaries of RFA and the caudal forelimb area (CFA). Multi-unit recording techniques were used to determine sensory fields in S1. A stimulating electrode was implanted into the RFA. A recording electrode was introduced in CFA as well as control locations. For each recording electrode location in CFA we were able to discriminate spikes based on the same time-amplitude window discrimination algorithm to be programmed into the microdevice. We recorded spontaneous firing rates for five minutes to define baseline rates. Then, spike activity in CFA was recorded during single-pulse stimulation in RFA for 1000 pulses. This resulted in successful spike discrimination of both spontaneous and stimulus-evoked activity.

To facilitate this testing, we developed an experimental design wherein one hour periods of stimulation were interspersed with 10 minute basal periods in which no stimulation was given (**Figure 8**). For each subject, a 4x4, 16-channel Michigan electrode (NeuroNexus, Ann Arbor, MI) was inserted into layer V of RFA and a 1x16 16-channel Michigan electrode was inserted into somatosensory cortex. During the first basal period, a “trigger” neuron was identified within RFA that had a strong signal to noise ratio (based on peak-to-peak spike amplitudes) and a clear spike profile with an appropriate firing rate, between 5-30Hz.

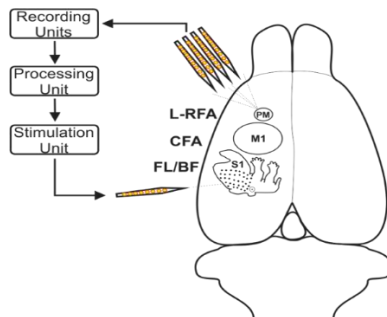


**Figure 8.** Experimental paradigm for assessing changes in electrophysiological response related to stimulation. Neural activity was recorded within RFA and stimulation was delivered into different regions of somatosensory cortex depending on group assignment.

In groups receiving ADS, detection of the “trigger” neuron’s spike profile would lead to a stimulation pulse within somatosensory cortex after a set-delay. Further, there was a software limiting “blanking” period in which detected trigger spikes would not induce stimulation to limit the likelihood of forming a runaway positive feedback loop resulting from detected stimulus artifact at the recording site. This blanking period also allowed for a period following stimulation that could be compared across all groups. Neural spikes of several ADS animals were analyzed for mean firing rate distribution of inter-spike intervals. Based on this data, control animals received random (non-neural activity linked) stimulation (RS), programmed to be triggered randomly, but at intervals normally distributed around the ADS trigger mean-firing rate (~7Hz). The stimulation had the same delay and blanking constraints as the ADS group: stimulation would occur after a programmable delay and no stimulation could occur, even if triggered, during the blanking period.

Based on programmatic limitations of the developed microdevice, namely the timing between threshold crossing for the initiation of spike detection through the decision logic, delay, and blanking period was required to be less than 28ms total duration. To test delay periods that were possible within the microdevice circuitry, we opted to start experimentation with a 10ms spike-stimulus delay, and an 18ms post-stimulus time period. This time period was within the optimal delay period described by Jackson et al. [2] for inducing changes in motor output properties within M1 of the macaque using ADS.

We initially acquired data on four groups of rats using the 10ms delay, ADS in S1 forelimb area (FL), N=6, ADS in S1 barrel field (BF), N=5, random stimulation in FL, N=5, and random stimulation in BF, N=5. All neural activity was bandpass-filtered between 0.3-5kHz, digitized and stored for off-line analysis. Time stamps of trigger neurons in all cases were recorded, as well as the time stamps when stimulation was delivered. Time stamps were also recorded between the basal and stimulation phases of each experiment to allow for filtering based on these parameters. The filtered data was then processed offline to find neural spike profiles and time stamps, using either commercial (OpenSorter, TDT) or custom spike detection software. Due to the duration of the recording sessions, the influence of the stimulation artifact, and the number of channels, significant effort was devoted to developing automated algorithms for spike detection and sorting for analysis of this data set [3]. Using data recorded for this task, we were able to improve spike detection accuracy rates from 90.9% using the TDT commercial spike detection to 97.3% using custom spike detection during the basal periods, and from 93.5% to 97.2% during stimulation phases.

For **Task 2.3 in Phase I**, we used spike timing data collected in Task 2.2 to perform a number of analyses to assess changes in the electrophysiological properties of neurons within RFA as a result of ADS. We investigated these properties in a number of ways. Examining spikes recorded during the blanking period, we first determined the evoked response to the delivered stimulation. The time stamps of all stimulations were used to generate post-stimulus time histograms for all periods 28ms after stimulation (corresponding to the blanking period plus delay of the shortest possible stimulus-stimulus latency; **Figure 9**).

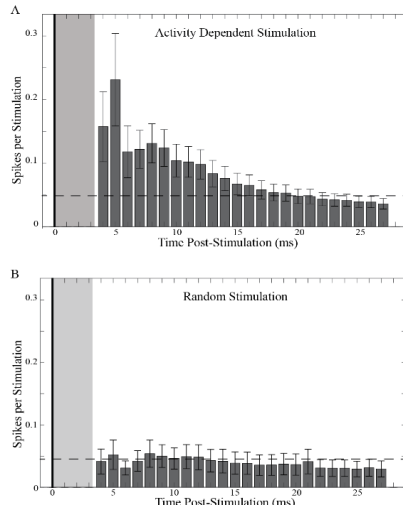


**Figure 9.** Normalized post-stimulus time histograms for ADS (top) and RS (bottom). ADS shows increased probability of spiking within RFA following stimulation, especially within 10ms of stimulus onset (unpublished).

The first three milliseconds post-stimulus were eliminated due to the presence of stimulus artifact. Stimulus-associated spikes, calculated as the mean number of spikes per stimulus, were used to allow inter-session comparison by normalizing for the total number of stimulus pulses delivered across sessions. All spike profiles recorded were used to calculate the mean spikes per stimulus subdivided into 1ms bins. In the ADS condition, the data indicated a distinct peak above baseline firing rates within the first 10ms following stimulus onset, and a return to baseline firing rates by the end of the 28ms. In contrast, there was minimal increase above baseline in the random stimulation (RS) condition.

To further explore this relationship, we then examined differences in the activity-dependent stimulation-evoked activity between BF and FL. As shown in **Figure 10**, it appears that there is a strong effect in the location in which ADS is delivered, with facilitation of activity when stimulation was applied to BF, and suppression when stimulation was applied to FL. These data suggest that ADS promotes excitatory connectivity between RFA and BF, but potentially an inhibitory one between RFA and FL. Because of the spatial arrangement of the Michigan electrode, it was also possible to assess the evoked activity across a region of RFA. For both conditions, there was a negative relationship of the probability of ADS evoked activity and the distance from the trigger channel. This may indicate some degree of specificity in the response with RFA to the stimulation based on the location of the neuron triggering that stimulation (**Figure 11**).

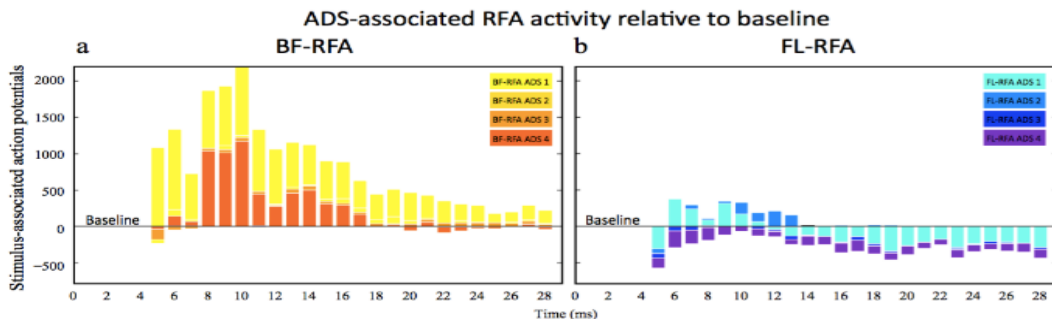


**Figure 10.** Cumulative ADS evoked spikes of BF and FL relative to the activity of the non-stimulation periods in a subset of  $n=4$  animals for each group (Van Acker, et al., in preparation).

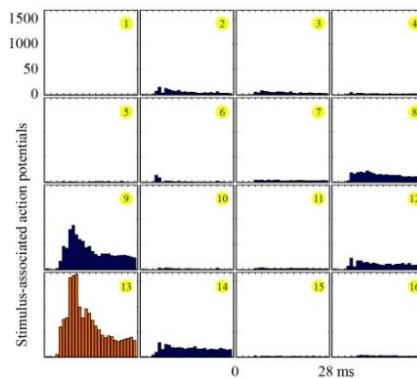


**Figure 11.** Specificity of short latency facilitation in RFA by ADS in S1. Channel 13 was used for triggering ADS, and synaptic facilitation was greatest on that channel (Van Acker et al., 2015).

In summary, it appears that ADS can induce activity in neurons within RFA immediately after the stimulation, with a stronger effect the closer the neuron is to the trigger site. While the general trend for ADS was induction of activity, the area that was stimulated had a dramatic effect on the overall rates of activity while the stimulation was occurring. In this case, of animals with an intact cerebral cortex, stimulation of the somatosensory barrel fields led to increased activity related to baseline periods, but stimulation of the forelimb area of somatosensory cortex decreased the activity relative to baseline. Further, based on the basal firing rates of the four conditions, RFA was more amenable to alterations in rate and patterns of activity resulting from stimulation of BF (either through ADS or RS). This information indicates that the location of stimulation has a significant contribution to the activity recorded in RFA. The ability to manipulate cortico-cortical connections using ADS is dependent on many factors, including the degree to which reciprocal inhibitory and excitatory connections exist between the recorded and stimulated areas. When connections are disrupted as a result of CCI injury, communication is fundamentally altered between cortical regions. It is still unclear what the interplay of existing neural communication has on ADS functionality. While timing surely plays a factor in effectiveness of ADS, it appears that the choice of recording and stimulation locations plays a significant factor in successful manipulation of neural activity.

While the initial goal of these experiments was the optimization of spike-stimulus delays, the rapid potentiation found with ADS, but not open-loop stimulation (OLS), demonstrated that we could examine many parameters in anesthetized preparations relatively quickly. Functional connectivity was enhanced within hours in an anesthetized rat after controlled cortical impact. Several other ancillary results have shed insight into the specificity of these effects, both at the level of the cortical area of interest, as well as the specific set of neurons used to trigger the stimulation.

## Phase II

### 1. Electronics Development / Microsystem Packaging

For **Tasks 2.1** to **2.4** in **Phase II**, a miniature rigid-flex substrate was fabricated through Flexible Circuit Technologies (Plymouth, MN). The integrated circuit (IC) that was developed in **Phase I** was assembled on the 4-layer substrate made from FR-4 (rigid) and polyimide (flexible) sections, together with various other

components. We worked with ProtoConnect (Ann Arbor, MI) for die attachment, encapsulation, wire bonding, and assembly of all the components onto the substrate. The microsystem was designed to connect to two chronically implanted recording and stimulating microelectrodes (NeuroNexus Technologies, Ann Arbor, MI) via two microconnectors (Omnisys Corp., Minneapolis, MN) in plug-and-play fashion. The microelectrodes were not permanently connected to the microsystem in order to allow replacing the microsystem in case of failure or reusing it for additional experiments. The flexible polyimide interconnect between the microelectrode connectors and the rigid substrate could partially compensate for slight misplacement of the microelectrodes during implantation, simplifying the surgical procedure for electrode placement. **Figure 12** depicts the schematic block diagram and a photograph of the fully assembled microsystem. **Figure 13** verifies the *in vivo* functionality of the microsystem in the brain of an ambulatory rat. Specifically, spike waveforms that were discriminated in real-time from the rostral forelimb area (RFA) region triggered single-pulse stimulation in the second somatosensory area (SII), leading to the presence of large stimulus artifacts on the recording microelectrode after a user-set spike-stimulus delay of 5 ms. Details of the microsystem design and assembly/packaging along with measurement results from both anesthetized and ambulatory rats were reported in Appendix IV (Azin, et al., *IEEE Trans. Biomed. Eng.*, September 2011).

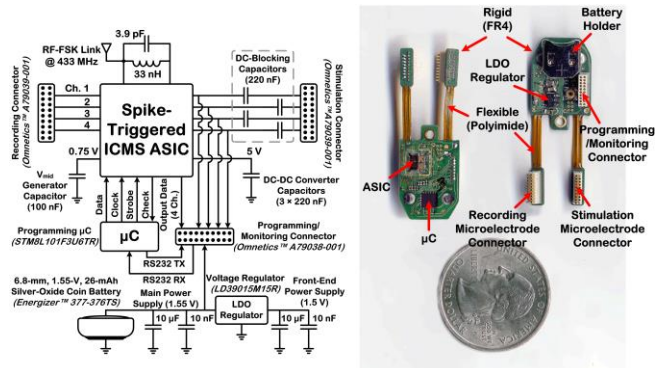


**Figure 12.** Schematic block diagram and a photograph of the fully assembled microsystem for activity-dependent intracortical microstimulation in an ambulatory rat.

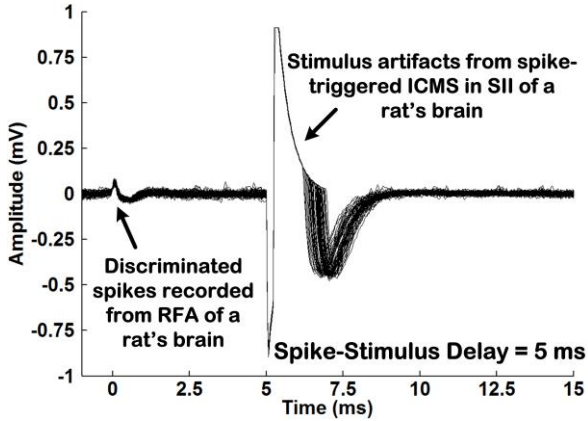


**Figure 13.** Stimulation on the microelectrode implanted in the SII triggered by neural spikes discriminated on the electrode implanted in the RFA with a spike-stimulus time delay of 5 ms.

We conducted *in vivo* testing of the microsystem developed at CWRU, and these results were reported in [1]. As soon as the fully assembled microsystem was available from CWRU, *in vivo* experiments were conducted in brain-injured rats. We tested our ability to successfully implant the device chronically in an injured rat, record spikes from implanted electrodes, and stimulate a remote area. We were successful in generating ADS delivered to the somatosensory cortex with an externally mounted microdevice (**Figure 14**). In pilot rats, we examined the effects of the implanted device in ambulatory rats that had sustained a controlled cortical impact in CFA. Recording electrodes were implanted in RFA, while the stimulating electrode was implanted in the somatosensory forepaw field. As in uninjured rats, we were able to demonstrate functionality of the microdevice in an ambulatory rat who had sustained a controlled cortical impact to CFA. The maximum delay for the initial

microdevice was 28 ms. Thus, it was decided that the initial treatment studies were to be conducted using a 28 ms delay.

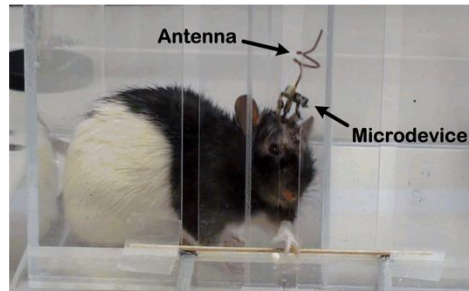


**Figure 14.** Ambulatory rat with microdevice in place. Rat is reaching for a food pellet through a slot in a Plexiglas barrier. Normal rats achieve approximately 80% successful retrievals during an assessment session. In rats with a controlled cortical impact to CFA, motor performance is poor and rats rarely achieve more than 20% success at the task.

For **Task 1.2** in **Phase II**, *in vivo* experiments were performed in a total of 16 rats that had received controlled cortical impact (CCI) over the forelimb area of the primary motor cortex to simulate a TBI (Tasks 3.1-3.11 in *Neurobiology*, below). ADS was generated continuously for 28 days by the fully assembled microsystem powered with a 1.5 V battery. As seen in **Figure 15**, within one week post-injury, while receiving ADS, rats showed substantially improved reaching and grasping functions as compared to control rats (injured but no microsystem) and open-loop stimulation (OLS) rats. These functions were indistinguishable from pre-lesion levels (dotted line) by two weeks post-injury. These findings showing rapid recovery of motor abilities in rats implanted with the microsystem were published in the journal *Proceedings of the National Academy of Sciences* (PNAS, see Appendix II, Guggenmos, et al., December 2013). During the ensuing weeks, the study attracted considerable attention from various news agencies and technology leaders in the microelectronics field, and was featured on the CDMRP's own website.

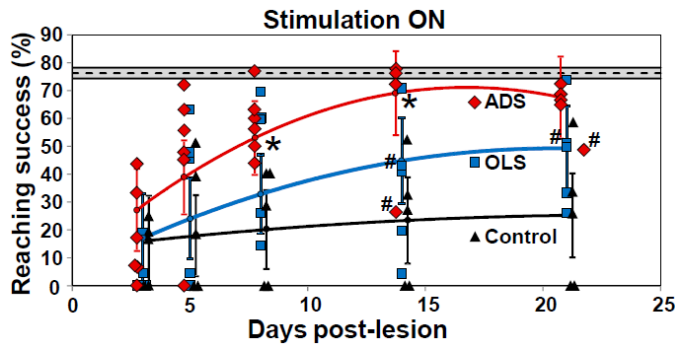


**Figure 15.** Performance of rats on a skilled reaching task after injury to primary motor cortex. ADS group is shown in red, OLS group in blue, and control group in black.

### 3. Neurobiology

**Tasks 3.1 – 3.11 (Phase II)** represented the core experiment of the project to test the ability of ADS between RFA and S1 to improve motor recovery after a controlled cortical impact injury to motor cortex. The behavioral results of this study were summarized above under *Electronics Development/Microsystem Packaging*. The individual tasks (3.1-3.11) represent various steps in the protocol describing injury induction, baseline testing, microelectrode implantation, randomization of rats to ADS and OLS and control groups, assessment of behavioral and physiological outcomes, explantation of microelectrodes, and euthanasia.

Male Long-Evans rats were randomly assigned to one of two groups: ADS, random, OLS or no stimulation (Unimplanted Control). Each animal was put into a Plexiglas reaching chamber and a single banana-flavored food pellet was placed into a shallow food well on an external shelf. The opening of the chamber was such that only the left forelimb could be used for reaching. Prior to entry into the remainder of the study, the animal was required to reach and retrieve food pellets above 70% success for three consecutive days. Probe trials occurred on Post-Lesion Days (PLD) 3, 5, 8, 14, 21 and 28 and consisted of 20 trials with microdevice stimulation on and 20 trials with microdevice stimulation off.

Under anesthesia, a midline incision was made to expose the skull surface, then a 5-mm trephine hole was made over the right hemisphere using stereotaxic coordinates to expose the CFA RFA, and the forepaw area of S1 in the right hemisphere using stereotaxic coordinates. The RFA and S1 areas were then isolated using electrophysiological mapping techniques. After defining RFA and S1, a controlled cortical impact was delivered to CFA using the Impact One stereotaxic impactor (Leica Microsystems). The impact was delivered via a flat, circular tip with a 3-mm diameter, using parameters outlined in our published study [4]. A 16-channel Michigan electrode (NeuroNexus Technologies) was inserted into RFA and another electrode was inserted into S1. Any remaining exposed areas were covered with the silicone polymer before suturing the incision.

The microdevice was then affixed to a threaded rod with stainless steel nuts and spacers, and its connectors plugged into the appropriate electrodes. Two to four hours following the microdevice implantation, a 1.55-V battery was inserted into the microdevice. An Omnetics connector leading to a custom-built controller board was plugged into the microdevice, and the microdevice was initially programmed to record on all four available channels. Once spike discrimination parameters were defined, they were imported into the microdevice programming software. Stimulation parameters were also set in the software to a 60- $\mu$ A current delivered pseudobiphasically with pulse duration of 192  $\mu$ s. For the ADS group, stimulation was set to occur 28 ms following spike discrimination on the channel from which the parameters were derived. The microdevice was then programmed to transmit the data wirelessly, and the animal was allowed to move freely about its cage during the 28 day recovery period.

The results demonstrated a potent effect of ADS on motor performance after only 5 days of operation. By Day 14 post-lesion, performance in the ADS group was indistinguishable from pre-lesion performance (~75%; **Figure 15**). These results demonstrate that ADS between the spared premotor cortex (i.e., the RFA) and the somatosensory forepaw area (S1) can result in a rapid improvement in motor function in the first week post-lesion. This is the first demonstration that ADS can be used to positively affect function after cortical injury. Our neurophysiological results also showed that ADS resulted in strong, short-latency facilitation of the corticocortical pathway between S1 and RFA (Appendix II, Guggenmos, et al., December 2013).

### **Phase III**

#### **1. Electronics Development**

For **Tasks 1.1** and **1.2** in **Phase III**, considerations of differences in non-human primate to rodent anatomy and physiology were needed to identify parameter ranges necessary for the non-human primate microdevice. In rodents, evoked motor responses can be elicited from the premotor region using stimulation pulses with current levels varying from 1  $\mu$ A to 80  $\mu$ A, which was used, in part, as the rationale for having <100  $\mu$ A of stimulus intensity in the rodent IC. In non-human primates, evoked motor responses in the premotor regions can be elicited using much lower current levels, up to 30  $\mu$ A in the squirrel monkey [5]. In this case, the rodent IC had more than enough headroom to stimulate non-human primate motor circuits. Furthermore, in the rodent IC, the range of spike-stimulus time delay was chosen based on the estimated transmission time (assuming a minimum of 2.9 m/s transmission propagation speed of layer V motor neurons [6], 1 or 2 synapse transmission (2 ms to 3 ms per synapse) and a corticocortical transmission distance of 5 mm), leading to a physiologically relevant delay between premotor region activity and sensory cortex stimulation. While the distance between premotor regions and area 3a/3b of the sensory cortex in the squirrel monkey is significantly larger than that in the rodent at ~1.2 cm, the conduction velocity is likely significantly faster. Hence, the time delay range (< 29 ms) of the rodent IC was sufficient for physiologically relevant time delays in the squirrel monkey. As the primary adjustable parameters for ADS in the rodent IC were sufficient or superior for use in the non-human primate, the rodent IC was used in subsequent development of the primate microdevice.

#### **2. Microsystem Packaging**

For **Tasks 2.1** and **2.2** in **Phase III**, efforts were focused on modifying the microsystem assembly and packaging for ambulatory experiments with non-human primates. Specifically, the goal was to fit the revised microsystem inside a custom-designed plastic chamber with dimensions of ~ 2.4 × 2.4 × 1.8 cm<sup>3</sup> that would be mounted to the skull of a squirrel monkey with stainless steel skull screws and affixed with dental acrylic. Power was delivered to the head-mounted microsystem from a backpack device enclosed in a casing with dimensions of ~ 6 × 3.5 × 2 cm<sup>3</sup> and embedded within a primate jacket. The backpack device incorporated a lithium-thionyl-

chloride battery (3.6 V) with a capacity of 1,600 mAh, electronic components for power management, a microcontroller unit (MCU), and an ANT radio module (ANT Wireless, Alberta, Canada). Since the primate microsystem had to be enclosed within the skull-mounted chamber during the behavioral studies, and the squirrel monkeys would be freely moving in their home cages, the microsystem could not be tethered to equipment for programming/monitoring, even on a temporary basis. The low-power, small-sized, 2.4 GHz ANT radio module would instead establish a stable, bidirectional, wireless link between the microsystem and a home-base computer for programming the head-mounted microsystem and monitoring its operation status (e.g., battery voltage, stimulus site impedance, and average stimulus rate). Efforts were then focused, and are still continuing, on firmware design to develop codes for the two microcontrollers on the microsystem and an external receiver board to allow bidirectional communication between the microsystem and the home-base computer via the ANT radio module.

**Figure 16** shows the system architectures for the head-mounted and backpack devices placed within the skull chamber and primate jacket, respectively. To increase battery lifetime (estimated to be ~60 days), the backpack device employed a commercial dc-dc converter and low-dropout (LDO) regulator to generate the power supply for the ANT radio module (2.1 V) and MCU (1.8 V). The head-mounted device also included a commercial, low-power, low-voltage MCU that programmed the IC during power-up and then would go into a halt mode to reduce the static power consumption. Three LDO regulators would generate the power supply for the MCU (1.8 V), analog (1.5 V), and digital (1.5 V) circuitry of the IC in the head-mounted device. The head-mounted and backpack devices could communicate via a biocompatible, flexible, 4-conductor wire (ground, 2.1 V, DATA\_TX, DATA\_RX), shielded in a flexible, biocompatible, spiral conduit and tunneled subcutaneously.

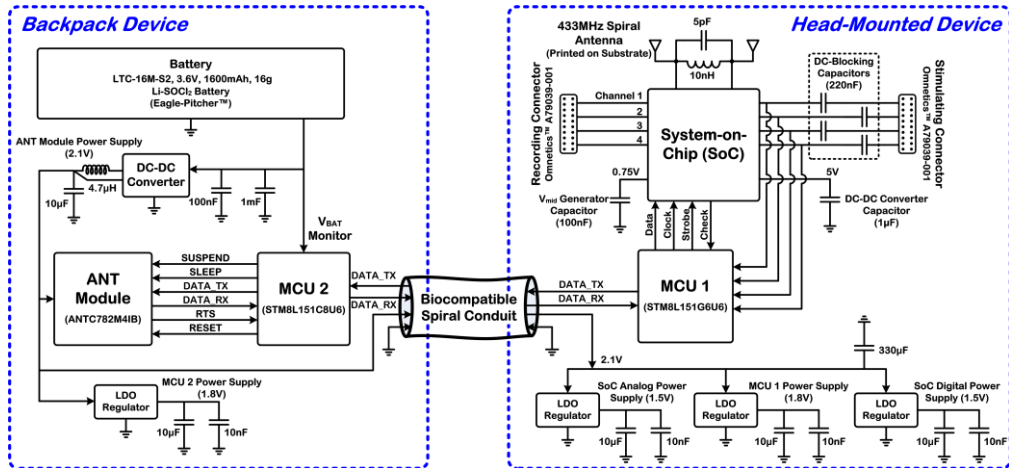


**Figure 16.** Architecture of head-mounted and backpack devices for primate microsystem.

### 3. Neurobiology

For **Task 3.1 and 3.2 (Phase III)**, we sectioned the tissue and calculated the lesion volumes for the efficacy study described above. **Task 3.3, 3.4 and 3.5** focused on anatomical changes using histological stains to identify tract-tracers. Tract-tracing in unimplanted CCI (and uninjured healthy) rats was straight-forward. We did extensive analysis of the control cases, and we were able to reconstruct in tangential sections the anatomical connectivity patterns of the RFA with other cortical areas (**Figure 17**). A full manuscript was submitted to *Cerebral Cortex*, and is currently under revision. We encountered a problem in the histological processing of implanted animals that is attributable to the presence of the electrode arrays and their removal prior to tracer injection. Analysis of rats with CCI injuries, but no ADS treatment, will be completed using internal KUMC endowment funding. However, it is possible that axonal growth and connectivity will not occur over this short time period. Such long-range rewiring is likely to require several weeks to a few months. The rapid recovery we observed during the efficacy study described above suggests that the microdevice serves as a functional communication bridge between the cortical areas, at least within the first few weeks of operation. Nevertheless, we are continuing with the study of corticocortical connections after injury to determine natural sprouting patterns

and rates of connectivity. **Task 3.6**, conducting the regulatory review and approval of the protocol for non-human primates was completed. Full approval by the local IACUC and by ACURO was completed. In addition, an on-site inspection of the non-human primate facilities was conducted by a DoD veterinarian, and was approved.

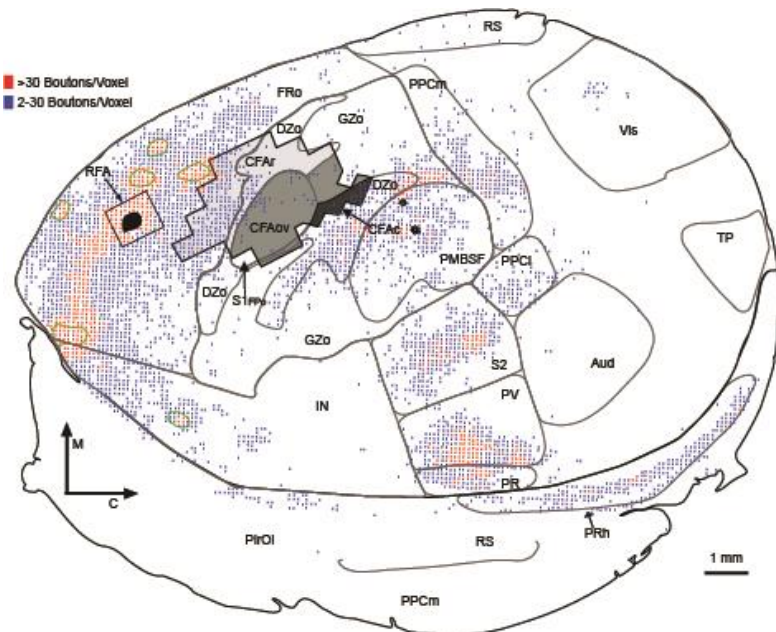


**Figure 17.** Spatial distribution of labeled synaptic boutons following injection of the neuronal tract-tracer, biotinylated dextran amine, into RFA in a healthy, uninjured rat. A single 50 micron thick, tangential section in the middle layers of cortex is shown (Urban et al., under revision).

#### **Phase IV**

##### **1. Electronics Testing/Microsystem Packaging**

For **Task 1.1** in **Phase IV**, **Figure 18** shows an illustration of the skull-mounted plastic chamber enclosing the non-human primate microsystem. With internal dimensions of  $18 \times 18 \text{ mm}^2$ , the chamber that molded to the skull curvature and spanned the cranial opening was designed to surround the fixed electrode connectors. This chamber would serve both to protect the opening and electrodes, and to secure the microsystem. The chamber was mounted to the skull within the border of embedded skull screws and affixed with dental acrylic. The microsystem power leads routed through a hole in the chamber and subcutaneously tunneled to the mid-scapular region of the back and into a previously installed primate jacket. These leads could be connected to a large-capacity battery pack held within the jacket. Inside the chamber, the primate microsystem was designed to connect to two multi-site, chronically implanted recording and stimulating microelectrodes (NeuroNexus Technologies, Ann Arbor, MI) via two microconnectors (Omnetics Corp., Minneapolis, MN) in plug-and-play fashion, and was then screwed into place on mounting posts inside the chamber walls. After the power leads were attached to the microsystem, the chamber lid was screwed into place, securing all embedded microelectronic circuitry. As stated above, efforts were focused, and are still continuing, on developing software tools and firmware codes to allow bidirectional wireless communication between the fully enclosed microsystem and the home-base computer for programming and operation monitoring. Follow-on support from the Joint Warfighter Medical Research Program (JWMRP, award log# JW150028) will allow ADS testing with this microsystem in the non-human primate model.

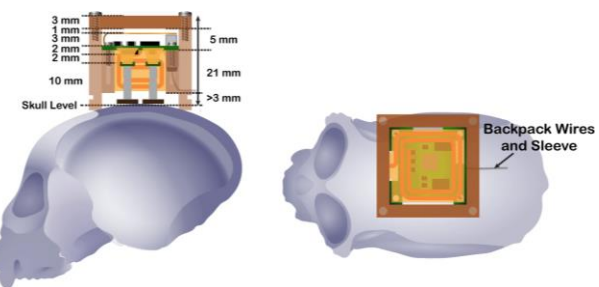


**Figure 18.** Illustration of skull-mounted plastic chamber enclosing non-human primate microsystem.

## 2. Neurobiology

**Tasks 2.1-2.10 (Phase IV)** comprised the various steps in the protocol for the non-human primate study. The full efficacy study was postponed due to two issues: 1) The non-human primate microdevice will need to undergo additional revisions in the structural design in order to be attached to the monkey's head. 2) Since controlled cortical impact studies in non-human primates are unprecedented, the local IACUC required that we first conduct a pilot study to verify the lesion parameters and to understand the course of recovery after injury. This study has now been completed in three squirrel monkeys, and we have characterized the time course of the behavioral deficits on two different forelimb tasks: 1) a pellet retrieval task and 2) a grip force control task. For the impact procedure, under sterile surgical conditions, the dura was incised and retracted to perform motor mapping exploration of M1 using intracortical microstimulation procedures. This allowed precise identification of the M1 hand area. A commercial impactor designed for CCI studies was used with the following parameters: Impact tip diameter: 5 mm (slightly larger than the area of the M1 hand representation); Depth below surface: 3mm; impact velocity: 4 m/s; impact duration: 200 msec. The dura was replaced, the impact tip was positioned over the center of the M1 forelimb area, and the injury created.

Following the injury, each of the monkeys recovered from the procedure well, with no untoward side effects except for the expected paresis of the affected forelimb. Comparison of photographs of the impacted area before, and 15 weeks after the impact injury shows substantial distortion of the cortical tissue (**Figure 19**). Blood vessels outside of the impact area are intact 15 wks later, but tissue in the center of the impact is shrunken, due to necrosis of injured cortical tissue, and subsequent cavitation. The areas intended for microelectrode implantation are still intact, and thus, the proposed protocol is feasible for the full closed-loop intervention in primates.

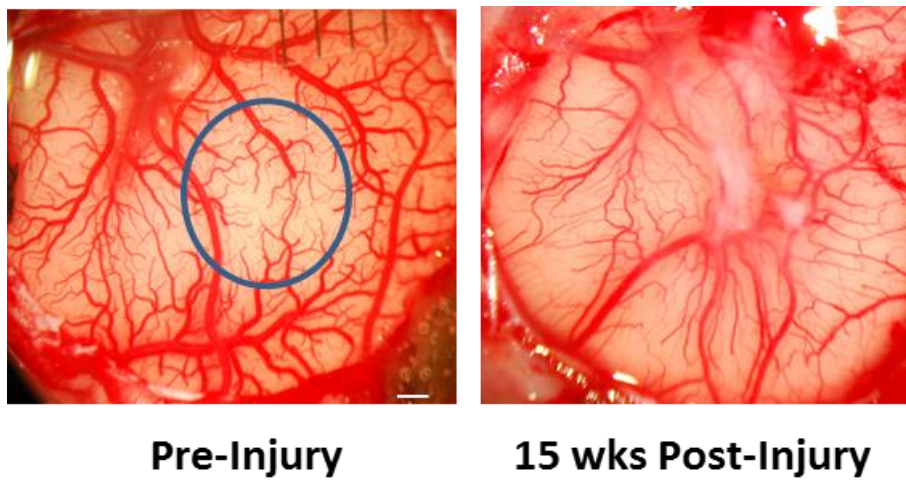


**Figure 19.** Photograph of cortical surface prior to, and 15 weeks after a CCI injury in motor cortex of a squirrel monkey. Black lines in left image indicate mm calibration marks. The blue circle indicates the location of the impact tip over the M1 forelimb representation.

**Figure 20** shows a monkey displaying initial deficits in both the grip task and the pellet retrieval task. It is important to note that except in a subset of days on the pellet retrieval task, the monkey made attempts, despite the poor performance. This indicates that our lesion size is appropriate, in that we can track performance over time, but the monkeys are not so impaired that they will not attempt the task, or have trouble eating. By 13 weeks post-injury, this monkey had completely recovered the ability to grip and hold with a range of force from 100-300 grams for 3 seconds. Note also that the scores on the pellet retrieval task were consistently worse after the injury, throughout the 13 weeks. While flexions per retrieval were approximately 2 before the injury, the daily averages ranged from 4 to 14 after the injury, and variability remained much higher.

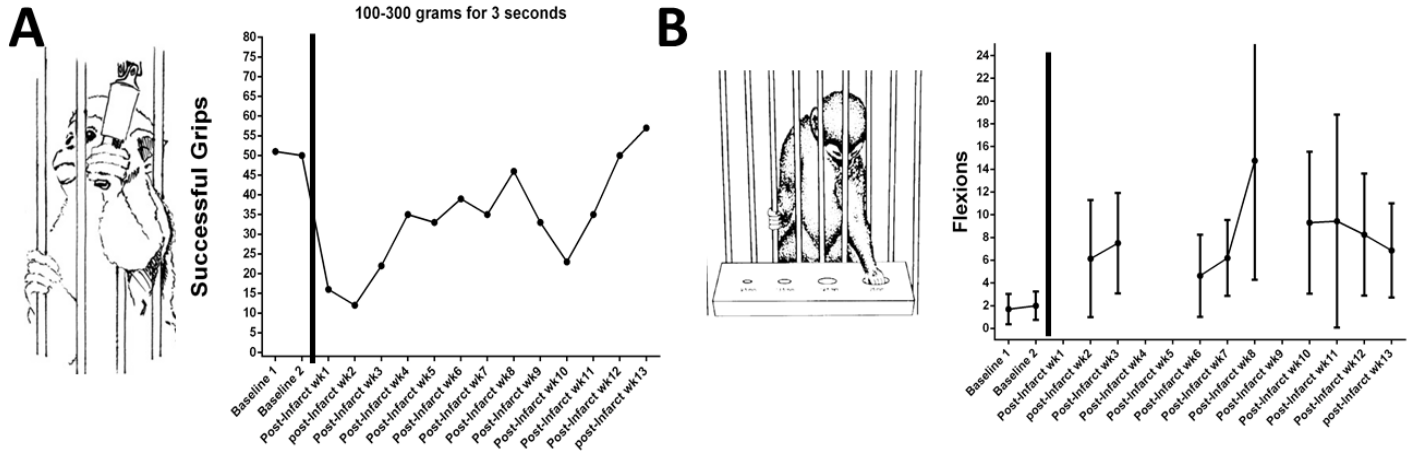


**Figure 20.** Natural behavioral recovery after CCI injury in the primary motor cortex hand representation in a representative squirrel monkey. A. Number of successful grips (100-300 gram grip held for 3 seconds) before and weekly post-injury for 13 weeks. B. Behavioral performance on a pellet-retrieval task requiring skilled use of the digits. Lower numbers indicate better performance.

Histological confirmation of the lesion revealed focal necrosis in the target region of the motor cortex corresponding to the impact location (**Figure 21**). In each of the three monkeys, the underlying cortical tissue displayed localized necrosis. As shown in the figure, while intact, the cortical tissue showed substantial shrinkage and loss of myelin substance due to degeneration of local neurons. Nissl stains (not shown) revealed severe to complete loss of neurons. Where neurons were still present, typical cortical lamination patterns were severely disrupted. While the underlying white matter was intact, distortion of the most superficial aspects of the corona radiata was evident. In the full study, impact parameters will be altered slightly (somewhat larger impact tip, slightly deeper penetration) in order to produce a more substantial and longer lasting behavioral deficit in untreated monkeys. This will provide a more robust and sensitive model for testing the effects of the proposed ADS intervention.

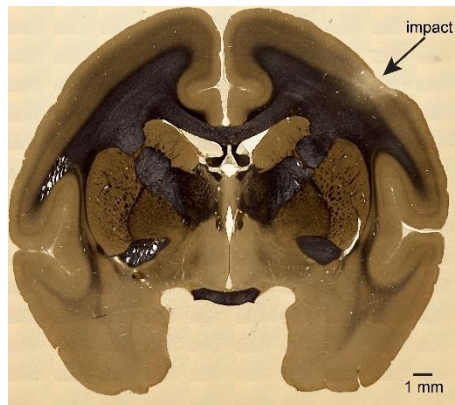


**Figure 21.** Weil-Myelin stain revealing myelinated axons in post-mortem tissue from squirrel monkey after CCI injury. Note the necrotic tissue at the location of the impact, as evidenced by dimpling of surface, loss of myelin, thinning of cortex, and distortion of underlying fibers in corona radiata (unpublished).

These data provide convincing evidence that we can successfully and reliably perform a CCI injury in the M1 hand area of a non-human primate, the squirrel monkey. As few such studies have ever been done in non-human primates, the paper generated from this study, now in preparation, should attract broad attention. The study suggests that we can create a CCI injury that spares the regions of interest for the closed-loop neuromodulation approach, like we performed in rats. The ventral premotor cortex and the somatosensory hand area are still intact after the injury, and there are chronic deficits that can potentially be overcome through the use of the closed-loop technology approach.

### **Key Research Accomplishments**

- Developed the smallest, most lightweight system to date for use with an ambulatory rat

- Demonstrated ADS in an ambulatory rat
- Demonstrated rapid recovery of motor performance in rats with TBI undergoing ADS
- Developed optimal design strategies for a fully enclosed, skull-mounted, non-human primate microsystem
- Developed a neural signal-processing algorithm for real-time stimulus artifact rejection (SAR)
- Implemented the algorithm in hardware on FPGA and IC platforms for real-time operation
- Demonstrated full functionality of the SAR IC via neurobiological experiments with an *Aplysia californica*
- Demonstrated rapid synaptic facilitation using ADS in anesthetized rats
- Demonstrated synaptic facilitation between target cortical areas that correlates with the recovery of motor skills
- Performed anatomical studies in healthy rats using tract-tracers to compare with CCI rats undergoing ADS
- Performed first CCI study in motor cortex of non-human primates and tracked behavioral recovery

## **Reportable Outcomes**

### **1- Manuscripts/Abstracts/Presentations:**

### **2- Patents and Licenses Applied for/Issued:**

- R. J. Nudo, P. Mohseni, D. Guggenmos, and M. Azin, *Methods and Associated Neural Prosthetic Devices for Bridging Brain Areas to Improve Function*, U.S. Patent No. 9,008,780 Awarded on April 14, 2015
- R. J. Nudo, P. Mohseni, D. Guggenmos, and M. Azin, *Methods and Associated Neural Prosthetic Devices for Bridging Brain Areas to Improve Function*, U.S. Non-Provisional (Continuation) Application No. 14/630,375 Filed on February 24, 2015
- R. J. Nudo, P. Mohseni, D. Guggenmos, and M. Azin, *Methods and Associated Neural Prosthetic Devices for Bridging Brain Areas to Improve Function*, International Application No. PCT/US2012/42381 Filed on June 14, 2012

### **3- Degrees Obtained from Award:**

- PhD (Kanokwan Limnuson), May 2015
- PhD (David Guggenmos), May 2013
- PhD (Meysam Azin), May 2011

### **4- Development of Cell Lines and Tissue/Serum Repositories:** Not applicable.

### **5- Infomatics (Databases and Animal Models):** None.

### **6- Funding Applied for:**

- *A Closed-Loop Neural Prosthesis for Restoration of Function after Traumatic Brain Injury*; US Army Medical Research and Materiel Command; PIs Mohseni and Nudo; \$1,654,379; 2016–2019 (Funded).
- *A Closed-Loop Neuroprosthetic Microdevice for Restoration of Function after Spinal Cord Injury*; US Army Medical Research and Materiel Command; PI Nudo/Co-I Mohseni/Co-I Tolosa; \$597,270; 2016–2019 (Recommended for Funding as an Alternate, but ultimately not funded).
- *Advanced Neuroprosthetics for Functional Restoration after Acquired Brain Injuries*; Kansas Board of Regents; PI Nudo/Co-I Guggenmos; \$125,000; 2015-2016 (Funded)

### **7- Employment/Research Opportunities Applied for/Received:**

- Kanokwan Limnuson, PhD Post-Doctoral Research Fellow, Feinstein Institute for Medical Research, Manhasset, NY
- Meysam Azin, PhD Staff Engineer, QualComm, San Diego, CA
- David Guggenmos, Ph.D., post-doctoral fellow, Duke University; research assistant professor, University of Kansas Medical Center, 2015-present.

### **8- Personnel Receiving Pay from Award:**

## **Conclusion**

Rapid progress was made toward developing smart prosthetic platforms for altering plasticity in the injured brain, leading to future therapeutic interventions for TBI that are guided by the underlying mechanisms for long-range functional and structural plasticity in the cerebral cortex. An unprecedented, potent effect of ADS on motor performance has been demonstrated in rats with TBI. Statistical analysis of the data is complete and includes both un-implanted and open-loop stimulation control groups. Post-hoc physiological data demonstrated rapid establishment of functional connectivity between the two areas. Efforts were also focused on developing a revised microsystem that would enable the investigation of the safety and efficacy of this approach in a non-human primate model of TBI, leading to the development of optimal design and partitioning strategies for a fully enclosed, skull-mounted microsystem with a long operation lifetime. In parallel, we also established the feasibility of IC implementation of a neural signal-processing algorithm for real-time elimination of stimulus artifacts that can potentially increase the amount of conditioning performed by the ADS microsystem between the two cortical regions.

## **References**

- [1] M. Azin, D. J. Guggenmos, S. Barbay, R. J. Nudo, and P. Mohseni, "A battery-powered activity-dependent intracortical microstimulation IC for brain-machine-brain interface," *IEEE J. Solid-State Circuits*, vol. 46, no. 4, pp. 731-745, April 2011.
- [2] A. Jackson, J. Mavoori, and E.E. Fetz, "Long-term motor cortex plasticity induced by an electronic neural implant," *Nature*, vol. 444, pp. 56-60, October 2006.
- [3] E. Rodriguez-Manyari, D. Guggenmos, A. Averna, C. Dunham, G. Van Acker, R. J. Nudo and M. Chiappalone, "Efficacy of an automated spike detection algorithm for processing *in vivo* multichannel recordings," *Soc for Neurosci Abstr.*, online, 451.09, November, 2015.
- [4] Nishibe, M., S. Barbay, D. Guggenmos, and R. J. Nudo "Reorganization of motor cortex after controlled cortical impact in rats and implications for functional recovery," *J Neurotrauma*, vol. 27, pp. 2221-32, November, 2010.
- [5] S. B. Frost, S. Barbay, K. M. Friel, E. J. Plautz, and R. J. Nudo, "Reorganization of remote cortical regions after ischemic brain injury: a potential substrate for stroke recovery," *J. Neurophysiology*, vol. 89, no. 6, pp. 3205-3214, 2003.
- [6] M. H. Kole, J. J. Letzkus, and G. J. Stuart, "Axon initial segment Kv1 channels control axonal action potential waveform and synaptic efficacy," *Neuron*, vol. 55, no. 4, pp. 633-647, August 2007.

Appendix I D. J. Guggenmos, M. Azin, S. Barbay, J. D. Mahnken, C. Dunham, P. Mohseni, and R. J. Nudo, "Restoration of function after brain damage using a neural prosthesis," *Proc. Natl. Acad. Sci. USA (PNAS)*, vol. 110, no. 52, pp. 21177-21182, December 2013.

Appendix II K. Limnuson, H. Lu, H. J. Chiel, and P. Mohseni, “Real-time stimulus artifact rejection via template subtraction,” *IEEE Trans. Biomed. Circuits and Systems*, vol. 8, no. 3, pp. 391-400, June 2014.

Appendix III K. Limnuson, H. Lu, H. J. Chiel, and P. Mohseni, “A bidirectional neural interface SoC with an integrated spike recorder, microstimulator, and low-power processor for real-time stimulus artifact rejection,” *J. Analog Integr. Circ. Sig. Process.*, vol. 82, no. 2, pp. 457-470, February 2015.

Appendix IV M. Azin, D. J. Guggenmos, S. Barbay, R. J. Nudo, and P. Mohseni, “A miniaturized system for spike-triggered intracortical microstimulation in an ambulatory rat,” *IEEE Trans. Biomed. Eng.*, vol. 58, no. 9, pp. 2589-2597, September 2011.

Appendix V Murphy, M., D.J. Guggenmos, D. Bunday and R.J. Nudo (2016) Current challenges facing the translation of brain-computer interfaces from preclinical trials to use in human patients. *Front Cell Neurosci*, 9:497.

# Restoration of function after brain damage using a neural prosthesis

David J. Guggenmos<sup>a,b,1</sup>, Meysam Azin<sup>c,2</sup>, Scott Barbay<sup>a,b</sup>, Jonathan D. Mahnken<sup>d</sup>, Caleb Dunham<sup>a,b</sup>, Pedram Mohseni<sup>c</sup>, and Randolph J. Nudo<sup>a,b,3</sup>

Departments of <sup>a</sup>Molecular and Integrative Physiology and <sup>b</sup>Biostatistics, and <sup>d</sup>Landon Center on Aging, Kansas University Medical Center, Kansas City, KS 66160; and <sup>c</sup>Department of Electrical Engineering and Computer Science, Case Western Reserve University, Cleveland, OH 44106

Edited\* by Michael Merzenich, Brain Plasticity Institute, San Francisco, CA, and approved November 15, 2013 (received for review September 6, 2013)

**Neural interface systems are becoming increasingly more feasible for brain repair strategies. This paper tests the hypothesis that recovery after brain injury can be facilitated by a neural prosthesis serving as a communication link between distant locations in the cerebral cortex. The primary motor area in the cerebral cortex was injured in a rat model of focal brain injury, disrupting communication between motor and somatosensory areas and resulting in impaired reaching and grasping abilities. After implantation of microelectrodes in cerebral cortex, a neural prosthesis discriminated action potentials (spikes) in premotor cortex that triggered electrical stimulation in somatosensory cortex continuously over subsequent weeks. Within 1 wk, while receiving spike-triggered stimulation, rats showed substantially improved reaching and grasping functions that were indistinguishable from prelesion levels by 2 wk. Post hoc analysis of the spikes evoked by the stimulation provides compelling evidence that the neural prosthesis enhanced functional connectivity between the two target areas. This proof-of-concept study demonstrates that neural interface systems can be used effectively to bridge damaged neural pathways functionally and promote recovery after brain injury.**

brain-machine-brain interface | neural plasticity | traumatic brain injury | closed-loop | long-term potentiation

The view of the brain as a collection of independent anatomical modules, each with discrete functions, is currently undergoing radical change. New evidence from neurophysiological and neuroanatomical experiments in animals, as well as neuroimaging studies in humans, now suggests that normal brain function can be best appreciated in the context of the complex arrangements of functional and structural interconnections among brain areas. Although mechanistic details are still under refinement, synchronous discharge of neurons in widespread areas of the cerebral cortex appears to be an emergent property of neuronal networks that functionally couple remote locations (1). It is now recognized that not only are discrete regions of the brain damaged in injury or disease but, perhaps more importantly, the interconnections among uninjured areas are disrupted, potentially leading to many of the functional impairments that persist after brain injury (2). Likewise, plasticity of brain interconnections may partially underlie recovery of function after injury (3).

Technological efforts to restore brain function after injury have focused primarily on modulating the excitability of focal regions in uninjured parts of the brain (4). Purportedly, increasing the excitability of neurons involved in adaptive plasticity expands the neural substrate potentially involved in functional recovery. However, no methods are yet available to alter the functional connectivity between spared brain regions directly, with the intent to restore normal communication patterns. The present paper tests the hypothesis that an artificial communication link between uninjured regions of the cerebral cortex can restore function in a rodent model of traumatic brain injury (TBI). Development of such neuroprosthetic approaches to brain repair may have important implications for the millions of individuals who are left with

permanent motor and cognitive impairments after acquired brain injury, as occurs in stroke and trauma.

For the present experiment, we used a rodent model of focal brain injury to the caudal forelimb area (CFA), a region that is part of the cortical sensorimotor system. This area in the frontal cortex shares many properties with primary motor cortex (M1) of primates; injury to M1 results in long-term impairment in reaching and grasping functions (5). Traditionally, it has been thought that impairment occurs because M1 provides substantial outputs to the motor apparatus in the spinal cord, thus directly affecting motor output function. However, M1 also has important interconnections with the primary somatosensory cortex (S1) located in the parietal lobe (Fig. 1A). Long-range corticocortical fibers from S1 provide critical information to M1 about the position of the limb in space. Thus, injury to M1 results in impaired motor performance due, at least in part, to disruption in communication between the somatosensory and motor cortex (6).

To test our hypothesis that functional recovery can be facilitated by creating an artificial communication link between spared somatosensory and motor regions of the brain, we focused on the rat's premotor cortex (PM). The rostral forelimb area (RFA) is a premotor area in the rodent's frontal cortex that shares many properties with PM of primates and is thought to participate in recovery of function after injury to M1 (5, 7–9). PM areas are so-named because the principal target of their output fibers is M1 (10). PM areas also have long-range corticocortical connections with somatosensory areas, but at least in

## Significance

Closed-loop systems, or brain-machine-brain interfaces (BMBIs), have not been widely developed for brain repair. In this study, we targeted spared motor and somatosensory regions of the rat brain after traumatic brain injury for establishment of a functional bridge using a battery-powered microdevice. The results show that by using discriminated action potentials as a trigger for stimulating a distant cortical location, rapid recovery of fine motor skills is facilitated. This study provides strong evidence that BMBIs can be used to bridge damaged neural pathways functionally and promote recovery after brain injury. Although this study is restricted to a rodent model of TBI, it is likely that the approach will also be applicable to other types of acquired brain injuries.

Author contributions: D.J.G., M.A., P.M., and R.J.N. designed research; D.J.G., M.A., and S.B. performed research; D.J.G., M.A., J.D.M., C.D., P.M., and R.J.N. analyzed data; and D.J.G., M.A., J.D.M., P.M., and R.J.N. wrote the paper.

The authors declare no conflict of interest.

\*This Direct Submission article had a prearranged editor.

Freely available online through the PNAS open access option.

<sup>1</sup>Present address: Department of Neurobiology, Duke University, Durham, NC 27705.

<sup>2</sup>Present address: Qualcomm CDMA Technologies, Qualcomm, Inc., San Diego, CA 92121.

<sup>3</sup>To whom correspondence should be addressed. E-mail: rnudo@kumc.edu.

This article contains supporting information online at [www.pnas.org/lookup/suppl/doi:10.1073/pnas.1316885110/-DCSupplemental](http://www.pnas.org/lookup/suppl/doi:10.1073/pnas.1316885110/-DCSupplemental).

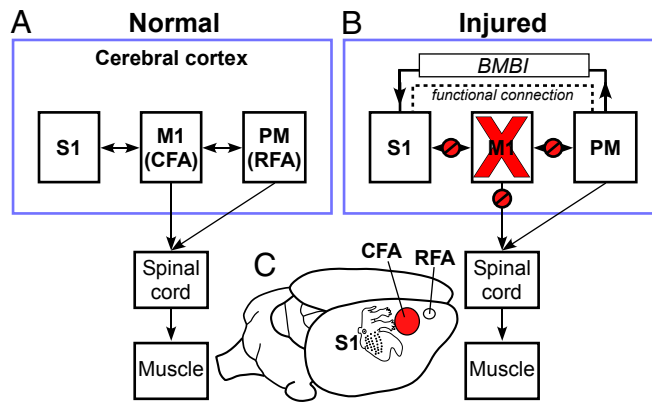


**Fig. 1.** Theoretical model of neuroprosthetic treatment approach after brain injury. (A) Normal connectivity of M1, S1, and PM. Both M1 (CFA in rat) and PM (RFA in rat) send substantial outputs to the spinal cord via the corticospinal tract. Also, extensive reciprocal connections exist between M1 and PM, as well as between M1 and S1. (B) Effects of focal M1 injury on brain connectivity and the hypothetical effect of a BMBI to restore somatosensory-motor communication. An injury to M1, as might occur in stroke or brain trauma, results in a focal area of necrosis, as well as loss of M1 outputs to the spinal cord. Corticocortical communication between M1 and S1 (and between M1 and PM) is also disrupted, further contributing to functional impairment. Because the uninjured PM also contains corticospinal neurons, it might have the ability to serve in a vicarious role. The dotted line indicates enhanced functional connection between PM and S1 that we propose is established after treatment with a BMBI. (C) Location of target areas in rat cerebral cortex. A topographic map of the somatosensory representation in S1 is superimposed on the cortex.

intact animals, they appear to be relatively weak compared with M1's connections with the somatosensory cortex (9, 11, 12).

Our approach was to link the neural activity of the PM forelimb area (RFA) functionally with activation of the S1 forelimb area following a controlled cortical impact (CCI) to M1 (Fig. 1B and C). To this end, a microdevice was developed with the ability to deliver activity-dependent stimulation (ADS) through recording and digitizing extracellular neural activity from an implanted microelectrode, discriminating individual action potentials (spikes), and delivering small amounts of electrical current to another microelectrode implanted in a distant population of neurons (13, 14). This closed-loop system was similar, in principle, to the "Neurochip" used previously by other investigators to demonstrate the effects of local ADS in intact animals (15), but it was miniaturized for head-mounted, wireless operation (Fig. 2A and Fig. S1). By linking the activity of one area of the cortex with that of a distant area of the cortex, a closed-loop brain-machine-brain interface (BMBI) for artificial corticocortical communication between PM and S1 was created.

Individual spikes were detected in PM, and subsequent stimulation was delivered to S1 after a 7.5-ms delay (Fig. 2B). (Because connections between distant cortical areas are commonly reciprocal, enhanced communication theoretically could be established by ADS in either direction.) After the M1 injury, rats were implanted with microelectrodes connected to the BMBI microdevice (Fig. 2A). The microdevice delivered ADS 24 h per day up to 28 d postinjury, except for brief motor assessment sessions on predetermined days. Behavioral recovery in ADS rats was compared with recovery in rats with open-loop stimulation (OLS), in which S1 stimulation was uncorrelated with spikes in PM, and with control rats that had no microdevice implanted.

## Results

**Testing Motor Skill After Brain Injury.** The primary behavioral assay for determining whether ADS resulted in functional improvement

after brain injury was a skilled reaching task. This widely used task is a particularly sensitive measure of forelimb motor function after M1 lesions in both rodents and primates. Rats were pretrained to achieve a minimum criterion score of >70% successful pellet retrievals. After the lesion was created, rats were tested on the task during assessment sessions on postlesion days 3, 5, 8, 14, 21, and 28. During each postlesion assessment session, rats were tested under two conditions: first with the microdevice stimulation function turned OFF and then with the stimulation function turned ON. Rats in each of the three groups demonstrated a severe deficit on the skilled reaching task in the first few days after the injury (Fig. 3). On postlesion days 3 and 5, there were no significant differences in motor performance between the groups (global comparisons:  $P = 0.5265$  and  $P = 0.0945$ , respectively). Rats in the control group (with a lesion but no microdevice) continued to demonstrate a profound deficit that plateaued at only about 25% successful retrievals. In striking contrast, by postlesion day 8, group performance was significantly different (global comparison:  $P = 0.0044$ ). Rats in the ADS group showed a substantial and statistically significant behavioral improvement in reaching success compared with rats in the other groups in the ON condition (pairwise comparisons:  $P = 0.0418$  for ADS vs. OLS,  $P = 0.0012$  for ADS vs. control, and  $P = 0.2110$  for OLS vs. control; Fig. 3 and Movies S1 and S2). By postlesion day 14, the performance of the rats in the ADS group was approximately at prelesion levels and significantly higher than that of rats in the other groups. The difference between the OLS group and the control group approached significance on day 14 (global comparison:  $P = 0.0004$ ; pairwise comparisons:  $P = 0.0284$  for ADS vs. OLS,  $P < 0.0001$  for ADS vs. control, and  $P = 0.0555$  for OLS vs. control). By postlesion day 21, performance in the ADS group remained high and statistically different from that of the control group. Performance was not significantly different in the ADS group between days 14 and 21 ( $P = 0.576$ ). However, by day 21, the OLS group had improved further, so that the difference between the two groups was not significant (global comparison:  $P = 0.0007$ ;

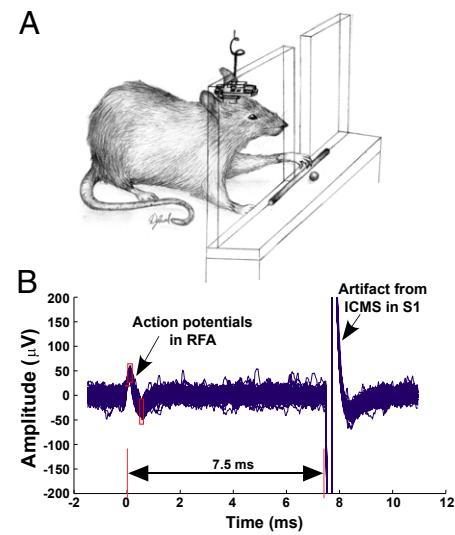


**Fig. 2.** ADS protocol. After injury to the CFA, a recording microelectrode was placed in the RFA, whereas a stimulating microelectrode was placed in the distal forelimb field of S1. A BMBI discriminated action potentials in the RFA, and after a 7.5-ms delay, it delivered a low-level electrical current pulse to S1 (13). (A) Sketch of a rat retrieving a food pellet with a BMBI attached to the skull. (B) Sample traces of recordings from the RFA showing action potentials and stimulus artifacts from an ICMS current delivered to S1. Time-amplitude window discriminators are indicated by red boxes. A total of 100 superimposed traces are shown.

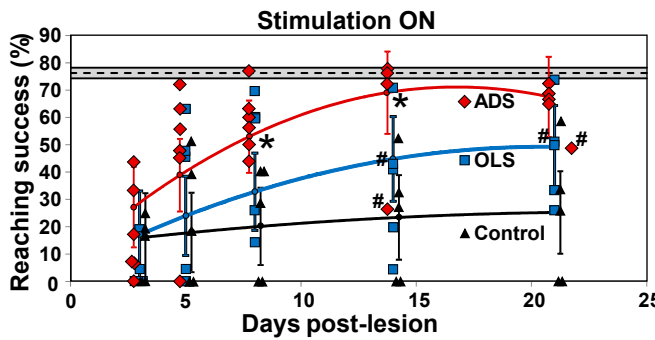


**Fig. 3.** Performance of rats on a skilled reaching task after injury to M1 (ON condition). The ADS group is shown in red, the OLS group is shown in blue, and the control group is shown in black. The dotted line indicates the average prelesion performance of all animals in the study. The bounded area indicates the 95% confidence interval. Regression lines are based on an LMM (43). Error bars represent 95% confidence intervals. \* $P < 0.05$  (pairwise difference between the ADS and OLS groups). Because the statistical analysis was an intent-to-treat model, rats were included in the analysis even if the microdevice was no longer functional. Only one rat in the ADS group had a microdevice that was functional by postlesion day 28; thus, figures are presented through postlesion day 21 (*SI Results*). Diamonds, squares, and triangles represent individual animal data points. #, microdevice not functional (Tables S1 and S2).

pairwise comparisons:  $P = 0.0891$  for ADS vs. OLS,  $P = 0.0002$  for ADS vs. control, and  $P = 0.0278$  for OLS vs. control). Although the mean performance of the ADS group was higher than that of the OLS group even in the OFF condition, differences were not statistically significant on any postlesion day (Fig. S2).

**Immediate Effects Within Single Sessions.** Rats in the ADS group often showed substantially improved performance within a single day's session when the microdevice was switched from the OFF to the ON condition. One particularly salient example can be seen in a video of a rat in the ADS group on postlesion day 8 (Movie S2). In the OFF condition, this rat made many attempts to reach through the opening in the Plexiglas but was rarely able to do so accurately. Large trajectory errors were made, and relatively few retrievals were completed successfully. Following completion of trials in the OFF condition, the microdevice was programmed to the ON state, a process that required 2–3 min. As soon as the microdevice was turned ON, the rat began to retrieve pellets with noticeably enhanced success. Movements tended to be slower and seemingly more deliberate, and fewer errors were made. A statistical analysis of the ADS group between the OFF and ON conditions revealed significantly better performance in the ON condition on postlesion day 3 ( $P = 0.0003$ ), postlesion day 5 ( $P = 0.0005$ ), and postlesion day 8 ( $P = 0.0019$ ) and marginally better performance on postlesion day 14 ( $P = 0.0666$ ). The same analysis for the OLS group revealed significantly worse performance in the ON condition on postlesion day 3 ( $P = 0.0471$ ) and marginally worse performance on postlesion day 5 ( $P = 0.0554$ ) and postlesion day 8 ( $P = 0.0781$ ) (Fig. S3). These effects tended to dissipate over time, so that no differences were detected between OFF and ON conditions in either group by postlesion day 21. These within-day differences through postlesion day 8 suggest that the timing of the S1 stimulus pulse is critical. Behavioral performance was significantly better when the S1 stimulus pulse was delivered contingent upon an action potential in the RFA (i.e., in the ADS group).

**Effects of ADS on Functional Connectivity.** To explore possible neurophysiological mechanisms underlying the behavioral effects of the ADS treatment on postinjury motor performance, we performed post hoc analysis of spike events in the RFA that were

discriminated in the 28 ms after each S1 stimulus pulse. This time window represented our imposed blanking period during which additional S1 stimulus pulses could not occur. Poststimulus spike histograms were compared with 28-ms periods chosen from data acquired in the OFF condition 7.5 ms after each RFA spike event. The results show that substantially more spikes in the RFA occurred following S1 stimulation in the ADS group, with peak activity occurring ~4–6 ms after the S1 stimulus pulse (Fig. 4A). Spike rates were nearly threefold higher averaged across the 28-ms period compared with a comparable period in the OFF condition. Spike rates in the OLS group were slightly lower than in the ADS group in the OFF condition but were significantly lower than in the ADS group in the ON condition. These data suggest that ADS substantially reinforced network interactions between S1 and the RFA, whereas OLS did not.

Subdividing the spike histograms by day reveals that enhanced spike activity in the ADS ON condition is evident even on the first day that the microdevice was activated (Fig. 4B and Fig. S4). There is also a trend toward further increases in spike discharge between the first (days 1 and 5) and second (days 8 and 14) weeks in the ADS group, corresponding to the time period when behavioral performance approached normal levels.

Whether behavioral performance and enhanced functional connectivity persist following the end of treatment cannot be addressed fully based on the current results (*SI Discussion*). However, it is noteworthy that there was a significant decrease in mean performance in the ADS group between postinjury days 21 and 28 (Fig. S5). During this time period, microelectrode-microdevice connection failures prevented normal operation of the microdevice in most of the ADS rats. This phenomenon of reduced behavioral performance after deactivation provides further

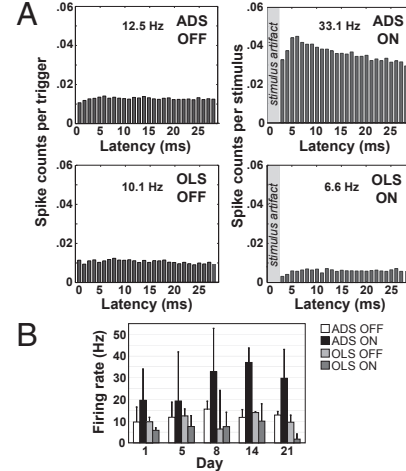


**Fig. 4.** Comparison of spike activity in the RFA in the ADS and OLS groups. Data represent spikes discriminated in the RFA over a 28-ms period. In the ON condition, the trigger for the data acquisition was the S1 stimulus pulse. In the OFF condition, the trigger for the data acquisition was 7.5 ms after a spike event in the RFA. (A) Composite posttrigger spiking histograms derived from neural recordings in the RFA compiled from days 1, 5, 8, 14, and 21 ( $\pm 1$  d). Histograms portray the mean spike counts per trigger event within each time bin (also Fig. S4). Spike counts were based on an average of over 22,000 trigger events per animal per day. Poststimulus firing rates were substantially higher in the ADS ON condition (33.1 Hz), compared with the ADS OFF (12.5 Hz), OLS ON (6.6 Hz), or OLS OFF (10.1 Hz) condition. (B) Average spike firing rates throughout the 28-ms window for each day. Error bars represent between-subject variation on each day (plus 1 SD). LMMs detected higher firing rates in the ADS group compared with the OLS group with stimulation ON ( $P < 0.0001$ ). Firing rates did not differ statistically between groups in the OFF condition ( $P > 0.05$ ). Posttrigger spiking histograms for each day are shown in Fig. S4.

support for the notion that the behavioral improvements were mediated by closed-loop operation. It also suggests that either a longer duration of operation (i.e., beyond 21 d) is required for persistent effects or that closed-loop stimulation enhances the rate, but not the extent, of recovery compared with OLS. Nonetheless, the present data provide persuasive evidence that targeted closed-loop stimulation approaches are feasible as brain repair strategies. Rapid behavioral recovery parallels the development of increased functional connectivity between spared somatosensory and motor regions of the cortex.

## Discussion

This proof-of-concept study indicates that a closed-loop neuroprosthetic microdevice can enhance functional connectivity between distant cortical locations and generate rapid improvement in motor function after cortical injury, at least in rats with M1 damage. A closed-loop device with similar functionality induced neurophysiological changes when applied over a short distance within M1 of intact monkeys (15). More recently, spike-triggered stimulation was used to demonstrate increased potentiation between neurons in the sensorimotor cortex of rats. The spike-stimulation delay was important, because 5 ms resulted in robust increases, whereas 100 or 500 ms resulted in no potentiation (16). The present study demonstrates that the extension of the ADS approach to injured brains has demonstrable effects on recovery and establishes functional communication that is qualitatively different compared with uncorrelated stimulation. The current implementation of the system architecture, using a lightweight, battery-powered, wireless, miniaturized microdevice for spike-triggered intracortical microstimulation (ICMS), represents an important step in the process of developing implantable BMBIs for neural repair in clinical populations.

**Differential Mechanisms Underlying the Effects of OLS and ADS on Behavioral Recovery.** The mechanisms underlying the therapeutic effects of OLS and ADS after injury in the present model of TBI are still somewhat speculative. In the 1940s, Donald Hebb (17) postulated that “When one cell repeatedly assists in firing another, the axon of the first cell develops synaptic knobs... in contact with the soma of the second cell.” This hypothesis has morphed into the modern maxim “Cells that fire together, wire together,” a phrase made popular by neuroscientist, Carla Shatz (18). A large literature has grown from these initial hypotheses, and a neurophysiological phenomenon widely known as “Hebbian plasticity” has formed the basis for many neuroscientific models of learning and memory. Previous studies in intact primates and rodents using ADS or paired-pulse stimulation show the ability for such coactivation to alter output properties of cortical neurons (15, 16, 19). Presumably, the stimulation causes Hebbian-like plasticity to alter existing connectivity within a cortical area.

Although significant behavioral recovery occurred in both the ADS and OLS groups compared with control rats, the ADS group improved substantially more rapidly. Also, in the early postlesion period, the ADS group demonstrated a qualitatively different ON vs. OFF performance compared with the OLS group. These behavioral results alone suggest that different mechanisms underlie recovery in ADS and OLS groups. Although the results of ICMS on behavioral outcomes in animal models of brain injury have not been reported previously, several studies have examined the therapeutic effects of surface stimulation in either human stroke survivors or animal stroke models. For example, an invasive technology using epidural stimulation to provide low-level current pulses over uninjured cortical areas during the execution of rehabilitative training resulted in behavioral improvement in rodent and nonhuman primate models of cortical ischemic injury (20, 21). Although initial results in clinical stroke populations were promising, the therapeutic effect of open-loop epidural stimulation was not demonstrated in a randomized clinical trial (22). Nonetheless,

noninvasive cortical stimulation approaches (transcranial magnetic stimulation and transcranial direct-current stimulation) continue to attract substantial interest due to positive results in small groups of stroke survivors (23).

Evidence to support specific mechanisms underlying the effects of open-loop electrical stimulation of the cortex on recovery is largely correlative but includes motor map reorganization, increased dendritic length and spine density, cell proliferation and cell migration in the subventricular zone, receptor subunit expression, activation of antiapoptotic cascades, increased neurotrophic factors, enhanced angiogenesis, and proliferation of inflammatory cells (20, 21, 24–28). Because the number of stimulus pulses was similar in the ADS and OLS groups in the present study, it is reasonable to conclude that if electrical stimulation promoted proliferative processes, the effects were the same in the two groups.

In addition, various OLS protocols produce alterations in synaptic efficacy. These data are particularly relevant because of the qualitative differences in functional connectivity observed between ADS and OLS groups. Long-term potentiation (LTP), an experimental phenomenon first discovered in the hippocampus of anesthetized rabbits over 40 y ago (29), is expressed in both excitatory and inhibitory synapses throughout the mammalian brain (30). Although many experimental protocols have been developed to optimize synaptic potentiation in various model systems, the sign and magnitude of synaptic potentiation are heavily dependent upon the frequency and pattern of stimulation (31, 32).

Despite comparable mean stimulation frequency between the two groups, the temporal structure of stimulus pulses differed between the ADS and OLS groups. Interstimulus intervals spanned approximately the same range, but the intrinsic temporal firing pattern observed in the ADS group resulted in a greater number of short interstimulus intervals (Fig. S6A). Thus, ADS stimulation occasionally consisted of stimulus pulses at higher frequency, somewhat analogous to theta-burst stimulation, in which train bursts of high-frequency pulses (e.g., four to eight pulses at 100–300 Hz) are delivered at about 6–7 Hz (i.e., within the theta-rhythm frequency). Theta-burst stimulation is often used to optimize generation of LTP, especially in the neocortex of awake animals, where LTP has traditionally been more difficult to generate (33). In a study in the neocortex of freely moving rats, theta-burst stimulation, using parameters similar to those used in the hippocampus, evoked LTP, but the effects required at least 5 d to develop and plateaued at about 15 d (34). In the present study, although enhanced, short-latency spike discharge was evident with ADS even on the first day of stimulation, the time course of the behavioral effects was remarkably similar to the slowly developing LTP found in the rat neocortex study.

Theta-burst timing protocols vary considerably depending upon the particular model system. However, a recent study in a mouse brain slice preparation in the dorsal striatum suggests that the optimal theta-burst patterns are those that best match intrinsic neural activity patterns (35). Further, “burstiness” was critical to inducing LTP. Simply reducing the interburst pause from 35 ms to 20 ms eliminated the induction of LTP. It is possible that our imposed 28-ms blanking period further contributed to the neurophysiological and behavioral effects. We propose that by using a closed-loop stimulation paradigm, the intrinsic stimulation patterns that optimally drive synaptic potentiation in the cortico-cortical pathways were used. (The feasibility of using optimal theta-burst parameters in an open-loop mode of stimulation is discussed in *SI Discussion*).

In summary, OLS and ADS may both contribute to behavioral recovery but by somewhat different mechanisms. Electrical stimulation, in general, is likely to modulate neuronal growth processes, leading to adaptive plasticity that could account for at least part of the behavioral improvement. In the closed-loop (ADS) condition, however, the intrinsic firing pattern drives synaptic

potentiation in a manner similar to that observed in theta-burst protocols. Although potentiation builds rapidly (within 1 d), we propose that chronic ADS results in a behaviorally relevant, functional connection between S1 and PM.

**Future Applications of Closed-Loop Neuroprostheses for Treating Neurological Disorders.** A closed-loop neuroprosthesis applying ADS across distant cortical areas is a vastly different approach to brain repair than has been achieved to date. Therapeutic closed-loop stimulation in the brain is still uncommon. However, analogous approaches are already being tested for epilepsy, and an expanded role for closed-loop systems for deep brain stimulation in Parkinson disease is now being considered (36, 37). Further, closed-loop approaches are under development in animal models of spinal cord injury (38, 39). Other investigators have proposed a closed-loop approach for a cognitive prosthesis that has shown promise in animal models (40). Other potential clinical applications based on the current model include stroke, focal TBI, and surgical resections. Finally, a variety of neurological syndromes that are thought to be related to disruption of cortical communication may be amenable to ADS. In the 1960s, Norman Geschwind identified several disorders collectively called “disconnection syndromes,” revolutionizing the field of behavioral neurology (41). The consideration of closed-loop approaches to repair of cortical disconnection syndromes may open treatment options for a variety of conditions in which neural communication is disrupted, whether due to disease, injury, or idiopathic causes.

## Materials and Methods

**Animals.** Adult, male Long-Evans hooded rats ( $n = 16$ , weight: 350–450 g; Harlan) were procured at 4 mo of age. Protocols for animal use were approved by the Kansas University Medical Center Institutional Animal Care and Use Committee and adhered to the *Guide for the Care and Use of Laboratory Animals* (42). Each rat was singly housed in a transparent cage and provided with food and water ad libitum. The room was kept on a 12-h:12-h light/dark cycle, and ambient temperature was maintained at 22 °C.

Rats were assigned to three groups: the ADS group, the OLS group, and the control group. Rats in all three groups received a CCI injury over the M1 forelimb area (5). Postmortem histological analysis confirmed that lesion size was comparable across groups (*SI Results*). The surgical procedures (e.g., burr holes, skull screws, dura resection) were identical in all three groups. Microelectrode implantation and microdevice attachment were identical in the ADS and OLS groups. In both the ADS and OLS groups, one single-shank microelectrode array was inserted into the S1 forelimb area. A second single-shank microelectrode array was inserted into the RFA (depths are provided in *SI Materials and Methods*). In the ADS group, stimulation in S1 was contingent upon spike activity in the RFA; that is, time-amplitude window discriminators determined when action potentials were recorded from the RFA microelectrode. Discrimination of an individual action potential triggered delivery of a brief pulse of electrical current to the microelectrode implanted in S1. In the OLS group, the stimulation was delivered arbitrarily at a frequency approximately the same as that in the ADS group but with the timing of stimulation uncorrelated with the discriminated action potentials (*SI Materials and Methods*). The wireless, battery-powered microdevice, mounted to the freely moving rat's skull, operated 24 h per day (Fig. 2A and Fig. S1).

**CCI Procedure.** In each rat, the skull over the CFA was removed while leaving the dura intact. A 3-mm diameter rod with a flat tip was placed into a commercial impactor device (Leica Microsystems), centered over the target location (*SI Materials and Methods*), and then lowered until the surface of the tip was in contact with the dura, as indicated by an audible signal triggered by a feedback sensor. The rod was then retracted and armed. An impact was delivered with an excursion of 2 mm below the surface of the dura. This protocol leads to reproducible lesions that damage all cortical layers within the CFA with minimal superficial damage to underlying white matter tracts and limited or no damage to adjacent cortical areas (5).

**Microdevice Programming. ADS programming.** To determine discrimination parameters for ADS, the channel with the best signal-to-noise ratio was chosen. This same channel was later used during microdevice operation to determine spike events that triggered stimulation. Using a custom MATLAB

(MathWorks) script, action potentials were discriminated offline by thresholding and two user-adjustable time-amplitude windows, with the intent of maximizing discrimination of observed spikes while minimizing noise and/or stimulus artifacts. Stimulation parameters were set to deliver a 60-μA, 192-μs, pseudobiphasic current pulse with a 7.5-ms delay following spike discrimination (Fig. 2B). A blanking interval following each spike discrimination prevented additional stimulus pulses for 28 ms. The spike discrimination, timing, and stimulation parameters were then uploaded to the microdevice for online spike discrimination. Thus, during device operation in the ADS group, each discriminated spike in PM triggered a stimulation pulse in S1, constrained by the blanking interval.

The 7.5-ms delay was based on previous studies of the effective delay within local networks, analysis of spike-stimulus delays in pilot data, as well as constraints in the current microdevice architecture. The 28-ms blanking interval was also based on analysis of spike-stimulus delays in pilot data and was set to reduce the possibility of producing a positive-feedback loop, in which S1 stimulation might drive action potentials in PM, retriggering stimulation of S1. **OLS programming.** Stimulation parameters were the same in the OLS group as for the ADS group. However, the stimulation was not contingent upon recorded neural activity. Instead, the stimulation was set to occur arbitrarily with interstimulus intervals ranging from 35 to 200 ms (randomized equally across the range), closely approximating the stimulus rate for the ADS group (*SI Materials and Methods*, *SI Results*, and Fig. S6A).

**Signal monitoring and maintenance.** The neural activity and stimulation rates were monitored daily throughout the study via a wireless connection. The microdevice ran continuously, delivering ADS or OLS 24 h a day during the experiment, except for brief periods required for behavioral assessment, changing the battery, and adjusting the window discriminator parameters.

Bandpass-filtered neural data (~500 Hz to 5 kHz) were recorded at ~35.7 kHz per channel from either one or four channels (wireless or wired connection, respectively) during all signal monitoring and behavioral trials using LabVIEW software (National Instruments). In addition, all animals had multiple sessions during which data were recorded during home cage behavior. The raw signal recording duration of any single monitoring period was software-limited to ~45 min, but the stimulus trigger signal could be recorded for up to 24 h. The neural signal data were converted from a LabVIEW file to a text file and analyzed using custom MATLAB software.

**Behavioral Training and Assessment. Skilled reaching task.** Each rat was tested in a 30-cm × 30-cm × 52-cm Plexiglas reaching chamber. For each trial, a single food pellet (45 mg; Bioserv) was placed into a shallow well 2 cm from the front wall on an external shelf positioned 3 cm from the bottom of the chamber. The rat was required to reach through a narrow slot to retrieve the pellet with its forepaw (Fig. 2A). After forelimb preference was determined, a removable Plexiglas wall was used to force the animal to use only the preferred forelimb (5). Trials were recorded with a digital camcorder for playback and analysis. The percentage of success was measured as the percentage of trials in which the rat grasped, retrieved, and brought the pellet to the mouth (60 trials per day). Before entry into the remainder of the study, the rat was required to reach and retrieve food pellets above 70% success for 3 consecutive days. Following the injury (see below), behavioral probing sessions were conducted on postlesion days 3, 5, 8, 14, 21, and 28. Testing on postlesion days 1 and 2 was not practical due to the effects of surgical recovery and postsurgical analgesics on behavioral performance. Probing sessions consisted of 20 trials with the microdevice stimulation function turned OFF and then 20 trials with the microdevice stimulation function turned ON.

**Foot-fault task.** Rats were also assessed on a foot-fault task to determine the effects of the injury on a locomotion task. In general, although there was an effect of the injury on this task on postlesion day 3, no lesion effects were observed on subsequent days. Also, there were no differences between groups at any time points. This result was not unexpected, because the foot-fault task is less sensitive, and spontaneous recovery is common with lesions restricted to the forelimb motor cortex.

**Statistical Analysis of Behavioral Performance.** Initially, animals were randomly assigned to an ADS ( $n = 6$ ) or control ( $n = 5$ ) group. A subsequent OLS group ( $n = 5$ ) was studied after group randomization. This was necessary to use neurophysiological data from the ADS group to determine the stimulation protocol for the OLS group.

Linear mixed models (LMMs) (43) were generated via restricted maximum likelihood estimation using SAS version 9.2 PROC GLIMMIX (SAS Institute, Inc.) to model performance on the skilled reaching task for each animal over time. Results are presented to mirror a series of one-way ANOVA models because the LMM provides analogous results. For animals in the ADS and

OLS groups, the difference between the OFF and ON conditions was studied as an outcome. Models included fixed effects for treatment group, time, and their interaction.

Time was treated as a continuous measure to generate estimates of a polynomial relationship for recovery profiles in each treatment group over time up to a (treatment group-specific) quadratic relationship. Animal-specific effects were introduced by allowing for random intercepts in these models; thus, the models allowed for estimation of normally distributed error terms both for between- and within-animal effects. Backward elimination was used to determine the functional form of these relationships with *F* test *P* values <0.05 for effects to remain in the models. All lower ordered terms were retained in models in the presence of higher level interaction effects, regardless of statistical significance. Models were evaluated by visual inspection of observed vs. predicted values for each animal to assess model fit, observed vs. residuals plots to assess constant variance assumptions, and histograms of the residuals and quantile-quantile plots to assess the assumption of normally distributed random effects. Residuals included both those for the random intercept coefficients (for between-animal error terms) and overall residuals (for within-animal error terms).

1. Vicente R, Gollo LL, Mirasso CR, Fischer I, Pipa G (2008) Dynamical relaying can yield zero time lag neuronal synchrony despite long conduction delays. *Proc Natl Acad Sci USA* 105(44):17157–17162.

2. Carter AR, Shulman GL, Corbetta M (2012) Why use a connectivity-based approach to study stroke and recovery of function? *Neuroimage* 62(4):2271–2280.

3. Nudo RJ (2011) Neural bases of recovery after brain injury. *J Commun Disord* 44(5): 515–520.

4. Webster BR, Celnik PA, Cohen LG (2006) Noninvasive brain stimulation in stroke rehabilitation. *NeuroRx* 3(4):474–481.

5. Nishibe M, Barbay S, Guggenmos D, Nudo RJ (2010) Reorganization of motor cortex after controlled cortical impact in rats and implications for functional recovery. *J Neurotrauma* 27(12):2221–2232.

6. Friel KM, et al. (2005) Dissociation of sensorimotor deficits after rostral versus caudal lesions in the primary motor cortex hand representation. *J Neurophysiol* 94(2): 1312–1324.

7. Conner JM, Chiba AA, Tuszyński MH (2005) The basal forebrain cholinergic system is essential for cortical plasticity and functional recovery following brain injury. *Neuron* 46(2):173–179.

8. Nudo RJ, Frost SB (2009) The evolution of motor cortex and motor systems. *Evolutionary Neuroscience*, ed Kaas JH (Academic, Oxford), pp 727–756.

9. Rouiller EM, Moret V, Liang F (1993) Comparison of the connectional properties of the two forelimb areas of the rat sensorimotor cortex: Support for the presence of a premotor or supplementary motor cortical area. *Somatotens Mot Res* 10(3):269–289.

10. Dum RP, Strick PL (2002) Motor areas in the frontal lobe of the primate. *Physiol Behav* 77(4–5):677–682.

11. Dancause N, et al. (2005) Extensive cortical rewiring after brain injury. *J Neurosci* 25(44):10167–10179.

12. Fang PC, Stepniewska I, Kaas JH (2005) Ipsilateral cortical connections of motor, premotor, frontal eye, and posterior parietal fields in a prosimian primate, *Otolemur garnetti*. *J Comp Neurol* 490(3):305–333.

13. Azin M, Guggenmos DJ, Barbay S, Nudo RJ, Mohseni P (2011) A miniaturized system for spike-triggered intracortical microstimulation in an ambulatory rat. *IEEE Trans Biomed Eng* 58(9):2589–2597.

14. Azin M, Guggenmos DJ, Barbay S, Nudo RJ, Mohseni P (2011) A battery-powered activity-dependent intracortical microstimulation IC for brain-machine-brain interface. *IEEE J Solid-State Circuits* 46(4):731–745.

15. Jackson A, Mavoori J, Fetz EE (2006) Long-term motor cortex plasticity induced by an electronic neural implant. *Nature* 444(7115):56–60.

16. Rebesco JM, Miller LE (2011) Stimulus-driven changes in sensorimotor behavior and neuronal functional connectivity application to brain-machine interfaces and neurorehabilitation. *Prog Brain Res* 192:83–102.

17. Hebb DO (1949) *The Organization of Behavior* (Wiley, New York).

18. Shatz CJ (1992) The developing brain. *Sci Am* 267(3):60–67.

19. Rebesco JM, Stevenson IH, Körding KP, Solla SA, Miller LE (2010) Rewiring neural interactions by micro-stimulation. *Front Syst Neurosci* 4:39.

20. Adkins-Muir DL, Jones TA (2003) Cortical electrical stimulation combined with rehabilitative training: Enhanced functional recovery and dendritic plasticity following focal cortical ischemia in rats. *Neurol Res* 25(8):780–788.

21. Plautz EJ, et al. (2003) Post-infarct cortical plasticity and behavioral recovery using concurrent cortical stimulation and rehabilitative training: A feasibility study in primates. *Neurol Res* 25(8):801–810.

22. Plow EB, Carey JR, Nudo RJ, Pascual-Leone A (2009) Invasive cortical stimulation to promote recovery of function after stroke: A critical appraisal. *Stroke* 40(5): 1926–1931.

23. Perez MA, Cohen LG (2009) The corticospinal system and transcranial magnetic stimulation in stroke. *Top Stroke Rehabil* 16(4):254–269.

24. Adkins DL, Hsu JE, Jones TA (2008) Motor cortical stimulation promotes synaptic plasticity and behavioral improvements following sensorimotor cortex lesions. *Exp Neurol* 212(1):14–28.

25. Baba T, et al. (2009) Electrical stimulation of the cerebral cortex exerts antiapoptotic, angiogenic, and anti-inflammatory effects in ischemic stroke rats through phosphoinositide 3-kinase/Akt signaling pathway. *Stroke* 40(11):e598–e605.

26. Henderson AK, Pittman QJ, Teskey GC (2012) High frequency stimulation alters motor maps, impairs skilled reaching performance and is accompanied by an upregulation of specific GABA, glutamate and NMDA receptor subunits. *Neuroscience* 215:98–113.

27. Jahanshahi A, et al. (2013) Electrical stimulation of the motor cortex enhances progenitor cell migration in the adult rat brain. *Exp Brain Res* 231(2):165–177.

28. Edwardson MA, Lucas TH, Carey JR, Fetz EE (2013) New modalities of brain stimulation for stroke rehabilitation. *Exp Brain Res* 224(3):335–358.

29. Bliss TV, Lomo T (1973) Long-lasting potentiation of synaptic transmission in the dentate area of the anaesthetized rabbit following stimulation of the perforant path. *J Physiol* 232(2):331–356.

30. Malenka RC, Bear MF (2004) LTP and LTD: An embarrassment of riches. *Neuron* 44(1): 5–21.

31. Feldman DE (2009) Synaptic mechanisms for plasticity in neocortex. *Annu Rev Neurosci* 32:33–55.

32. Feldman DE (2012) The spike-timing dependence of plasticity. *Neuron* 75(4):556–571.

33. Trepel C, Racine RJ (1998) Long-term potentiation in the neocortex of the adult, freely moving rat. *Cereb Cortex* 8(8):719–729.

34. Racine RJ, Chapman CA, Trepel C, Teskey GC, Milgram NW (1995) Post-activation potentiation in the neocortex. IV. Multiple sessions required for induction of long-term potentiation in the chronic preparation. *Brain Res* 702(1–2):87–93.

35. Hawes SL, Gillani F, Evans RC, Benkert EA, Blackwell KT (2013) Sensitivity to theta-burst timing permits LTP in dorsal striatal adult brain slice. *J Neurophysiol* 110(9): 2027–2036.

36. Skarpaas TL, Morrell MJ (2009) Intracranial stimulation therapy for epilepsy. *Neurotherapeutics* 6(2):238–243.

37. Santos FJ, Costa RM, Tecuapetla F (2011) Stimulation on demand: Closing the loop on deep brain stimulation. *Neuron* 72(2):197–198.

38. Jackson A, Zimmermann JB (2012) Neural interfaces for the brain and spinal cord—Restoring motor function. *Nat Rev Neuro* 8(12):690–699.

39. Nishimura Y, Perlmuter SI, Fetz EE (2013) Restoration of upper limb movement via artificial corticospinal and musculospinal connections in a monkey with spinal cord injury. *Front Neural Circuits* 7:57.

40. Berger TW, et al. (2012) A hippocampal cognitive prosthesis: Multi-input, multi-output nonlinear modeling and VLSI implementation. *IEEE Trans Neural Syst Rehabil Eng* 20(2):198–211.

41. Catani M, Mesulam M (2008) What is a disconnection syndrome? *Cortex* 44(8): 911–913.

42. Committee for the Update of the Guide for the Care and Use of Laboratory Animals (2011) *Guide for the Care and Use of Laboratory Animals* (The National Academies Press, Washington, DC).

43. McCulloch CE, Searle SR (2001) *Generalized, Linear, and Mixed Models* (Wiley, New York).

Linear contrasts of model estimates were used to test for treatment group differences on postlesion days 3, 5, 8, 14, 21, and 28 using *F* tests, with day 28 serving as the a priori time point of interest for the comparison of ADS vs. OLS. Other pairwise comparisons at each time point were also tested (*SI Materials and Methods, Protocol Deviations*). Given the single, a priori primary comparison, no further adjustments for multiple comparisons were made. Linear contrasts were used to generate 95% confidence intervals for each treatment group for those specific days and, within the ADS and OLS groups, to test for differences in the OFF vs. ON conditions. Two-sided *P* values were used for presentation of results.

**ACKNOWLEDGMENTS.** The authors thank Andrea Pack and Alexandra Brown for technical assistance, Cam Teskey for invaluable comments on the discussion, and Casey Wood for artistic contributions. This research was funded by the Department of Defense Traumatic Brain Injury-Investigator-Initiated Research Award Program under Awards W81XWH-10-1-0741/0742 (to P.M. and R.J.N.) and the American Heart Association under Award 09BGIA2280495 (to P.M.). The fabrication costs for the chip in the microdevice were generously supported by the Advanced Platform Technology Center—A Veterans Affairs Research Center of Excellence (Cleveland, OH).

# Real-Time Stimulus Artifact Rejection Via Template Subtraction

Kanokwan Limnuson, *Student Member, IEEE*, Hui Lu, Hillel J. Chiel, and Pedram Mohseni, *Senior Member, IEEE*

**Abstract**—This paper presents an infinite impulse response (IIR) temporal filtering technique for real-time stimulus artifact rejection (SAR) based on template subtraction. A system architecture for the IIR SAR algorithm is developed, and the operation of the algorithm with fixed-point computation is analyzed to obtain the number of bits for the internal nodes of the system, considering dynamic range and fraction length requirements for optimum performance. Further, memory initialization with the first recorded stimulus artifact is proposed and shown to significantly decrease the IIR system response time, especially when artifacts are highly reproducible in consecutive stimulation cycles. The proposed system architecture is hardware-implemented on a field-programmable gate array (FPGA) and tested using two sets of prerecorded neural data from a rat and an *Aplysia californica* (a marine sea slug) obtained from two different laboratories. The measured results from the FPGA verify that the system can indeed remove the stimulus artifacts from the contaminated neural data in real time and recover the neural action potentials that occur on the tail end of the artifact (as close as within 0.5 ms after the artifact spike). The root-mean-square (rms) value of the pre-processed stimulus artifact is reduced on average by a factor of 17 (*Aplysia californica*) and 5.3 (rat) post-processing.

**Index Terms**—Closed-loop neuroprostheses, field-programmable gate array (FPGA), neural recording, neurostimulation, stimulus artifact rejection, template subtraction.

## I. INTRODUCTION

**S**TIMULUS ARTIFACT REJECTION (SAR) is important in biopotential recording, whenever stimulation is performed in the same medium in which the recording electrodes are also placed [1]. This is because the large stimulus artifacts can corrupt or mask the neural activity of interest, either hindering the analysis of stimulus-evoked recorded data [1],

Manuscript received February 24, 2013; revised May 31, 2013; accepted July 14, 2013. Date of publication September 20, 2013; date of current version June 02, 2014. This work was supported by the Department of Defense Traumatic Brain Injury—Investigator-Initiated Research Award Program under Award W81XWH-10-1-0741 (to P. Mohseni) and National Institutes of Health Grant NS047073 (to H. J. Chiel). This paper was recommended by Associate Editor E. M. Drakakis.

K. Limnuson is with the Electrical Engineering and Computer Science Department, Case Western Reserve University, Cleveland, OH 44106 USA.

H. Lu and H. J. Chiel are with the Department of Biology, Case Western Reserve University, Cleveland, OH 44106 USA (e-mail: hjc@case.edu).

P. Mohseni is with the Electrical Engineering and Computer Science Department, Case Western Reserve University, Cleveland, OH 44106 USA, and also with the Advanced Platform Technology (APT) Center—A Veterans Affairs (VA) Research Center of Excellence, Cleveland, OH 44106-1702 USA (e-mail: pedram.mohseni@case.edu).

Color versions of one or more of the figures in this paper are available online at <http://ieeexplore.ieee.org>.

Digital Object Identifier 10.1109/TBCAS.2013.2274574

or limiting the efficacy of activity-dependent stimulation for closed-loop operation [2], [3]. Many SAR techniques have been developed in the past that use the same fundamental principles for rejection, and the choice of a particular method is typically dependent on the type of biopotential that is being recorded and the conditions under which the recording is taking place [4]–[7].

The two primary classes of SAR techniques are the so-called *blanking* and *subtraction* techniques. There are also some other techniques that do not readily fit into one of these two categories [8], [9]. Blanking techniques essentially disconnect the input of the recording amplifier during stimulation. Stimulation-synchronized blanking can be achieved by several methods, including grounding the amplifier input [10], [11], connecting the amplifier input to its output or to that of a sample-and-hold circuit [12], [13], digitally replacing the contaminated signal during the artifact interval with an estimate of the uncontaminated signal [14], and using high-speed auto-zeroing to maintain the amplifier output constant during stimulation [15]. In general, blanking techniques are relatively simple, effective for rejecting large stimulus artifacts, practical for preventing amplifier saturation, and inherently amenable to hardware implementation for real-time SAR. The major drawback is that recording is not viable during stimulation.

Subtraction techniques basically subtract a template signal representative of the stimulus artifacts from the contaminated neural data to remove the artifacts. These techniques do not prevent amplifier saturation on their own and often necessitate running a digital signal processing (DSP) algorithm, rendering them much more complex than the blanking techniques. The major advantage is that these techniques make it possible to retain signal information during stimulation.

Generating an accurate template signal has been the main focus of research in subtraction-based SAR techniques and can be achieved by several methods, including artifact modeling based on locally fitted cubic polynomials [5], capturing the artifact from subthreshold stimulation or from a second recording site remote from the stimulation site [1], and temporal averaging of the contaminated data for multiple consecutive stimulation cycles [16], [17], with the underlying assumption that the overall shape, dynamic range, and timing (e.g., latency with respect to the stimulus timing signal) of the stimulus artifacts do not significantly vary with time.

Subtraction techniques have the potential to fully eliminate the artifacts from the contaminated data record, but have to rely on the generation of an accurate template signal for subtraction, which in turn necessitates an adjustment in the recording amplifier gain or stimulus intensity to enable non-saturated recording

of the full-scale stimulus artifact. On the other hand, providing a low-impedance discharge path for the stimulation electrode using active feedback circuitry [18], [19], as well as careful design of the stimulator in terms of isolation of stimulation channels and parasitic current injection [20] have been previously shown to decrease the duration and amplitude of otherwise-saturating stimulus artifacts. But these approaches cannot fully eliminate the artifacts on their own, suggesting that an optimal solution might be to combine them with the subtraction techniques.

Since subtraction techniques typically require a DSP algorithm for the generation of the template signal, they have traditionally been implemented offline on a home-base computer post-data acquisition. To execute a subtraction-based SAR algorithm in real time (i.e., as the recording is taking place), a suitable template-generation technique should be selected and optimized, realized in hardware, and tested with real neural data, paving the way for ultimately implementing it on a custom integrated circuit (IC).

We have previously assessed the feasibility of hardware implementation of a subtraction-based SAR algorithm using the well-established finite impulse response (FIR) and infinite impulse response (IIR) temporal filtering techniques for template generation [21]. Using MATLAB<sup>TM</sup> simulations, both implementations were shown to be capable of removing stimulus artifacts upon reaching steady-state, with the IIR architecture offering a more favorable tradeoff among performance, computational resources, and power consumption at the expense of its operation speed.

This paper presents our work on hardware implementation of the IIR system proposed in [21] for a real-time SAR algorithm based on template subtraction. The paper is organized as follows. Section II describes the SAR algorithm and the corresponding IIR system architecture, and Section III analyzes its dynamic range and fraction length requirements to determine the number of bits for the internal nodes of the system in fixed-point computation. Section IV describes the implementation of the IIR SAR algorithm on a field-programmable gate array (FPGA), and Section V presents the measured FPGA results using two prerecorded neural datasets. Finally, Section VI draws some conclusions from this work.

## II. SAR ALGORITHM

To generate a template signal representative of the stimulus artifact, temporal filtering is employed in which several properly shifted versions of the input neural data containing the stimulus artifacts are averaged. This is represented by [21]

$$y(t) = \sum_{n=0}^{N-1} a(n) \cdot x(t - nT_{sti}) \quad (1)$$

where  $y(t)$  is the estimated template signal,  $x(t)$  is the input neural data containing the stimulus artifacts,  $N$  is the number of stimulus artifact waveforms used for template estimation,  $a(n)$  are averaging factors that should sum up to unity for the stimulus artifact and  $y(t)$  to have the same amplitude (e.g.,  $a(n)$  factors can be all equal to  $1/N$  for standard averaging), and  $T_{sti}$  is the stimulation period. It should be noted that the stimulation

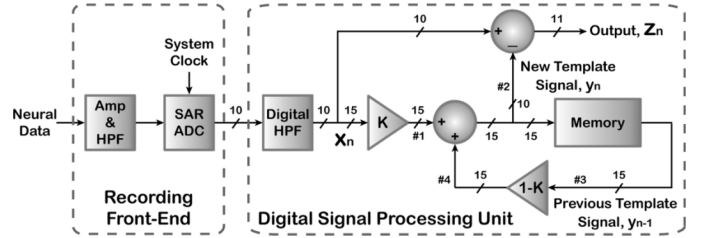


Fig. 1. System architecture for the IIR implementation of the template subtraction-based SAR algorithm. The number of bits in internal operation of the algorithm is also shown.

occurrence does not necessarily have to be periodic for correct operation of the SAR algorithm, as long as it is predictable via a stimulus timing signal.

An FIR implementation of (1) was previously shown to require at least  $N - 1$  memory rows and  $N$  summations in each period of the sampling clock, whereas the IIR implementation would require a single memory row and only three summations at the expense of much longer system response time [21]. Initializing the memory with the first recorded artifact can significantly decrease the IIR system response time for creating an accurate artifact template signal [22]. Therefore, this paper focuses on the IIR implementation of the SAR algorithm with memory initialization.

Fig. 1 depicts the system architecture, comprising neural-recording front-end circuitry for signal conditioning and a DSP unit for executing the SAR algorithm. The recording front-end provides ac amplification, dc input stabilization, bandpass filtering, and 10b digitization of the recorded neural signal with fully programmable gain and bandwidth, similar to what has previously been shown in [3]. The DSP unit, which is the focus of this paper, provides additional highpass filtering using an IIR digital filter with adjustable bandwidth to remove any residual dc offsets or low-frequency noise, and performs real-time stimulus artifact rejection using template subtraction. Based on Fig. 1:

$$y_n = (1 - K) \cdot y_{n-1} + K \cdot x_n \quad (2)$$

where  $y_n$  is the new artifact template signal,  $y_{n-1}$  is the previous template signal, and  $x_n$  is the input neural data. Therefore, in the IIR implementation, the stimulus artifact template signal is retained in the memory, and a new template signal is generated from the previous template signal and the input neural data according to (2), which is then subtracted from the input neural data. The factor  $K$  ( $<1$ ) plays a similar role to  $N$  in (1), affecting the IIR system response time and accuracy. As shown in the Appendix, it can be derived from (2) that the minimum number of stimulus artifacts,  $m$ , required to generate an accurate template signal with error less than, e.g., 0.1% is

$$m > \frac{-3 - \log_{10} |1 - Y_0|}{\log_{10}(1 - K)} \quad (3)$$

where  $Y_0$  is the initial condition of the memory normalized to the steady-state artifact template signal. Fig. 2 shows a plot of  $m$

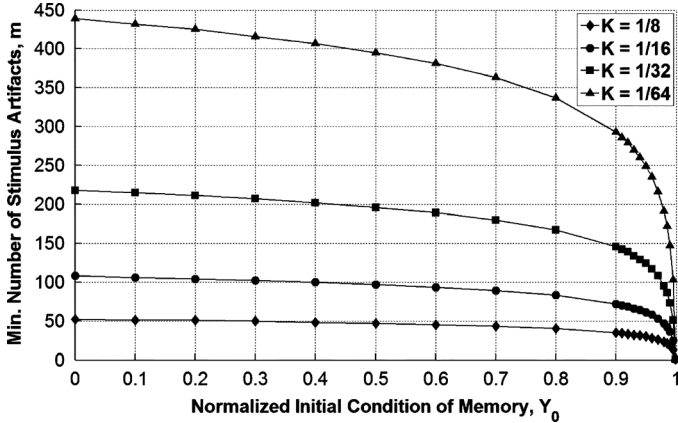


Fig. 2. Minimum number of stimulus artifacts required to generate an accurate template signal with error  $<0.1\%$  as a function of the normalized initial condition of the memory ( $Y_0 < 1$ ) for four different values of  $K$ .

versus  $Y_0$  for four different values of  $K$ . Clearly, the closer the initial condition is to the steady-state template signal, the faster the system response time, showing that the IIR implementation is particularly effective when stimulus artifacts in consecutive stimulation cycles are reproducible. In this work, the factor  $K$  is selected to be either 1/16 or 1/32, which also allows implementing the multiplication-by-  $K$  function via a shift to the right by 4b or 5b, respectively, obviating the need for digital multipliers.

It is worth noting that the artifact template generation technique in (2) performed by the proposed IIR system is in essence an exponentially weighted moving average (EWMA) [23], a statistic tool with a rich history in process monitoring and quality control charting [24], [25] as well as economics [26] and industrial quality control [27]. In this paper, we utilize a real-time implementation of the EWMA for a novel application in neural signal processing. Section III discusses the performance of the IIR SAR algorithm with fixed-point computation and provides a framework for determining the optimum number of bits in internal operation of the algorithm.

### III. SAR ALGORITHM WITH FIXED-POINT COMPUTATION

When template calculations are performed with floating-point precision, similar to when the SAR algorithm is executed offline in MATLAB<sup>TM</sup> on a home-base computer post-data acquisition, the output can be very accurate. However, for *real-time* execution of the algorithm in hardware, fixed-point computation is preferred for simplicity, which then raises concerns about the template signal accuracy due to quantization noise. In this section, we find the optimum number of bits in internal operation of the SAR algorithm by analyzing the dynamic range and fraction length requirements.

In IIR systems, the internal nodes of the structure can potentially overflow, necessitating an adjustment in their dynamic range to satisfy the L1-norm criteria for preventing an overflow [28]–[30]. In Fig. 1, consider the signal path from the input neural data (i.e.,  $x_n$ ) to each of the four internal nodes of the algorithm (i.e., nodes #1–4). Assume the resulting transfer functions and corresponding impulse responses are  $F_i(z)$  and  $f_i[n]$ ,

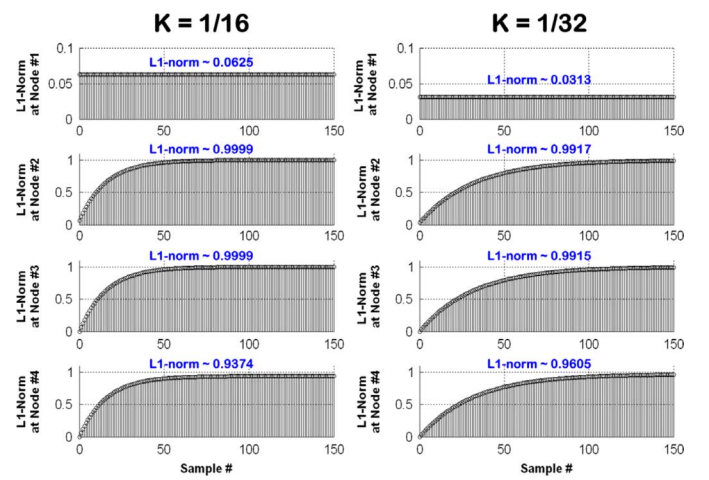


Fig. 3. L1-norm estimates at nodes #1–4 for the two selected values of  $K$ .

respectively. Modeling the memory block as a unit delay, it can be shown that

$$\begin{aligned} F_1(z) &= K \\ F_2(z) &= \frac{K}{1 - (1 - K)z^{-1}} \\ F_3(z) &= \frac{Kz^{-1}}{1 - (1 - K)z^{-1}} \\ F_4(z) &= \frac{K(1 - K)z^{-1}}{1 - (1 - K)z^{-1}}. \end{aligned} \quad (4)$$

Fig. 3 depicts the L1-norm estimates of the four transfer functions for the two selected values of  $K$ , where L1-norm is

$$\|f\|_1 = \sum_{n=0}^{\infty} |f[n]|. \quad (5)$$

As can be seen in all cases, the L1-norm estimates are less than one, indicating that no additional bits (equal to  $\log_2 \|f\|_1$ ) are needed beyond 10b for the internal nodes to avoid overflow. The SAR algorithm output node ( $z_n = x_n - y_n$ ) has higher dynamic range of 11b to prevent the saturation of the output after subtraction, in case of an overflow/underflow.

Next, to assess the impact of quantization noise induced by fixed-point computation on template signal accuracy, we determine the signal-to-noise ratio (SNR) in template signal generation as a function of the fraction length for the internal nodes (i.e., number of additional bits beyond 10b in a word-length). Fig. 4 shows the simulation structure for comparing the performance of the SAR algorithm with fixed-point computation versus that with floating-point computation by determining the SNR [31].  $Q_1$  and  $Q_2$  are two quantizers that quantize their inputs to the word-length value, whereas  $Q_3$  quantizes its input to 10b. Fig. 5 depicts the simulated SNR and effective number of

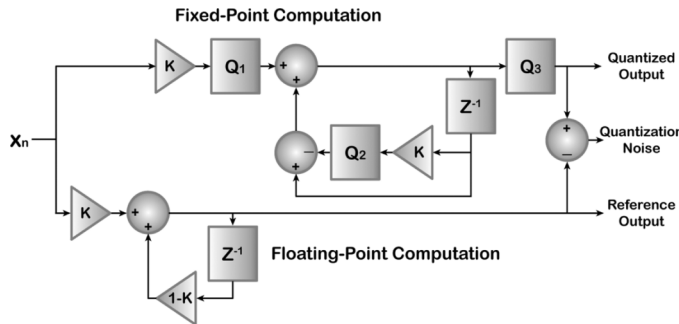


Fig. 4. Simulation structure for determining the SNR in template signal generation.

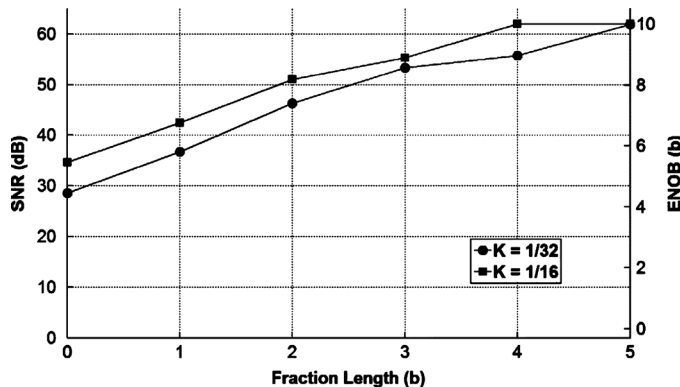


Fig. 5. Simulated SNR and ENOB of template signal generation in the IIR SAR algorithm with fixed-point computation versus the fraction length for the two selected values of  $K$ .

bits, ENOB, in template signal generation for the two selected values of  $K$ , where the SNR is defined as

$$\text{SNR} = 20 \log_{10} \frac{S_{\text{out},\text{rms}}}{N_{Q,\text{rms}}} \quad (6)$$

with  $S_{\text{out}}$  and  $N_Q$  representing the reference output and quantization noise, respectively. Input  $x_n$  is taken to be a 10b-digitized sinusoidal signal with rail-to-rail amplitude (i.e., -512 to 511 in two's complement format) and a frequency of 0.1 mHz to capture the underlying assumption that the stimulus artifacts do not change rapidly with time. Assuming a stimulation frequency of 1 Hz,  $x_n$ 's sampling frequency is also 1 Hz. Clearly, the system requires a fraction length of 5b to achieve  $\sim 10$ b accuracy in template signal generation with  $K = 1/32$ . A lower fraction length would increase the quantization noise and degrade the accuracy to  $< 10$ b, whereas a higher fraction length not only would increase the requisite hardware resources to support larger memory size, but also would not offer any significant benefit given that by design the overall system performance would be limited by that of the neural-recording front-end [3], and not the DSP unit. Taking into account these considerations related to dynamic range and fraction length requirements, the selected number of bits for the internal operation of the SAR algorithm is shown in Fig. 1.

#### IV. FPGA IMPLEMENTATION

The DSP unit in Fig. 1, comprising the digital highpass filter (HPF) and the SAR algorithm circuitry, has been implemented on an FPGA using the DE2 Development and Educational Board, which has the Cyclone II device by *Altera* as its FPGA platform. Fig. 6 depicts the architecture of the DSP unit in FPGA implementation, which incorporates a 68b parameter register, a digital control unit, and a DSP core. The parameter register is used to store the user-selectable parameters for system operation such as the bandwidth setting of the digital HPF and factor  $K$  in the SAR algorithm, as well as memory initialization, memory length, and output-blanking settings. The memory length (i.e., number of 16b samples) is determined by the sampling clock frequency and the stimulus artifact duration. If needed, the blanking feature is used after template subtraction to remove any residual artifacts in the output around the rising and falling edges of the artifact where it rapidly changes with time [21]. The parameter register is implemented as a standalone circuit block with its own timing and control operation, which is separate from that of the other circuit blocks and applied externally. This is because this block is loaded with the requisite system parameters only once prior to the experiment and is not synchronously clocked with the rest of the circuit during SAR algorithm operation.

The digital control unit incorporates counters and finite-state machines and provides timing, path, and blanking control signals for the DSP core. The required inputs for the digital control unit include a stimulus timing signal, system clock and sampling clock signals, and system parameters such as memory length, memory initialization, and blanking settings.

The DSP core incorporates a digital HPF, circuitry to execute the SAR algorithm, and parallel-to-serial converters at the output. The required inputs for the DSP core include the amplified/digitized neural signal (10b), system clock signal, and control signals provided by the digital control unit. Fig. 6 also shows the structure of the digital HPF and SAR algorithm circuitry in the DSP core as implemented on the FPGA. The amplified/digitized input neural signal is first highpass filtered using a 1st-order, IIR filter with direct form II architecture. Factor  $K_1$  is the user-selected HPF coefficient that controls the filter bandwidth and is selected judiciously to perform the filtering using arithmetic shifts, subtraction and addition only, with no need for digital multipliers or dividers [3]. The user can set  $K_1$  to be either 1/16 or 1/8, which results in a filter cutoff frequency of 366 Hz or 756 Hz, respectively, from a 1-MHz system clock. Since the digitized data at the analog-to-digital converter (ADC) output are unsigned numbers (10b), a factor of 512 is subtracted from the input signal to convert it to two's complement format for further processing. In addition, an overflow/underflow detector is used at the HPF output to limit its dynamic range to 10b before feeding it to the SAR algorithm circuitry.

The SAR algorithm only operates for the duration of each stimulus artifact. The digitized/filtered sample at the output of the HPF filter (10b) is first converted to 15b via a shift to the left by 5b and then multiplied by factor  $K_2$  (same as  $K$  in Fig. 1) stored in the parameter register. Next, the memory data containing the previous template signal are read, multiplied by

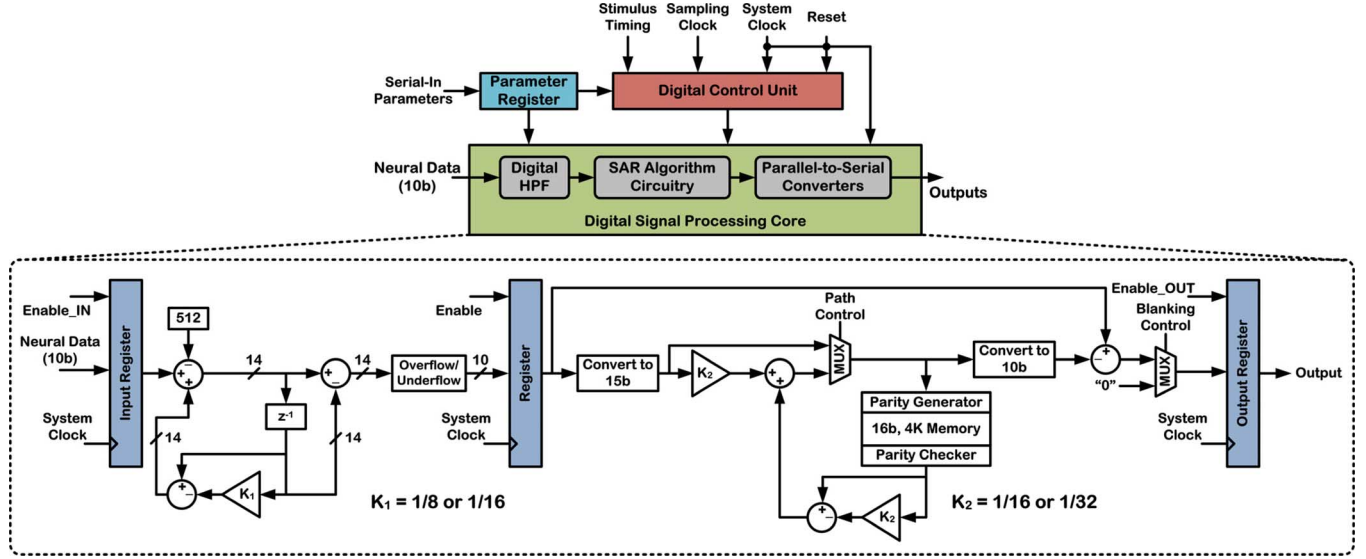


Fig. 6. Architecture of the DSP unit (top) and structure of the digital HPF and SAR algorithm circuitry in the DSP core (bottom) as implemented on the FPGA.

$(1 - K_2)$ , and added to  $(K_2 \cdot x_n)$  to obtain the new template signal (15b), which is written back into the memory for the next cycle. The new template signal is also converted back to 10b and subsequently subtracted from the 10b digitized/filtered input sample to produce the SAR algorithm output signal. Outside the duration of the stimulus artifact, the SAR algorithm circuitry is disabled and the digitized/filtered sample at the HPF output is directly passed to the output register.

The path control signal from the digital control unit manages the memory initialization. Specifically, if the recorded stimulus artifact is the first artifact, indicated as such by the stimulus timing signal, the path control signal routes the 15b sample directly to the memory input for its initialization. With the next indication of stimulation by the stimulus timing signal, the IIR system executes the SAR algorithm as previously described. If the memory initialization setting is not enabled by the user, the memory can be cleared to start with zero internal values, but this would increase the IIR system response time as previously shown in Fig. 2.

The 16b, 4K memory is implemented using the internal SRAM of the FPGA. Even parity is used to check for memory error, which is generated by an *XOR* function of all the bits in each 15b sample. The parity bit is then added to the end of the data bits before being written into the memory as a 16b sample. When the memory data are read out, a parity checker checks for memory error, and this information is sent to the output. The 15b sample is also sent to the rest of the SAR algorithm circuitry for template generation. Including the memory parity check feature, while not entirely necessary for an FPGA-based system, would streamline the design translation from an FPGA to an IC platform in the future.

The blanking control signal, which is also received from the digital control unit, is used to remove any residual artifacts in the output after template subtraction. Specifically, this control signal activates a multiplexer that replaces the output data with “0” for the time period in which blanking is applied, which is normally at the rising and falling edges of the artifact where it

rapidly changes with time. The user can independently set the blanking duration around the rising and falling edges from 0 (i.e., no blanking) to 2,047 data points.

The three registers in Fig. 6 are used for pipelining in order to overlap the processing in each stage and prevent harmful race conditions with proper timing control. Further, since the SAR algorithm circuitry operates synchronously with a system clock, all circuit blocks (except the parameter register) share the same system clock signal globally and use a local *Enable* signal for synchronization [32].

## V. FPGA MEASUREMENT RESULTS

The DSP unit as depicted in Fig. 6 has been synthesized and mapped to the Cyclone II FPGA, EP2C35F672C6, using Altera’s Quartus II design software. The mapped circuitry consumed 2% (656) of the total available logic elements (LEs) and 14% (65,536) of the total available memory bits. The DE2 board was programmed and connected to a digital data acquisition (DAQ) card, NI 6541, which provided the input signal to the FPGA and recorded the output waveforms. The system clock was applied to the FPGA using the onboard external clock port, and a supply of 9 V was used to power up the board with its input-output (I/O) ports at 3.3 V. For all FPGA measurements described below, factors  $K_1$  and  $K_2$  (see Fig. 6) were both set to 1/16.

Two sets of prerecorded neural data from two different laboratories were used to experimentally verify the operation of the IIR SAR algorithm and its FPGA implementation. Specifically, a 294-s window of prerecorded neural data from a rat was used as the first dataset. The rat data were sampled at  $\sim 24.4$  kHz and obtained during 4-Hz cortical stimulation. A gain of 520 ( $\sim 54.3$  dB) was applied to the neural data before feeding it to the FPGA. The SAR algorithm was set to operate for 5 ms upon receiving an indication of stimulation by the stimulus timing signal, and no output blanking was applied.

A 125-s window of prerecorded data from an *Aplysia californica* (a marine sea slug) was used as the second neural dataset.

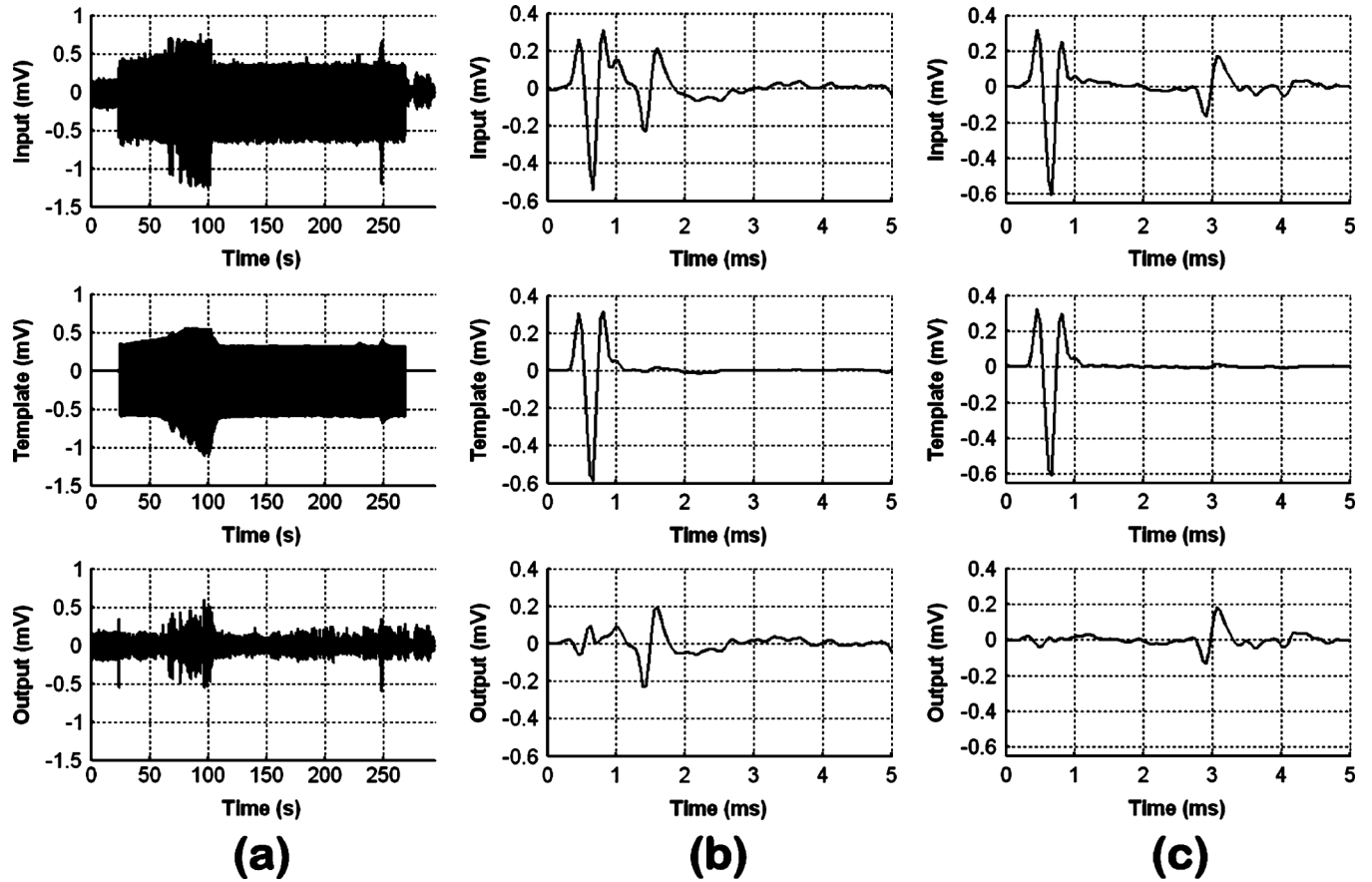


Fig. 7. FPGA measurement results using prerecorded neural data from a laboratory rat. (a) Top plot shows a 294-s window of the input data to the FPGA. Middle plot depicts the generated stimulus artifact template signal, whereas the bottom plot shows the IIR system output from the FPGA. Two 5-ms snapshots of the waveforms are shown at (b)  $t = \sim 208$  s and (c)  $t = \sim 256$  s.

The *Aplysia* data were sampled at 2 kHz and obtained during 0.5-Hz stimulation. A gain of 1,000 (60 dB) was applied to the neural data before feeding it to the FPGA. Upon receiving an indication of stimulation by the stimulus timing signal, the SAR algorithm was set to operate for 96 ms (the duration of stimulus artifact in the *Aplysia* dataset was much longer than that in the rat dataset), and output blanking was set to occur for 4 ms synchronized with the rising and falling edges of the stimulus timing signal. The applied gain values represented those previously obtained with our neural-recording front-end operating from 1.5 V [3]. The gain values were high enough to achieve sufficient resolution at the DSP unit input, while keeping the amplitude of the amplified neural data below  $1.5 \text{ V}_{\text{pp}}$ .

Fig. 7 shows the FPGA measurement results using the rat neural dataset. The top plot in (a) depicts the input neural data to the FPGA, consisting of neural spikes buried in large stimulus artifacts. The middle plot shows the generated artifact template signal after memory initialization as previously described. Note the fast response time of the IIR SAR algorithm in quickly generating the template signal even for the initial stimulus artifacts, as well as how fast the generated template signal tracks the variation in stimulus artifact amplitude in the first 100 seconds. The bottom plot depicts the IIR system output from the FPGA in which the large stimulus artifacts are rejected and the neural data recovered in real time.

Fig. 7(b) and (c) depict 5-ms snapshots of the waveforms at  $t = \sim 208$  s and  $\sim 256$  s, respectively, demonstrating that the system is fully capable of recovering neural action potentials that occur on the tail end of the artifact [see Fig. 7(c)] or appear as close as within 0.5 ms after the artifact spike [see Fig. 7(b)].

The slight discrepancy between the amplitude of the input artifact and that of the template signal is because the template signal actually represents the highpass filtered artifact.

Fig. 8 shows a 5-s snapshot of the waveforms in Fig. 7(a) around the onset of stimulation and their corresponding spectrograms obtained using 1,024-sample windows with 1,000-sample overlap. As can be seen in the top and middle spectrograms, the artifacts in the rat neural dataset have strong frequency components below 5 kHz that are significantly reduced in the output (see the bottom spectrogram), allowing the weaker neural activity to emerge from the large artifacts. For the very first stimulus artifact at just prior to  $t = 2.5$  s, which is the one loaded into the memory for its initialization, the corresponding template signal would be 1/16th of the artifact according to (2), and therefore 15/16th of the artifact appears in the output data after subtraction. The IIR SAR algorithm then removes all the subsequent stimulus artifacts starting with the second one. If present, artifact residuals as seen in Figs. 7(b) and (c) in the time domain and Fig. 8 in the frequency domain (bottom spectrogram) are now insignificant as compared to the neural action potentials.

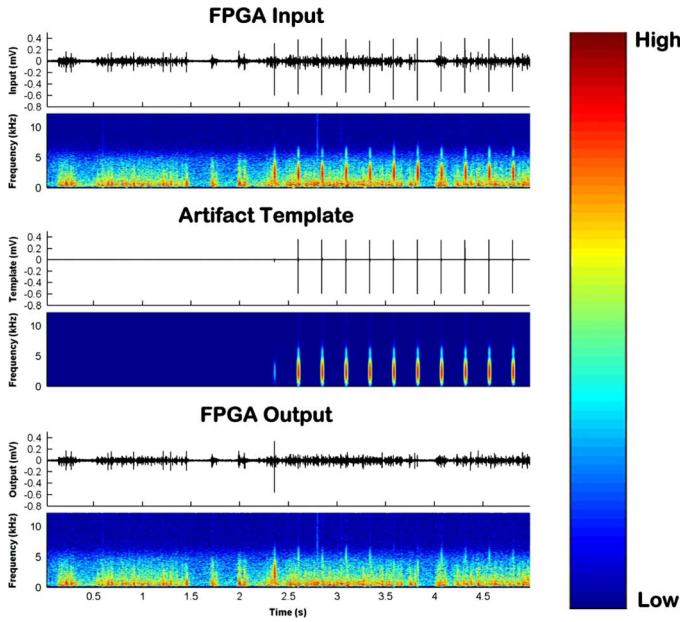


Fig. 8. A 5-s snapshot of the FPGA measurement results using the prerecorded rat neural dataset and their corresponding spectrograms. The 5-s snapshot is taken around the stimulus onset.

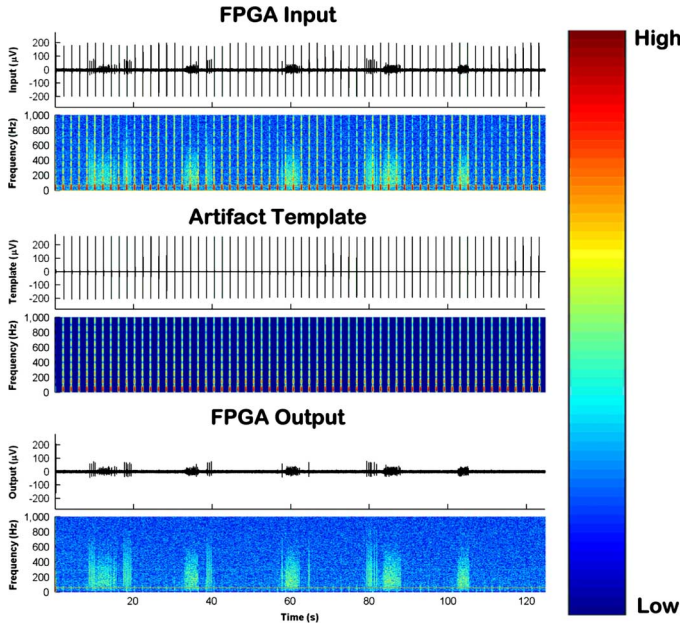


Fig. 9. FPGA measurement results using the prerecorded *Aplysia* neural dataset and their corresponding spectrograms.

Fig. 9 shows the FPGA measurement results using the *Aplysia* neural dataset and their corresponding spectrograms. The top plot depicts the input neural data to the FPGA, containing many large stimulus artifacts that occur at 0.5 Hz and bursts of extracellular neural activity that occur in between and occasionally on the tail end of the artifacts. The middle plot shows the generated artifact template signal and its spectrogram, indicating that the artifacts have their frequency components spread throughout a 1-kHz bandwidth with strong frequency components contained below 200 Hz. The bottom plot shows the FPGA output data after blanking in which all

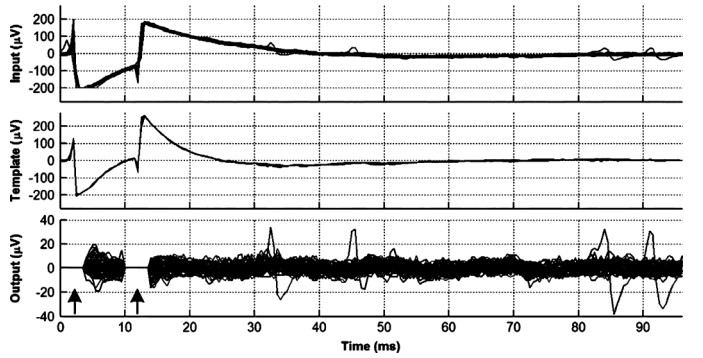


Fig. 10. Top plot shows a 96-ms portion of the *Aplysia* neural dataset, showing a total of 61 unfiltered stimulus artifacts superimposed on each other with some action potentials riding on the tail end of the artifacts. Middle plot depicts the 61 stimulus artifact templates superimposed on each other, which actually represent the highpass filtered artifacts (not shown). Bottom plot shows the artifact-free FPGA output in which the neural spikes are recovered after template subtraction. Residual artifacts are also simultaneously removed after 4-ms blanking (arrows). Note the smaller dynamic range of the Y-axis in the bottom plot after artifact removal and residual blanking.

stimulus artifacts (minus the first one as explained previously) are successfully removed from the recorded data in real time to recover the neural activity.

Fig. 10 shows a close-up view of the waveforms during the 96-ms period of operation for the SAR algorithm. The top plot depicts 61 unfiltered stimulus artifacts superimposed on each other (i.e., all the artifacts present in the 125-s window of *Aplysia* neural dataset minus the very first one), with some action potentials also occurring on the tail end of the artifacts. The middle plot shows the corresponding artifact templates superimposed on each other, whereas the bottom plot depicts the artifact-free IIR system output from the FPGA after template subtraction and 4-ms blanking (arrows) for simultaneous removal of the artifacts and artifact residuals, respectively, demonstrating successful operation of the algorithm and its hardware implementation.

In order to assess the performance of the IIR SAR algorithm and its hardware implementation in a quantitative manner, a total of 908 stimulus artifacts (54 of 62 and 854 of 1,000 artifacts in the *Aplysia* and rat neural datasets, respectively) were analyzed. Specifically, the mean and standard deviation of the root-mean-square (rms) values of the artifacts were computed pre- and post-processing by the FPGA.

The analysis excluded the very first artifact in each neural dataset and those artifacts that had action potentials present anywhere in their duration over which the algorithm was operating (96 ms and 5 ms for the *Aplysia* and rat artifacts, respectively). This ensured that the occasional presence of action potentials did not confound the analysis. The same statistics were also obtained from segments of the FPGA output that represented pure noise (i.e., absence of both action potentials and artifact residuals). Table I tabulates the results of this analysis. In the case of *Aplysia* neural dataset that contains relatively stationary stimulus artifacts (see the top plot in Fig. 9 and note the small standard deviation value in Table I), the rms value of the artifact on average is reduced by a factor of 17, resulting in post-processed rms values that are at the level of that for the output

TABLE I  
STATISTICS OF PRE- AND POST-PROCESSED STIMULUS ARTIFACTS

<i>Aplysia californica</i> (54 of 62 SAs)		
	Mean ( $\mu\text{V}_{\text{rms}}$ )	SD ( $\mu\text{V}_{\text{rms}}$ )
<b>Pre-Processing</b>	68.33	1.21
<b>Post-Processing</b>	4.01	0.68
<b>Output Noise</b>	3.83	0.16
<i>Rat</i> (854 of 1,000 SAs)		
<b>Pre-Processing</b>	115.74	21.72
<b>Post-Processing</b>	21.65	16.70
<b>Output Noise</b>	5.03	0.46

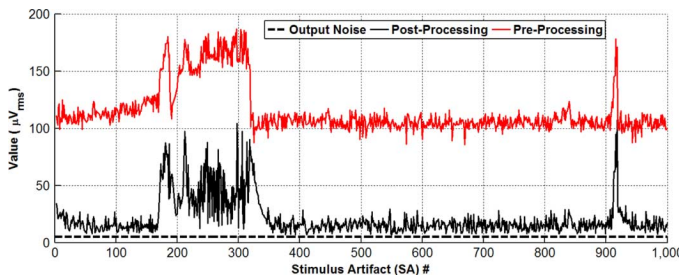


Fig. 11. Root-mean-square (rms) value of the stimulus artifacts (854 of 1,000) in the rat neural dataset pre- and post-processing by the FPGA. The dashed line represents an average rms value of  $5.03 \mu\text{V}$  for the output noise obtained from 10 different 5-ms segments that did not contain any action potentials or artifact residuals.

noise. In the case of rat neural dataset that contains both stationary and non-stationary artifacts (see the top plot in Fig. 7(a) and note the larger standard deviation value in Table I), the reduction in the rms value on average is more modest (a factor of 5.3). A closer look at the rms values of individual stimulus artifacts pre- and post-processing reveals that the degradation of performance is limited to when there is a sudden change in the artifacts (see Fig. 11 and compare its trend with how the artifacts are changing in the top plot of Fig. 7(a)), whereas the rms values of the post-processed artifacts indeed approach that of the output noise when the artifacts are relatively stationary.

## VI. CONCLUSION

This paper reported on a neural signal-processing algorithm for real-time stimulus artifact rejection (SAR) in which a high-fidelity template signal representative of the stimulus artifacts was first generated via temporal filtering and subsequently subtracted from the contaminated neural data to remove the artifacts. A system architecture for the IIR implementation of the algorithm was realized in hardware on an FPGA platform, featuring memory initialization as a simple method to significantly decrease the IIR system response time for accurate template generation. The measured FPGA results using two sets of prerecorded neural data from a rat and an *Aplysia californica* verified the functionality of the algorithm and its hardware implementation by removing the stimulus artifacts in real time from the contaminated recorded data and recovering the extracellular neural activity.

The major advantage of this approach as compared to the blanking techniques (i.e., disconnecting the recording amplifier

input during stimulation) is that it has the potential to retain signal information during stimulation while fully eliminating the artifacts from the contaminated data record in real time. On the other hand, one limitation of this approach is that it does not directly address the problem of amplifier saturation and hence becomes less effective with prolonged amplifier saturation, unless care is taken in the design of the recording and stimulating circuitry to prevent (or at least minimize) amplifier saturation by decreasing the duration and amplitude of the artifacts [18]–[20]. Another limitation of this approach is that if neural activity occurs on the tail end of the artifact and is time-locked to stimulation, it will be removed by the system along with the artifacts. Similarly, if neural activity occurs during the rising/falling edges of the artifact spike, it will be lost, because it will be either blanked out by the system or heavily distorted by the residuals with no blanking.

This technique can potentially handle other stimulation scenarios as well, given that it only needs the stimulus timing signal information for correct operation. For example, if stimulation occurs *simultaneously* on two electrodes, a *combined* stimulus artifact might appear on the recording electrode that can be removed even by the current system. If stimulation occurs *alternately* on two electrodes, two different stimulus artifact types might appear *alternately* as well on the recording electrode and can be removed by modifying the timing operation of the system to handle each artifact type independently, if there is no temporal overlap between the artifacts. Ultimately, a tradeoff exists between functional versatility and system operation complexity.

Finally, given the relatively low system clock frequency of  $\leq 1 \text{ MHz}$  in this work and that the synthesized algorithm utilized a very small percentage of the available FPGA resources, it was not readily feasible to accurately determine the power consumption in hardware implementation. Efforts are currently under way for custom implementation of the DSP unit in Fig. 1 on an IC that would also incorporate recording front-end and stimulating back-end circuitry adapted from [3] to form a complete system. To that end, our preliminary work shows that the DSP unit can be implemented with a total area of  $3.64 \text{ mm}^2$  (89% occupied by the 16b, 4K SRAM) in  $0.35\text{-}\mu\text{m}$  CMOS technology with power consumption on the order of low-tens of microwatts from  $1.5 \text{ V}$  (1-MHz system clock), indicating the feasibility of running the algorithm on a miniaturized, integrated device in the near future.

## APPENDIX

In this Appendix, we show the derivation of (3) in Section II: SAR Algorithm. As previously stated, based on Fig. 1

$$y_n = (1 - K) \cdot y_{n-1} + K \cdot x_n \quad (\text{A1})$$

where  $n = 1, 2, 3, \dots$ . Hence, it is simple to see that

$$y_1 = (1 - K) \cdot y_0 + K \cdot x_1$$

$$y_2 = (1 - K) \cdot y_1 + K \cdot x_2$$

$$= (1 - K)^2 \cdot y_0 + K \cdot (1 - K) \cdot x_1 + K \cdot x_2 \quad (\text{A2})$$

which means that the template signal for the  $m$ th artifact can be written as

$$y_m = (1 - K)^m \cdot y_0 + K \cdot [x_m + (1 - K) \cdot x_{m-1} + \cdots + (1 - K)^{m-1} \cdot x_1] \quad (\text{A3})$$

where  $y_0$  is the initial condition of the memory. Assume that  $x_1, x_2, \dots, x_m$  are all equal to the steady-state artifact template signal,  $y_{ss}$ . Therefore

$$\frac{y_m}{y_{ss}} = (1 - K)^m \cdot Y_0 + K \cdot [1 + (1 - K) + \cdots + (1 - K)^{m-1}] \quad (\text{A4})$$

where  $Y_0 = (y_0)/(y_{ss})$  is the initial condition of the memory normalized to the steady-state artifact template signal. Given the sum of geometric series, it can be shown that

$$\begin{aligned} 1 + (1 - K) + \cdots + (1 - K)^{m-1} \\ = \frac{1 - (1 - K)^m}{1 - (1 - K)} \\ = \frac{1 - (1 - K)^m}{K} \end{aligned} \quad (\text{A5})$$

which means that (A4) can be simplified to

$$\frac{y_m}{y_{ss}} = (1 - K)^m \cdot Y_0 + 1 - (1 - K)^m. \quad (\text{A6})$$

If  $Y_0 < 1$ , for generating an accurate template signal with error less than, e.g., 0.1%, one needs to have  $(y_m)/(y_{ss}) > 0.999$ , which means  $(1 - K)^m \cdot (1 - Y_0) < 0.001$  from (A6). Taking a logarithm of both sides and noting that  $\log_{10}(1 - K) < 0$ , one can obtain

$$m > \frac{-3 - \log_{10}(1 - Y_0)}{\log_{10}(1 - K)}. \quad (\text{A7})$$

If  $Y_0 > 1$ , for generating an accurate template signal with error less than 0.1%, one needs to have  $(y_m)/(y_{ss}) < 1.001$ , which ultimately leads to

$$m > \frac{-3 - \log_{10}(Y_0 - 1)}{\log_{10}(1 - K)}. \quad (\text{A8})$$

#### ACKNOWLEDGMENT

The authors would like to thank Dr. D. Guggenmos and Prof. R. Nudo, Kansas University Medical Center, Kansas City, KS, USA, for providing the prerecorded rat neural dataset. The authors would also like to thank Dr. M. Azin, QualComm, San Diego, CA, USA, and Prof. M. Buchner, Case Western Reserve

University, Cleveland, OH, USA, for helpful discussions that made this work possible.

#### REFERENCES

- [1] K. C. McGill *et al.*, "On the nature and elimination of stimulus artifact in nerve signals evoked and recorded using surface electrodes," *IEEE Trans. Biomed. Eng.*, vol. BME-29, no. 2, pp. 129–137, Feb. 1982.
- [2] M. Azin, D. J. Guggenmos, S. Barbay, R. J. Nudo, and P. Mohseni, "A miniaturized system for spike-triggered intracortical microstimulation in an ambulatory rat," *IEEE Trans. Biomed. Eng.*, vol. 58, no. 9, pp. 2589–2597, Sep. 2011.
- [3] M. Azin, D. J. Guggenmos, S. Barbay, R. J. Nudo, and P. Mohseni, "A battery-powered activity-dependent intracortical microstimulation IC for brain-machine-brain interface," *IEEE J. Solid-State Circuits*, vol. 46, no. 4, pp. 731–745, Apr. 2011.
- [4] B. H. Boudreau, K. B. Englehart, A. D. C. Chan, and P. A. Parker, "Reduction of stimulus artifact in somatosensory evoked potentials: Segmented versus subthreshold training," *IEEE Trans. Biomed. Eng.*, vol. 51, no. 7, pp. 1187–1195, Jul. 2004.
- [5] D. A. Wagenaar and S. M. Potter, "Real-time multichannel stimulus artifact suppression by local curve fitting," *J. Neurosci. Methods*, vol. 120, no. 2, pp. 113–120, Oct. 2002.
- [6] H. Liang and Z. Lin, "Stimulus artifact cancellation in the serosal recordings of gastric myoelectric activity using wavelet transform," *IEEE Trans. Biomed. Eng.*, vol. 49, no. 7, pp. 681–688, Jul. 2002.
- [7] V. Parsa, P. A. Parker, and R. N. Scott, "Adaptive stimulus artifact reduction in noncortical somatosensory evoked potential studies," *IEEE Trans. Biomed. Eng.*, vol. 45, no. 2, pp. 165–179, Feb. 1998.
- [8] A. Demosthenous, J. Taylor, I. F. Triantis, R. Rieger, and N. Donaldson, "Design of an adaptive interference reduction system for nerve-cuff electrode recording," *IEEE Trans. Circuits Syst. I, Reg. Papers*, vol. 51, no. 4, pp. 629–639, Apr. 2004.
- [9] R. Vigario, J. Sarela, V. Jousmaki, M. Hamalainen, and E. Oja, "Independent component approach to the analysis of EEG and MEG recordings," *IEEE Trans. Biomed. Eng.*, vol. 47, no. 5, pp. 589–593, May 2000.
- [10] V. Sharma, D. B. McCreery, M. Han, and V. Pikov, "Bidirectional telemetry controller for neuroprosthetic devices," *IEEE Trans. Neural Syst. Rehabil. Eng.*, vol. 18, no. 1, pp. 67–74, Feb. 2010.
- [11] Z. M. Nikolic, D. B. Popovic, R. B. Stein, and Z. Kenwell, "Instrumentation for ENG and EMG recordings in FES systems," *IEEE Trans. Biomed. Eng.*, vol. 41, no. 7, pp. 703–706, Jul. 1994.
- [12] F. Shahrokhi, K. Abdelhalim, D. Serletis, P. L. Carlen, and R. Genov, "The 128-channel fully differential digital integrated neural recording and stimulation interface," *IEEE Trans. Biomed. Circuits Syst.*, vol. 4, no. 3, pp. 149–161, Jun. 2010.
- [13] H. Jadvar and D. W. Benson, Jr., "A stimulus artifact suppressor for esophageal pacing studies: Design and clinical testing," in *Proc. 11th Annu. Int. IEEE Eng. Med. Biol. Conf.*, 1989, pp. 1401–1402.
- [14] A. E. Hines, P. E. Crago, G. J. Chapman, and C. Billian, "Stimulus artifact removal in EMG from muscles adjacent to stimulated muscles," *J. Neurosci. Methods*, vol. 64, no. 1, pp. 55–62, Jan. 1996.
- [15] G. DeMichele and P. R. Troyk, "Stimulus-resistant neural recording amplifier," in *Proc. 25th Annu. Int. IEEE Eng. Med. Biol. Conf.*, 2003, pp. 3329–3332.
- [16] T. Hashimoto, C. M. Elder, and J. L. Vitek, "A template subtraction method for stimulus artifact removal in high-frequency deep brain stimulation," *J. Neurosci. Methods*, vol. 113, pp. 181–186, 2002.
- [17] T. Wichmann, "A digital averaging method for removal of stimulus artifacts in neurophysiologic experiments," *J. Neurosci. Methods*, vol. 98, pp. 57–62, 2000.
- [18] E. A. Brown, J. D. Ross, R. A. Blum, Y. Nam, B. C. Wheeler, and S. P. DeWeerth, "Stimulus-artifact elimination in a multielectrode system," *IEEE Trans. Biomed. Circuits Syst.*, vol. 2, no. 1, pp. 10–21, Mar. 2008.
- [19] R. A. Blum, J. D. Ross, E. A. Brown, and S. P. DeWeerth, "An integrated system for simultaneous multichannel neuronal stimulation and recording," *IEEE Trans. Circuits Syst. I, Reg. Papers*, vol. 54, no. 12, pp. 2608–2618, Dec. 2007.
- [20] T. L. Hanson *et al.*, "High-side digitally current-controlled biphasic bipolar microstimulator," *IEEE Trans. Neural Syst. Rehabil. Eng.*, vol. 20, no. 3, pp. 331–340, May 2012.

- [21] M. Azin, H. J. Chiel, and P. Mohseni, "Comparisons of FIR and IIR implementations of a subtraction-based stimulus artifact rejection algorithm," in *Proc. 29th Annu. Int. IEEE Eng. Med. Biol. Conf.*, 2007, pp. 1437–1440.
- [22] K. Limnuson, H. Lu, H. J. Chiel, and P. Mohseni, "FPGA implementation of an IIR temporal filtering technique for real-time stimulus artifact rejection," in *Proc. IEEE Biomed. Circuits and Systems Conf.*, 2011, pp. 49–52.
- [23] J. S. Hunter, "The exponentially weighted moving average," *J. Qual. Technol.*, vol. 18, no. 4, pp. 203–210, Oct. 1986.
- [24] "Monitoring process variability using EWMA," in *Springer Handbook of Engineering Statistics*, H. Pham, Ed. New York, NY, USA: Springer, 2006, pp. 291–325.
- [25] S. W. Roberts, "Control chart tests based on geometric moving averages," *Technometrics*, vol. 1, no. 3, pp. 239–250, Aug. 1959.
- [26] J. F. Muth, "Optimal properties of exponentially weighted forecasts," *J. Amer. Stat. Assoc.*, vol. 55, pp. 299–306, 1960.
- [27] R. A. Freund, "Graphical process control," *Indus. Qual. Contr.*, vol. 18, pp. 15–22, 1962.
- [28] A. V. Oppenheim and R. W. Schafer, *Discrete-Time Signal Processing*. Upper Saddle River, NJ, USA: Prentice-Hall, 2010.
- [29] S. K. Mitra, *Digital Signal Processing: A Computer-Based Approach*. New York, NY, USA: McGraw-Hill, 2006.
- [30] M. Christensen and F. J. Taylor, "Fixed-point-IIR-filter challenges," *EDN Netw.*, vol. 51, no. 23, pp. 111–122, Nov. 2006.
- [31] B. Widrow and I. Kollar, *Quantization Noise: Round-Off Error in Digital Computation, Signal Processing, Control, and Communications*. New York, NY, USA: Cambridge Univ. Press, 2008.
- [32] P. P. Chu, *RTL Hardware Design Using VHDL: Coding for Efficiency, Portability, and Scalability*. Hoboken, NJ, USA: Wiley, 2006.



**Kanokwan Limnuson** (S'09) received the B.Eng. degree from Chulalongkorn University, Bangkok, Thailand, and the M.S. degree from Case Western Reserve University (CWRU), Cleveland, OH, USA, both in electrical engineering, in 2004 and 2008, respectively. Currently, she is working toward the Ph.D. degree in the BioMicroSystems Laboratory at CWRU. Her research interests are the development of neural signal-processing algorithms and their low-power implementation with analog and VLSI circuitry for bidirectional neural interfaces.



**Hui Lu** was born in 1981. She received the B.S. degree in biology from Nanjing University, Nanjing, China, in 2003.

Currently, she is working toward the Ph.D. degree in biology at Case Western Reserve University, Cleveland, OH, USA. Her research focuses on neural motor control and neuromodulation of the adaptive feeding behaviors in the marine mollusk *Aplysia californica*. She has authored seven peer-reviewed journal papers.



**Hillel J. Chiel** received the B.A. degree in English from Yale University, New Haven, CT, USA, and the Ph.D. degree in neural and endocrine regulation from the Massachusetts Institute of Technology (MIT), Cambridge, MA, USA.

After postdoctoral work at the Center for Neurobiology and Behavior at the College of Physicians and Surgeons, Columbia University, New York, NY, USA, and in the Department of Molecular Biophysics at AT&T Bell Laboratories, he joined the faculty of Case Western Reserve University, Cleveland, OH, USA. Currently, he is a Professor of Biology, with secondary appointments in the Departments of Neuroscience and Biomedical Engineering. His research focuses on the biomechanical and neural mechanisms of adaptive behavior, using the marine mollusk *Aplysia californica* as a model system. His research has led to the development of novel technology for imaging muscle movements and neural activity in intact animals, and biologically-inspired soft robots. He is a holder of four patents and has authored more than 115 peer-reviewed publications.

Dr. Chiel has been a Fellow of the Institute of Physics since 2004. He served as Guest Coeditor of a special issue on applied neurodynamics for the *Journal of Neural Engineering* with Dr. Peter Thomas in December 2011. He also serves on the editorial boards of the *Journal of Neural Engineering*, *Soft Robotics*, and the *Journal of Visualized Experiments*. In 2012, he won a prize from *Science*, published by the American Association for the Advancement of Science, for inquiry-based education.



**Pedram Mohseni** (S'94–M'05–SM'11) was born in 1974. He received the B.S. degree from the Sharif University of Technology, Tehran, Iran, in 1996, and the M.S. and Ph.D. degrees from the University of Michigan, Ann Arbor, MI, USA, all in electrical engineering, in 1999 and 2005, respectively.

Currently, he is a tenured Associate Professor in the Electrical Engineering and Computer Science Department at Case Western Reserve University, Cleveland, OH, USA, with a secondary appointment in the Biomedical Engineering Department. His research interests include analog/mixed-signal/RF integrated circuits and microsystems for neural engineering, wireless sensing/actuating systems for brain-machine interfaces, biomedical microtelemetry, and assembly/packaging of biomicrosystems.

Dr. Mohseni has been an Associate Editor for the *IEEE TRANSACTIONS ON CIRCUITS AND SYSTEMS-PART II* (2010–2012), *IEEE TRANSACTIONS ON BIOMEDICAL CIRCUITS AND SYSTEMS* (2008–present), and *IEEE TRANSACTIONS ON NEURAL SYSTEMS AND REHABILITATION ENGINEERING* (2012–present). In addition he was a Guest Editor for the *IEEE JOURNAL ON EMERGING AND SELECTED TOPICS IN CIRCUITS AND SYSTEMS* in 2011. He also serves on the Technical Program Committee of the IEEE CICC and RFIC Symposium. He was the recipient of the EECS Faculty Research Award for Exceptional Achievement in 2008, National Science Foundation Career Award in 2009, Case School of Engineering Research Award in 2011, and earned the first-place prize of the Medical Device Entrepreneur's Forum at the 58th annual conference of the ASAIO in 2012. He is a member of the IEEE Solid-State Circuits, Circuits and Systems, and Engineering in Medicine and Biology Societies.

# *A bidirectional neural interface SoC with an integrated spike recorder, microstimulator, and low-power processor for real-time stimulus artifact rejection*

**Kanokwan Limnuson, Hui Lu, Hillel  
J. Chiel & Pedram Mohseni**

**Analog Integrated Circuits and Signal  
Processing**  
An International Journal

ISSN 0925-1030  
Volume 82  
Number 2

Analog Integr Circ Sig Process (2015)  
82:457-470  
DOI 10.1007/s10470-015-0489-z

**ANALOG INTEGRATED CIRCUITS  
AND SIGNAL PROCESSING**  
**An International Journal**

Volume 82 • Number 2 • February 2015

**RFICs**

A 120 GHz QVCO with 16.2 GHz tuning range  
resistant against VCO pulling in 45 nm CMOS  
W. Volckaert · M. Steyaert · P. Reynaert **359**

A 2.5-GHz direct digital frequency synthesizer  
in 0.18  $\mu$ m CMOS  
Z. Jun-an · L. Guangjun · Z. Ruitao · L. Jiaoxue ·  
W. Yafeng · Y. Bo **369**

A 14.8 ps jitter low-power dual band all digital  
PLL with reconfigurable DCO and time-interlined  
multiplexers  
M. Souri · M.B. Ghaznavi-Ghoushchi **381**

**SIGMA DELTA MODULATORS**

A 95-dB DR second order incremental  $\Sigma\Delta$  ADC  
for multi-channel healthcare application  
X. Cao · Y. Wang · Z. Fu · T. Yi · Z. Hong **393**

A high-order closed-loop  $\Sigma\Delta$  interface for  
micro-machined accelerometer sensor  
H. Xu · X. Liu · Q. Fu · B. Lv **401**

**Coding efficiency and bandwidth enhancement  
in polar delta sigma modulator transmitter**  
N. Erfanmajd · H. Ghafoorfarad · A. Mohammadi **411**

**AMPLIFIERS AND FILTERS**

A variable-gain superregenerative amplifier  
controlled by duty-cycle for signal conditioning  
F. Rangel de Sousa · R.A. Romero Antayhua **423**

A new CMOS current-mode controllable-gain  
square rooting circuit using MOSFET in  
subthreshold  
E.S. Al-Suhailani · M.A. Al-Absi **431**

**TEST AND FAULT DIAGNOSIS**

A new test points selection method for analog  
fault dictionary techniques  
D. Zhao · Y. He **435**

Design and realization of a universal capacitive  
readout integrated circuit  
M. Liu · L. Xie · X. Jin **449**

(continued on back cover)

 SPRINGER

ISSN: 0925-1030

**Your article is protected by copyright and all rights are held exclusively by Springer Science +Business Media New York. This e-offprint is for personal use only and shall not be self-archived in electronic repositories. If you wish to self-archive your article, please use the accepted manuscript version for posting on your own website. You may further deposit the accepted manuscript version in any repository, provided it is only made publicly available 12 months after official publication or later and provided acknowledgement is given to the original source of publication and a link is inserted to the published article on Springer's website. The link must be accompanied by the following text: "The final publication is available at [link.springer.com](http://link.springer.com)".**

# A bidirectional neural interface SoC with an integrated spike recorder, microstimulator, and low-power processor for real-time stimulus artifact rejection

Kanokwan Limnuson · Hui Lu · Hillel J. Chiel ·  
 Pedram Mohseni

Received: 6 October 2014 / Revised: 20 December 2014 / Accepted: 6 January 2015 / Published online: 18 January 2015  
 © Springer Science+Business Media New York 2015

**Abstract** This paper presents a neural interface system-on-chip (SoC) featuring combined spike recording, electrical microstimulation, and real-time stimulus artifact rejection (SAR) for bidirectional interfacing with the nervous system. The SoC integrates a spike-recording front-end with input noise voltage of  $3.42 \mu\text{V}_{\text{rms}}$  (0.5 Hz–50 kHz), microstimulating back-end for delivering charge-balanced monophasic or asymmetric biphasic current pulses of  $<100 \mu\text{A}$  with passive discharge, and  $\mu\text{W}$ -level digital signal processing (DSP) unit for real-time SAR based on template subtraction. The DSP unit initializes its embedded 16b, 4 K static random-access memory with the first recorded stimulus artifact to reduce the operation time in generating an accurate artifact template signal for subtraction. Fabricated in AMS 0.35  $\mu\text{m}$  2P/4M CMOS, the  $3.1 \times 3.1\text{-mm}^2$  SoC has been characterized in benchtop tests and neurobiological experiments with isolated buccal ganglia of an *Aplysia californica* (a marine mollusk). The SoC can successfully remove mV-range stimulus artifacts with duration up to  $\sim 115$  ms from the contaminated neural data in real time and recover  $\mu\text{V}$ -range extracellular neural spikes that occur on the tail end of the artifacts. The average root-

mean-square (rms) value of the pre-processed stimulus artifact is reduced by a factor of  $\sim 24$ –30 post-processing, with DSP unit power consumption of  $<25 \mu\text{W}$  from 1.5 V.

**Keywords** Closed-loop neuroprostheses · Neural recording · Neural signal processing · Neurostimulation · Stimulus artifact rejection · System-on-chip · Template subtraction

## 1 Introduction

Stimulus artifact rejection (SAR) is an integral feature of the next-generation, bidirectional, neural interface microsystems that aim to combine electrical stimulation and neuroelectrical recording in a single device. Large stimulus artifacts often mask the neural activity-of-interest, either preventing the analysis of stimulus-evoked recorded data [1], or limiting the efficacy of activity-dependent stimulation in closed-loop operation [2, 3].

Blanking techniques in which the recording amplifier input is disconnected during stimulation have traditionally been effective in rejecting large, saturating stimulus artifacts at the expense of no viable recording during stimulation [4–9]. Using active feedback circuitry to provide a low-impedance discharge path for the stimulating electrode [10, 11], and careful stimulator design related to the isolation of stimulation channels and parasitic current injection [12] have been shown to decrease the duration and amplitude of the artifacts. However, these approaches cannot fully eliminate them, often leaving behind considerable residual artifacts.

On the other hand, more complex subtraction techniques typically employ digital signal processing (DSP) algorithms to generate a high-fidelity template signal representative of

K. Limnuson · P. Mohseni (✉)  
 Electrical Engineering and Computer Science Department, Case Western Reserve University, Cleveland, OH 44106, USA  
 e-mail: pedram.mohseni@case.edu

H. Lu · H. J. Chiel  
 Department of Biology, Case Western Reserve University, Cleveland, OH 44106, USA  
 e-mail: hjc@case.edu

P. Mohseni  
 Advanced Platform Technology (APT) Center – A Veterans Affairs (VA) Research Center of Excellence, Cleveland, OH 44106, USA

the stimulus artifacts for subsequent subtraction from the contaminated neural data, resulting in artifact removal [13–15]. This is based on the premise that the overall shape, dynamic range, and timing of the stimulus artifacts do not significantly vary over consecutive stimulation cycles. Hence, subtraction techniques have to rely on full-scale recording of the stationary stimulus artifacts for accurate template signal generation, but offer the advantage of retaining signal information during stimulation.

Since subtraction techniques require DSP algorithms for template signal generation, they have traditionally been implemented offline on a home-base computer post-data acquisition. To execute a subtraction-based SAR algorithm in real time (i.e., as the recording is taking place), a suitable template-generation technique should be realized in hardware after optimization and validated using real neural data. To that end, Wichmann and Devergnas have recently reported an artifact-removal device based on template subtraction, which employs commercial off-the-shelf (COTS) components such as a microcontroller as well as analog-to-digital and digital-to-analog converters [16]. The device employs digital averaging of the recurrent, stationary artifact waveforms [15] in order to generate and update a template signal that is subtracted from the contaminated data record on subsequent occurrences of the artifact.

We have previously assessed the feasibility of hardware implementation of a similar subtraction-based SAR algorithm using the well-established infinite impulse response (IIR) temporal filtering technique for template generation [17], and successfully realized a hardware-optimized, IIR-SAR algorithm on a field-programmable gate array (FPGA) platform [18]. In this paper, we present very-large-scale integrated (VLSI) implementation of the optimized IIR-SAR algorithm using a custom, low-power DSP architecture, which is co-integrated with recording and micro-stimulating circuitry to create a standalone, proof-of-concept, prototype system-on-chip (SoC) featuring low-noise neural recording, programmable neurostimulation, and real-time stimulus artifact removal for bidirectional interfacing with the nervous system [19]. The SoC functionality is validated in neurobiological experiments with isolated buccal ganglia of an *Aplysia californica* (a marine mollusk), an experimentally tractable and well-studied invertebrate model system for stable, repeatable tests.

The paper is organized as follows. Section 2 briefly describes the IIR-SAR algorithm. Section 3 presents the system architecture of the SoC and Sect. 4 presents the integrated circuit architecture of the recording, micro-stimulating, and signal-processing blocks within the SoC. Section 5 presents our measured results from the SoC, and Sect. 6 finally draws some conclusions from this work.

## 2 IIR implementation of SAR algorithm

In this section, we briefly describe the template subtraction-based, IIR-SAR algorithm that was previously developed in MATLAB™ simulations [17] and optimized for hardware implementation [18]. Template signal generation is achieved by averaging a number of the properly shifted versions of the input neural data, which also contain the stimulus artifacts. This can be mathematically expressed as:

$$y(t) = \sum_{n=0}^{N-1} a(n) \cdot x(t - nT_{sti}), \quad (1)$$

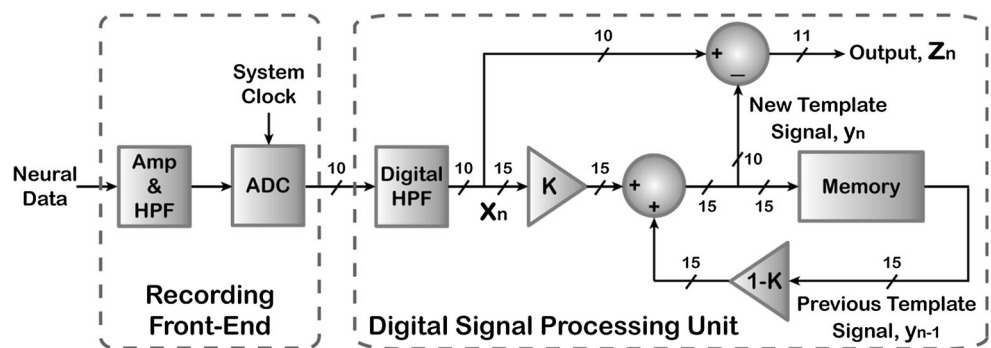
where  $y(t)$  is the estimated template signal,  $x(t)$  is the input neural data,  $N$  is the number of stimulus artifact waveforms used for averaging (i.e., averaging depth),  $a(n)$  are the averaging factors, and  $T_{sti}$  is the stimulation period. In order for the artifact and its template to have equal amplitudes, the averaging factors should sum up to unity and can be all equal to  $1/N$  for common averaging.

Figure 1 depicts the architecture for IIR implementation of the SAR algorithm, depicting the number of bits for the internal nodes after considering dynamic range and fraction length requirements for optimum performance with a 10b recording front-end [18]. To generate a template signal representative of the stimulus artifacts, temporal filtering is employed in the form of an exponentially weighted moving average, (EWMA) [20], of several properly shifted versions of the input neural data containing the stimulus artifacts. This can be represented by:

$$y_n = (1 - K) \cdot y_{n-1} + K \cdot x_n, \quad (2)$$

where  $y_n$  is the new artifact template signal,  $y_{n-1}$  is the previous template signal, and  $x_n$  is the input neural data. Hence, the template signal is retained in a memory, and a new template signal is generated from the previous template signal and the input neural data according to (2), which is then subtracted from the input neural data. Factor  $K$  ( $<1$ ) plays a similar role as  $N$  in (1) and affects the IIR system response time and accuracy. Specifically, increasing the averaging depth avoids significant presence of neural noise (i.e., residual neural activity) in the stimulus artifact template signal that can otherwise lead to undesired attenuation of the neural activity at the output upon template subtraction. This is obviously achieved at the expense of longer response time for the IIR-SAR system in creating an accurate artifact template signal [17]. Furthermore, if  $|1 - K| < 1$ , the 1st-order IIR system in (2) that has a single pole at  $(1-K)$  would be stable [21]. Factor  $K$  can be selected as  $1/2^i$  (with  $i$  being an integer) to alleviate the use of multipliers in VLSI implementation.

**Fig. 1** IIR architecture of the template subtraction-based SAR algorithm



### 3 SoC architecture

Figure 2 shows the system architecture of the proof-of-concept, bidirectional neural interface SoC that comprises a spike-recording front-end and programmable microstimulator, as well as an embedded DSP unit for real-time SAR. The SoC operates from 1.5 V, except for the stimulating electrode driver stage in which 5 V is used for enhanced voltage compliance.

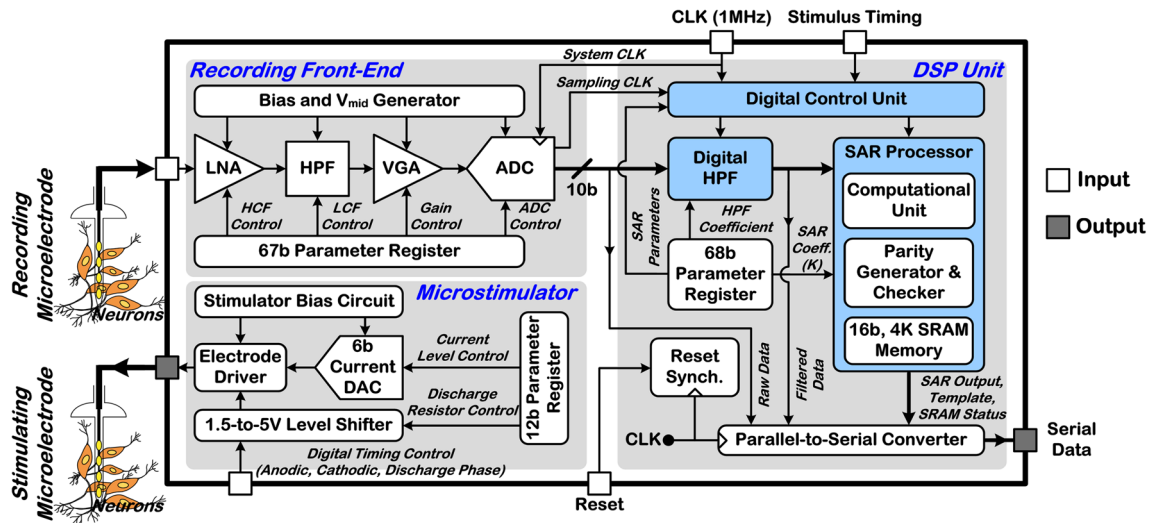
The recording front-end performs ac amplification, dc baseline stabilization, highpass filtering, and 10b digitization of the neural data with digitally programmable gain and bandwidth. The microstimulator delivers trains of charge-balanced monophasic or asymmetric biphasic current pulses followed by passive discharge, with digitally programmable current pulse amplitude and externally controllable current pulse duration, frequency, and number within a stimulus train, as well as polarity of the leading phase. The DSP unit performs additional highpass filtering digitally to remove any residual dc offset or low-frequency noise, and performs real-time stimulus artifact removal

based on template subtraction, as previously described in Sect. 2. The next section presents each SoC building block in further detail.

### 4 Integrated circuit architecture

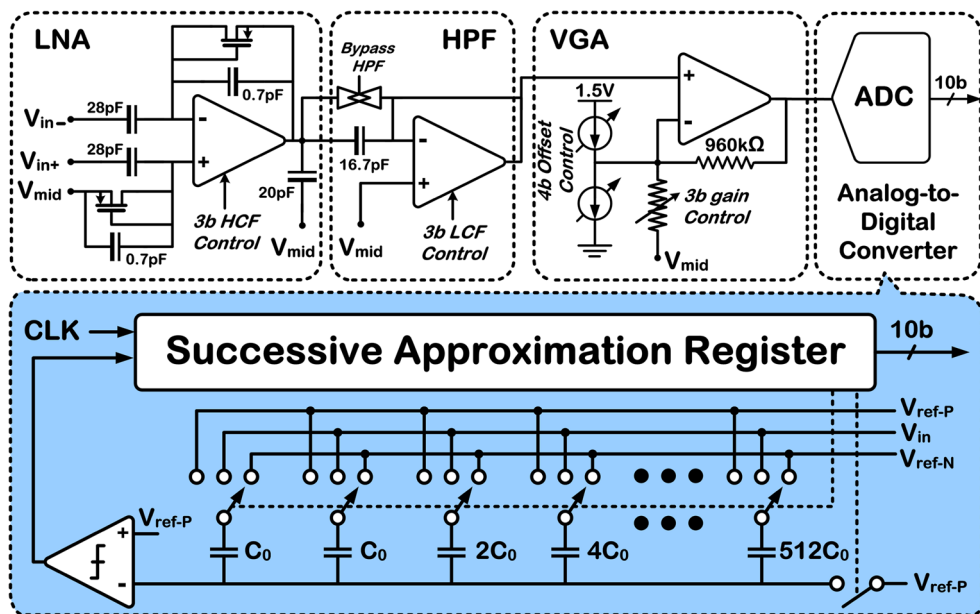
#### 4.1 Recording front-end

Figure 3 depicts the circuit schematic of the spike-recording front-end, comprising a low-noise amplifier (LNA) with adjustable high cutoff frequency (HCF),  $G_m$ -C highpass filter (HPF) with adjustable low cutoff frequency (LCF), variable-gain amplifier (VGA) with adjustable offset, and 10b successive-approximation register analog-to-digital converter (ADC) [3]. It features an overall bandpass frequency response with eight different gain values in 49–65.6 dB at 1 kHz, with the LNA providing fixed 32 dB of ac gain via capacitive feedback and dc baseline stabilization via a MOS-bipolar pseudo-resistor in parallel with the feedback capacitor [22]. With the ac gain nominally set



**Fig. 2** System architecture of the bidirectional neural interface SoC with real-time SAR capability

**Fig. 3** Circuit schematic of the spike-recording front-end



to 60 dB, the bandwidth can be programmed from <0.1 Hz–12.3 kHz to 390 Hz–6.4 kHz by digitally tuning the  $G_m$ –C HPF and LNA bias currents.

The 10b successive-approximation register ADC, whose capacitive network is driven by the preceding VGA, is nominally clocked at 1 MHz. Each ADC conversion cycle takes 28 clock cycles in which 16 cycles are dedicated to sampling, 1 cycle to hold, 10 cycles to approximation, and 1 cycle to reset; thus providing a sampling frequency of 35.7 kSa/s that is adequate for recording single-unit neural spikes with frequency content up to 10 kHz. The extended sampling period helps relax current drive requirements of the preceding VGA for low-power operation.

#### 4.2 Microstimulator

Figure 4(a) shows the circuit schematic of the 6b current-based digital-to-analog converter (DAC) and electrode driver stage of the electrical microstimulator. The electrode driver operates from 5 V and integrates a pair of pMOS (anodic) and nMOS (cathodic) current sources with thick-oxide transistors and boosted output impedance (>100 M $\Omega$ ) via negative feedback, provided by two op-amps,  $A_{1,2}$ , for constant-current stimulation [3]. The DAC operates from 1.5 V and outputs a programmable current in 0–2.2  $\mu$ A with 6b resolution that is then amplified to generate a maximum current of ~100  $\mu$ A, which is adequate for a variety of applications in both the intracortical [2, 23] and intraspinal microstimulation [24, 25] paradigms. The DAC also employs a 4b current-adjust mechanism to fine tune the desired output stimulus current in the

presence of process and voltage (PV) variations. Additional circuitry is used in the electrode driver to control the gate voltage of transistor  $M_3$  in the nMOS current source and limit the drain-source voltage across  $M_{2,3}$  to ~V<sub>DD</sub>/2 (i.e., ~2.5 V) for avoiding hot-carrier effects when the stimulus site voltage is near the supply rail [26].

The microstimulator can be programmed to generate two different types of stimulus current pulses. In one case shown in Fig. 4(b), a monophasic stimulus can be generated with a constant-current phase duration of  $T_A$  and 6b-programmable amplitude of  $I_A$ , which is followed by a passive discharge phase to drain the accumulated charge on the stimulation site using a 2b-programmable resistor combination in the range of 4.6 to 32 k $\Omega$ . In another case shown in Fig. 4(c), an asymmetric biphasic stimulus can also be generated in which the cathodic-phase current is set to be 1/3 of that in the anodic phase via proper transistor sizing ratios for optimal use of the available voltage headroom (5 V). For the current pulse waveform in Fig. 4(c) to be theoretically charge-balanced,  $T_C$  should nominally be set equal to 3  $\times$   $T_A$ . In practice, however, the ratio of current levels in the anodic and cathodic phases can deviate from 1/3 due to PV variations and transistor mismatches. Hence, passive discharge is also performed after each stimulus cycle to drain any residual charge left from charge mismatch between the anodic and cathodic phases [27–29]. Furthermore, in this proof-of-concept SoC with limited number of stimulus channels, an external dc-blocking capacitor can also be placed in series with the electrode-tissue interface to prevent any net dc current flow into the tissue arising from charge imbalance or semiconductor failure.

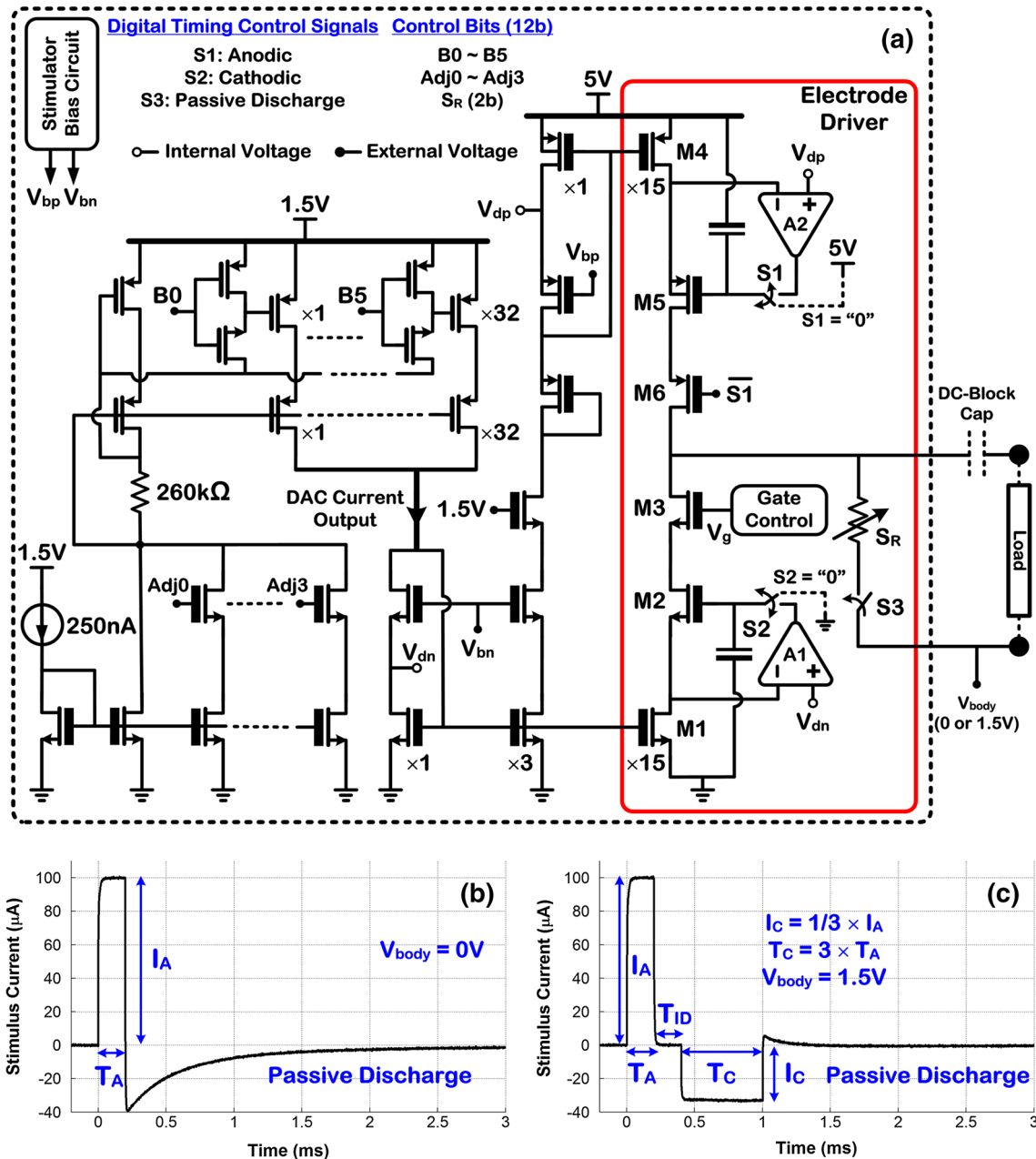


**Fig. 4** *Top*—**a** circuit schematic of the microstimulator. *Bottom*—measured **b** monophasic and **c** asymmetric biphasic stimulus current waveforms delivered by the microstimulator to saline via a silicon-substrate, “Michigan” electrode

#### 4.3 DSP unit

The major building blocks of the DSP unit include a digital HPF, digital control unit, and a SAR processor, which in turn comprises a computational unit, 16b static random-access memory (SRAM), and parity generator/checker to identify potential memory errors. A reset synchronizer generates an internal signal, *Sync Reset*, to asynchronously reset the DSP unit when the signal is low [30]. A 68b register is used to store user-set parameters such as

bandwidth setting of the digital HPF and SAR coefficient,  $K$ , as well as memory-initialization, memory-length, and output-blanking settings. The requisite memory length (i.e., # of 16b samples) depends on the sampling frequency and time duration over which the SAR algorithm operates, which should be at least equal to the stimulus artifact duration for proper operation. With a nominal sampling frequency of 35.7 kSa/s in the recording front-end and SRAM size of 4 K in the DSP unit, the SoC can process stimulus artifacts up to  $\sim 115$  ms in duration. A smaller

memory can always be used for a lower sampling frequency in the recording front-end or shorter artifacts.

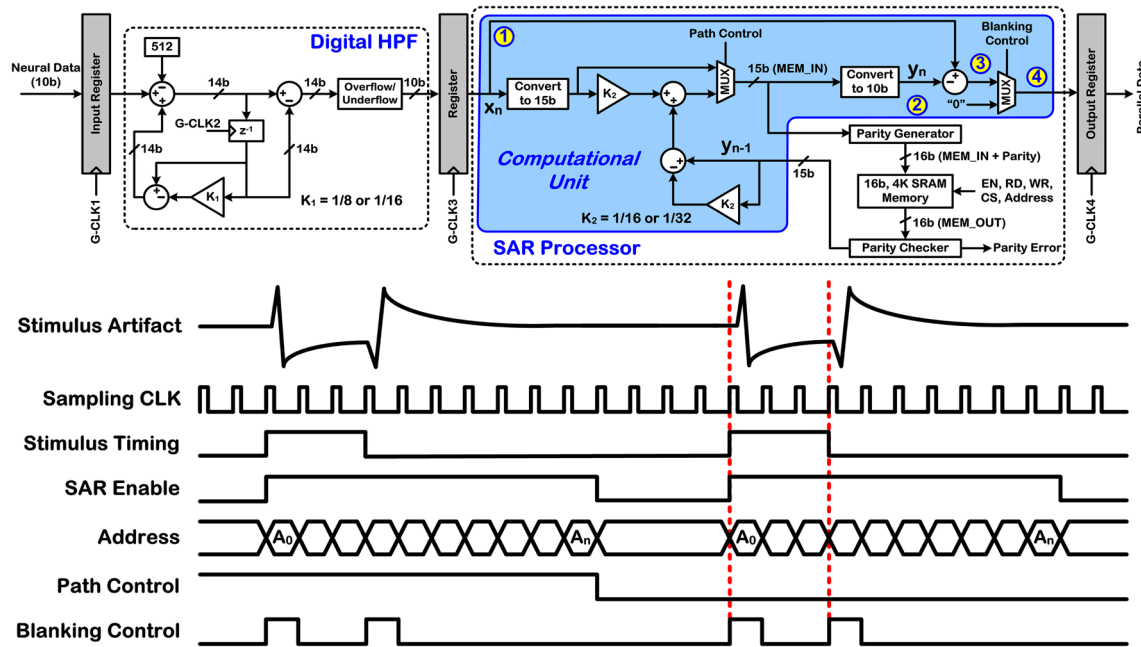
Figure 5 depicts the structure of the digital HPF and SAR processor in the DSP unit. The digitized neural sample (10b) from the ADC is first highpass filtered using a 1st-order filter with direct form II architecture and adjustable LCF. Factor  $K_1$  is set as 1/16 or 1/8, resulting in LCF of 366 or 756 Hz, respectively, with a system clock of 1 MHz. An overflow/underflow detector at the HPF output limits its dynamic range to 10b before feeding the SAR processor.

The SAR processor only operates for the duration of each stimulus artifact and uses fixed-point computation for simplicity, with 15b representation at its internal nodes to mitigate quantization noise effects on template signal accuracy [18]. The digitized/filtered sample at the HPF output (10b) is first converted to 15b and then multiplied by factor  $K_2$  (same as  $K$  in (2), 1/16 or 1/32 in this work) stored in the 68b parameter register. Next, the memory data containing the previous template signal are read, multiplied by  $(1-K_2)$ , and added to  $(K_2 \cdot x_n)$  to obtain the new template signal (15b), which is written back into the 16b memory for the next cycle after an even-parity bit addition. The new template signal is also converted back to 10b and subsequently subtracted from the 10b digitized/filtered input sample to produce the SAR output signal. Outside the duration of the artifact, the SAR processor is disabled, and the sample at the HPF output is directly routed to the output register. The three registers in Fig. 5 hold the data for

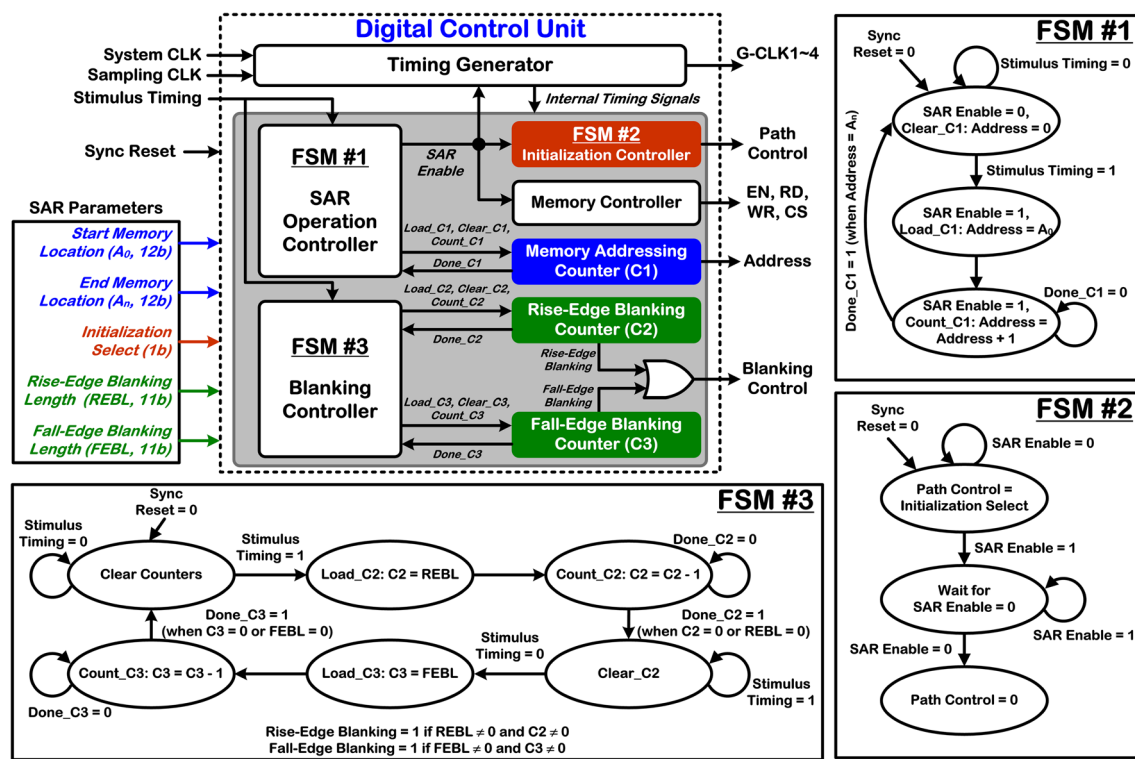
processing in each stage with proper timing control. Instead of sharing the same global clock signal and using a local enable signal to synchronize the registers [18], clock gating is used for low power consumption.

Figure 5 also depicts the DSP unit's timing operation for two consecutive stimulus artifacts assumed to be the very first and second artifacts. Using the *Path Control* signal generated by the initialization controller of the digital control unit, the computational unit of the SAR processor (SAR-CU) initializes the memory with the very first recorded stimulus artifact, which is shown to significantly decrease the response time of the IIR-SAR algorithm in generating an accurate template signal, especially when artifacts are highly reproducible in consecutive stimulation cycles [31]. Further, using the *Blanking Control* signal from the digital control unit, SAR-CU removes any residual artifacts in the output after template subtraction, especially at the rising and falling edges of the artifact where it rapidly changes with time.

Figure 6 depicts the architecture of the digital controller of the DSP unit, comprising a timing generator and several finite-state machine (FSM) controllers to manage the SAR processor operation, memory operation and its initialization, as well as output blanking. The timing generator creates all internal timing signals for the digital control unit, as well as the gated clocks for the digital HPF and the three registers in Fig. 5. The SAR operation controller and its associated counter (C1) respectively generate the internal *SAR Enable* signal and the *Address* signal to access



**Fig. 5** Architecture of the digital HPF and SAR processor of the DSP unit along with illustration of the DSP unit's timing operation for two consecutive artifacts



**Fig. 6** Architecture of the digital controller of the DSP unit along with its three finite-state machines (FSMs)

the memory between the start ( $A_0$ ) and end ( $A_n$ ) locations. Specifically, the SAR operation controller detects the rising edge of the *Stimulus Timing* signal upon which *SAR Enable* is activated and counter C1 is loaded with  $A_0$  (12b). Next, it commands the counter to up-count from  $A_0$  until the end memory location,  $A_n$  (12b), is reached upon which *SAR Enable* is deactivated until the next rising edge of the *Stimulus Timing* signal arrives. Hence, the time duration over which the SAR processor operates (i.e., when *SAR Enable* is high) is programmable via the user-set memory-length setting, and should be ideally equal to the stimulus artifact duration (and not much longer) to save processing power. The SAR processor is disabled when *SAR Enable* is low (i.e., outside the stimulus artifact duration).

The blanking controller and its two associated counters (C2 and C3) generate the *Blanking Control* signal. Specifically, the blanking controller detects the rising edge of the *Stimulus Timing* signal upon which counter C2 is loaded with the *Rise-Edge Blanking Length (REBL)* parameter (11b). Next, counter C2 activates the *Rise-Edge Blanking* signal and starts to down-count from *REBL* until the counter value reaches zero upon which *Rise-Edge Blanking* is deactivated. Upon detecting the falling edge of the *Stimulus Timing* signal, the same process is repeated by the blanking controller and counter C3 to generate *Fall-Edge Blanking* using the *Fall-Edge Blanking Length (FEBL)* parameter (11b). By defining *Blanking Control* as the OR

function of the two internal timing signals, the user can independently set the blanking duration from 0 (no blanking) to 2,047 data points (~57 ms given the nominal sampling frequency), synchronized with the rising and falling edges of the *Stimulus Timing* signal (see Fig. 5).

## 5 Measurement results

A prototype chip was fabricated in AMS 0.35  $\mu\text{m}$  2P/4M standard CMOS, measuring  $\sim 3.1 \times 3.1 \text{ mm}^2$  including the bonding pads. This section presents the measurement results from electrical benchtop characterization and neurobiological experiments in isolated buccal ganglia of an *Aplysia californica*.

### 5.1 Benchtop characterization

The top plots in Fig. 7 depict the measured frequency response and input noise voltage spectrum of the analog recording front-end for three different bandwidth settings and with the mid-band ac gain nominally set to 60 dB. The LCF was programmable from <0.1 to 390 Hz, whereas the HCF was adjustable in the range of 6.4–12.3 kHz. In the right plot, note how the  $G_m$ –C HPF effectively removed the flicker noise contribution, when the LCF was digitally set to 260 and 390 Hz (the HPF was bypassed for the case

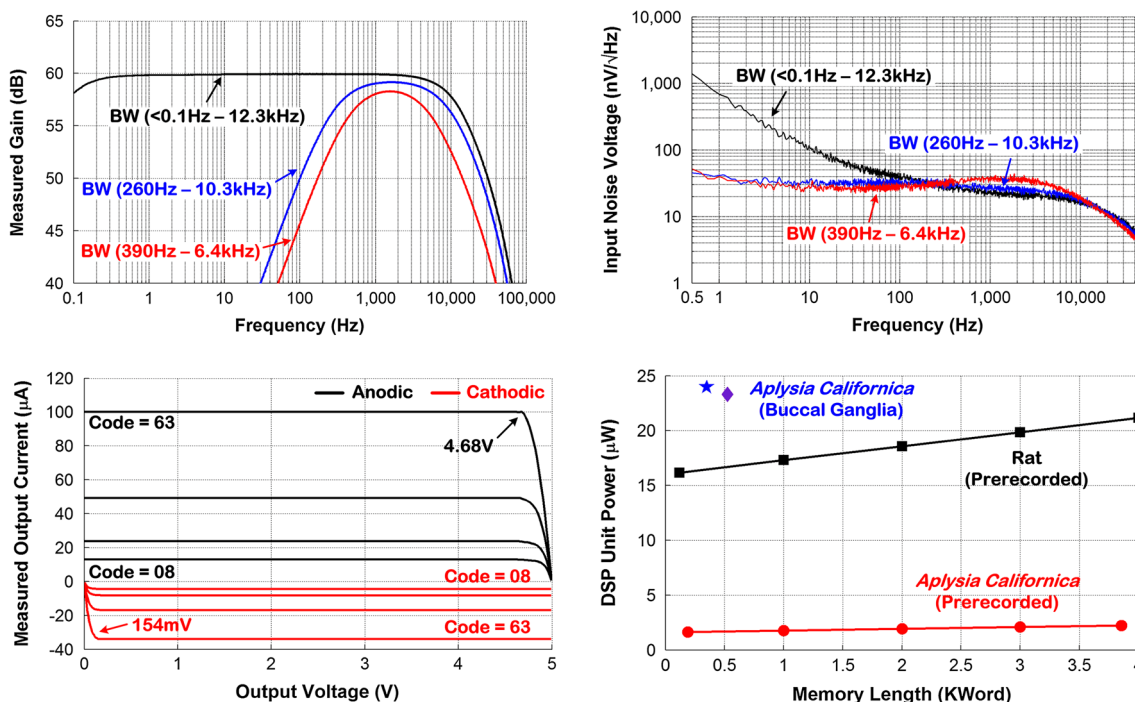


**Fig. 7** Top—measured gain (left) and input noise voltage (right) of the analog recording front-end. Bottom—measured microstimulator output current versus output voltage in anodic and cathodic phases

of the recording bandwidth of <0.1 Hz–12.3 kHz.) With the bandwidth of the analog recording front-end set to 390 Hz–6.4 kHz, the input noise voltage measured in 0.5 Hz–50 kHz was 3.42  $\mu\text{V}_{\text{rms}}$ , resulting in noise efficiency factor (NEF) of 2.74 for the LNA.

The bottom left plot depicts the measured microstimulator output current versus its output voltage for four different DAC input codes when sourcing and sinking current in anodic and cathodic phases, respectively. The microstimulator output voltage could reach at least 4.68 V (going toward 5 V) and 154 mV (going toward 0 V) when sourcing and sinking current, respectively, from 5 V. The output impedance was measured to be  $>100 \text{ M}\Omega$  (limited by the precision of our measurement setup), sufficiently high for constant-current stimulation.

To evaluate the DSP unit power consumption, two *prerecorded* neural datasets from a rat (sampled at  $\sim 24.41$  kHz and recorded during 4-Hz cortical stimulation) and an *Aplysia californica* (sampled at 2 kHz and recorded during 0.5-Hz stimulation) were used. These datasets were collected as part of experiments that were unrelated to this work and provided to us by two different research laboratories.

The system clock frequency was set to  $\sim 684$  and 56 kHz for the rat and *Aplysia* datasets, respectively (i.e.,  $28 \times$  their sampling frequency). The bottom right plot in Fig. 7 shows the measured DSP unit power consumption

(left) and DSP unit power consumption versus requisite memory length for processing neural datasets from a rat and *Aplysia californica* (right)

versus requisite memory length, when processing each neural dataset for artifact removal. The measured power was in the range of 1.6–2.2  $\mu\text{W}$  for the *Aplysia* neural dataset and increased to 16.1–21.2  $\mu\text{W}$  for the rat neural dataset due to the higher system clock frequency. Within each dataset, the measured power also increased with the duration of the *SAR Enable* signal. Table 1 summarizes the measured SoC performance.

## 5.2 Neurobiological experiments

The SoC functionality was next verified in neurobiological experiments with isolated buccal ganglia of an *Aplysia californica* [32]. Custom-made hook electrodes were made from enamel-coated stainless steel wire (Catalogue # 100194, *California Fine Wire*, 1-mil diameter) as previously described in [33], and used for stimulating on branch A of buccal nerve 2 (BN2-A) and recording from either the buccal nerve 2 (BN2) or buccal nerve 3 (BN3). The de-insulated region of the curled hook was placed in direct contact with the nerves, anchored in place with superglue, and electrically insulated from the fluid medium using Kwik-Sil, whereas the de-insulated tip of the reference electrode was left exposed to the fluid medium [33]. For recording purposes, these were connected to the inverting ( $V_{\text{in}-}$ ) and non-inverting ( $V_{\text{in}+}$ ) inputs of the LNA, respectively (see Fig. 3). Furthermore,  $V_{\text{in}+}$  was also connected to the SoC ground connection.

**Table 1** Summary of measured SoC performance

RECORDING FRONT-END		MICROSTIMULATOR		
Max. BW	<0.1Hz – 12.3kHz (HPF bypassed)	Stimulus Waveform	Anodic	Cathodic
Min. BW	390Hz – 6.4kHz		Asymmetric biphasic & monophasic w/ passive discharge	
AC Gain @ 1kHz	49 – 65.6dB	Max. $I_{OUT}$	100 $\mu$ A	34 $\mu$ A
RMS Input Noise (0.5Hz – 50kHz)	3.01 $\mu$ V (Max. BW) 3.42 $\mu$ V (Min. BW)		DAC Linearity	< $\pm$ 1.9 LSB
NEF	2.48 (Max. BW) 2.74 (Min. BW)	Voltage Compliance (Max. $I_{OUT}$ )	4.68V (of 5V)	4.846V (of 5V)
CMRR @ 1kHz	57.1dB		DIGITAL SIGNAL PROCESSING UNIT ( $f_{CLK} = 1\text{MHz}$ )	
PSRR @ 1kHz	63.7dB	HPF LCF	366Hz ( $K_1 = 1/16$ ); 756Hz ( $K_1 = 1/8$ )	
INL/DNL	< $\pm$ 1.2 LSB		Stimulus Artifact Duration	<114.7ms
ENOB	9b ( $f_s = 35.7\text{kSa/s}$ )	Blanking Duration	<57.3ms	
Power Consumption (Incl. ADC)	31.5 $\mu$ W (Max. BW; $f_{CLK} = 1\text{MHz}$ ) 26.7 $\mu$ W (Min. BW; $f_{CLK} = 1\text{MHz}$ )		SAR Coefficient ( $K_2$ )	1/16, 1/32
		Power Consumption	<25 $\mu$ W	
<b>Total Power Consumption w/o Microstimulator (Min. BW; <math>f_{CLK} = 1\text{MHz}</math>) = &lt;51.7<math>\mu</math>W</b>				

The bandwidth of the analog recording front-end was nominally set to the minimum range. In the DSP unit, factors  $K_1$  and  $K_2$  were both set to 1/16, and memory initialization was enabled. Furthermore, the DSP unit was set to operate for the duration of the stimulus artifact only, which was determined a priori, to save processing power. As shown in Fig. 8, an external stimulator was used for these tests, since the current range of the on-chip microstimulator ( $\leq 100 \mu\text{A}$ ) was not enough for effective stimulation on BN2-A. A home-base computer was used for generating the *Stimulus Timing* signal, which was applied to both the external stimulator and the SoC, as well as for storing the serial output data from the SoC.

### 5.2.1 Case #1

In the first case, recording was performed from BN2, with the gain of the analog recording front-end nominally set to the minimum value to determine the largest stimulus artifact dynamic range that could be handled by the SAR processor. Stimulation was performed for 1 min at 2 Hz with a stimulus current pulse of 100  $\mu\text{A}$  in amplitude and 1 ms in pulse-width. The SAR processor was set to operate for 15 ms upon receiving an indication of stimulation by the *Stimulus Timing* signal, and output blanking was applied for 0.5 ms in synchrony with the rising and falling edges of the *Stimulus Timing* signal. Figure 9 depicts the measured results in which plot numbers correspond to the node numbers in SAR-CU of Fig. 5. Specifically, plot #1 shows a 15-ms window of the input data to the SAR-CU, showing a total of 119 high-pass-filtered stimulus artifacts superimposed. Plot #2 depicts the 119 artifact templates generated by the DSP unit and

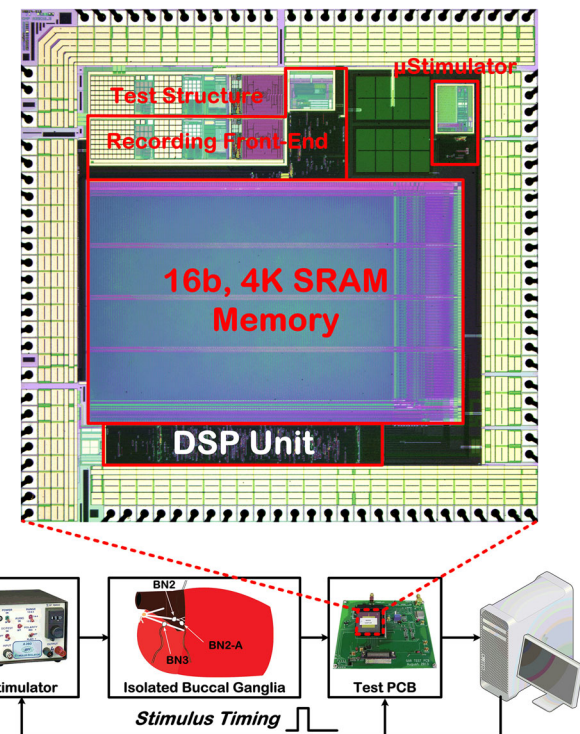
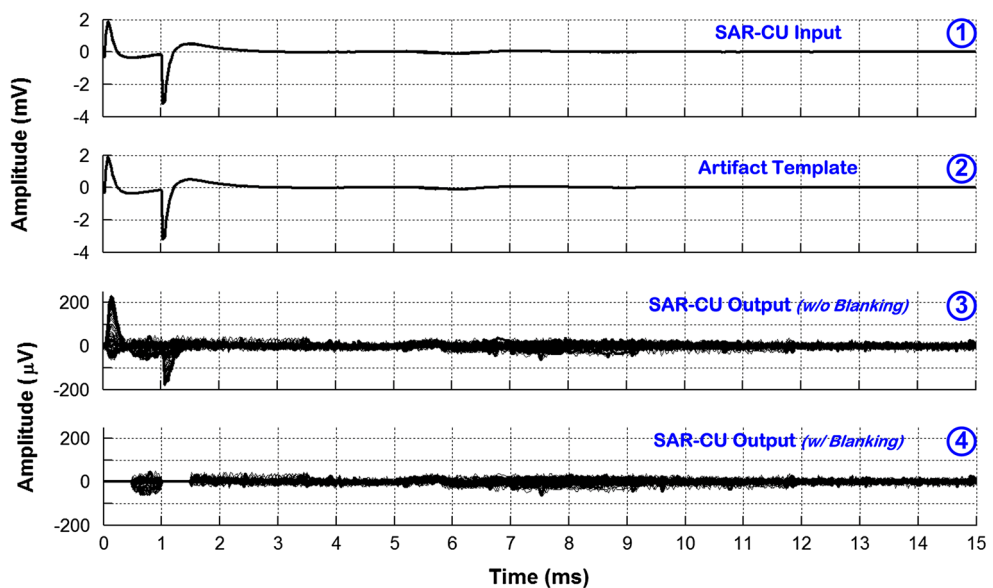


**Fig. 8** Illustration of the experimental setup for the neurobiological tests

superimposed. Plot #3 shows the SAR-CU output signal without blanking, showing significant rejection of the stimulus artifacts after template subtraction, whereas plot #4 shows the SAR-CU output signal after template subtraction and residual blanking. This experiment demonstrated the SAR processor functionality in fully removing artifacts as

**Fig. 9** Measured results from case #1 in neurobiological experiments



large as  $\sim 5 \text{ mV}_{\text{pp}}$  from the recorded data in real time, although no neural spikes could be detected due to subthreshold stimulation at  $100 \mu\text{A}$  and the small gain of the analog recording front-end. The DSP unit power consumption was measured to be  $23.3 \mu\text{W}$  (see Fig. 7).

### 5.2.2 Case #2

In the second case, recording was performed from BN3, with the gain of the analog recording front-end nominally set to the maximum value to enable neural spike recording. Memory initialization with the first recorded artifact was performed using a single current pulse at  $100 \mu\text{A}$  for subthreshold stimulation to avoid the presence of stimulus-evoked neural spikes on the initial condition of the memory. This was then followed by  $400\text{-}\mu\text{A}$ , 2-Hz stimulation for 1 min, with the stimulus current pulselwidth always set to 1 ms. The SAR processor was set to operate for 10 ms upon receiving an indication of stimulation by the *Stimulus Timing* signal, and output blanking was applied for 2.5 ms in synchrony with the rising edge of *Stimulus Timing*.

Since memory initialization was performed based on subthreshold stimulation, the initial condition of the memory normalized to the steady-state artifact template signal was  $<1$ . Hence, prior to any further data analysis, we first determined the minimum number of stimulus artifacts required to generate an accurate template signal [18]. The template error was defined as:

$$\text{Error}(\%) = \left| \frac{v_{\text{rms},\text{SA}} - v_{\text{rms},\text{template}}}{v_{\text{rms},\text{SA}}} \right| \times 100, \quad (3)$$

where  $V_{\text{rms},\text{SA}}$  and  $V_{\text{rms},\text{template}}$  are the root-mean-square (rms) values of the highpass-filtered stimulus artifact and

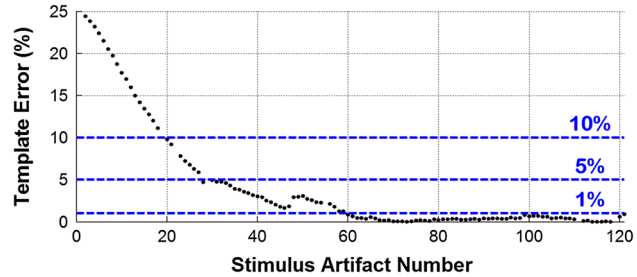


**Fig. 10** Error in template generation versus number of stimulus artifacts

corresponding template signal, respectively, within the 10-ms duration of SAR processor operation. Figure 10 shows the template error plot that was calculated for each stimulus artifact within the 1-min stimulation duration, except for the very first artifact and those with neural spikes present on their tail ends. As expected, the template error decreased with the number of artifacts, requiring 20 and 60 artifacts to reach 10 and 1 % error, respectively.

Figure 11 depicts the measured results from case #2 in neurobiological experiments after the template error reached 1 %. Specifically, plot #1 shows a 10-ms window of the input data to the SAR-CU, showing a total of 62 highpass-filtered stimulus artifacts superimposed (artifact #60–121), with some (barely visible) neural spikes riding on their tail ends. Plot #2 depicts the 62 stimulus artifact templates generated by the DSP unit and superimposed. Plot #3 shows the SAR-CU output signal without blanking, showing significant rejection of the stimulus artifacts after template subtraction, whereas plot #4 shows the SAR-CU output signal with blanking in which the neural spikes were recovered in real time (see arrows) after template

**Fig. 11** Measured results from case #2 in neurobiological experiments. Plot #4 is shown after additional offline lowpass filtering in dc–2 kHz. Note the smaller dynamic range of the Y-axis in the bottom plot after artifact removal and residual blanking

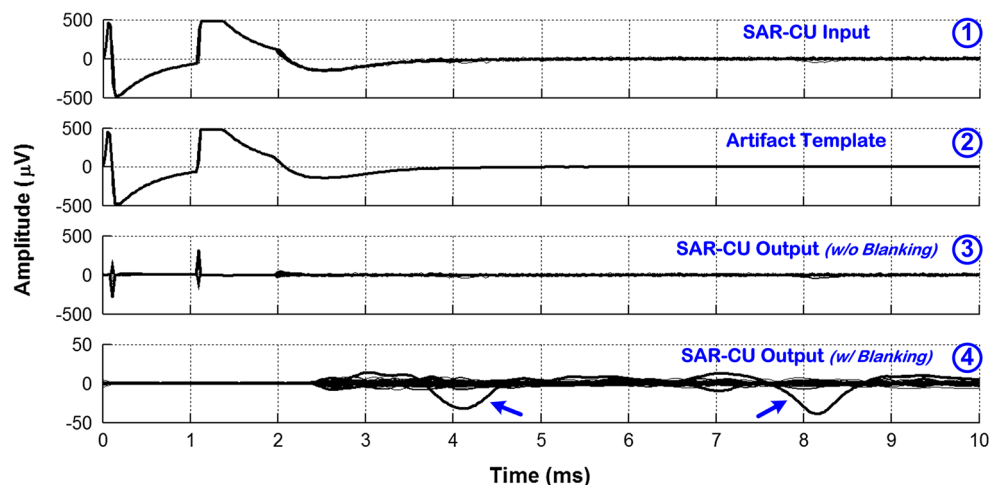


**Table 2** Statistics of pre- and post-processed stimulus artifacts

Template error		Mean ( $\mu\text{V}_{\text{rms}}$ )	SD ( $\mu\text{V}_{\text{rms}}$ )
<b>Case #1</b>			
$\leq 6\%$ (119 of 120 SAs)	Pre-processing	285.6	4.7
	Post-processing (w/o blanking)	13.2	5.9
	Post-processing (w/blanking)	9.6	1.6
	Output noise	7.1	0.2
<b>Case #2</b>			
$\leq 10\%$ (97 of 121 SAs)	Pre-processing	143.1	0.7
	Post-processing (w/o blanking)	11.5	3.9
	Post-processing (w/blanking)	6.2	0.7
$\leq 5\%$ (90 of 121 SAs)	Pre-processing	143.1	0.7
	Post-processing (w/o blanking)	10.9	3.2
	Post-processing (w/blanking)	6.1	0.6
$\leq 1\%$ (60 of 121 SAs)	Pre-processing	142.9	0.4
	Post-processing (w/o blanking)	10.6	3.2
	Post-processing (w/blanking)	6.0	0.5
	Output noise	7.2	0.6

subtraction and residual blanking. The DSP unit power consumption was measured to be  $\sim 24 \mu\text{W}$  (see Fig. 7).

In order to assess the SAR performance of the SoC in a quantitative manner, a total of 216 stimulus artifacts (119 of 120 and 97 of 121 artifacts from case #1 and #2, respectively) were analyzed. Specifically, the mean and standard deviation of the rms values of the artifacts were computed pre- and post-processing by the SAR processor of the DSP unit. The analysis excluded the very first artifact in each neural dataset and those artifacts in case #2 dataset that had neural spikes present anywhere in their 10-ms duration over which the SAR processor was operating. This ensured that the occasional presence of neural spikes did not confound the analysis. The same statistics were also obtained from segments of the SoC output that represented pure noise (i.e., absence of both neural spikes and artifact residuals).

Table 2 tabulates the results of this analysis. As can be seen, the mean rms value of the artifact was reduced by a factor of  $\sim 30$  and  $\sim 24$  in case #1 and #2 (template error  $\leq 1\%$ ), respectively, resulting in post-processed rms values that were at the level of that for the output noise after template subtraction and residual blanking.

## 6 Conclusion

This paper reported on a bidirectional neural interface SoC for combined spike recording, electrical microstimulation, and real-time stimulus artifact removal based on template subtraction. In particular, the SoC integrated a low-power DSP unit that could generate a high-fidelity template signal representative of the stimulus artifacts via IIR temporal

filtering and then subtract it from the contaminated neural data to remove the artifacts. The SoC functionality was demonstrated in neurobiological tests with isolated buccal ganglia of an *Aplysia* by removing large stimulus artifacts in real time from the contaminated data record and recovering the neural activity that occurred on the tail end of the artifacts. The power consumption of the spike-recording front-end and DSP unit were measured to be  $\sim 27 \mu\text{W}$  and  $<25 \mu\text{W}$ , respectively, from 1.5 V.

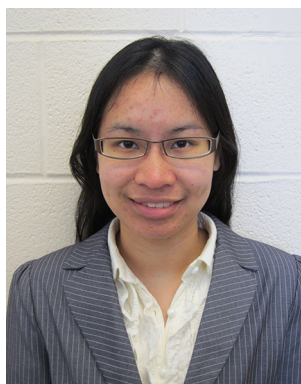
One limitation of this approach is that it does not address the problem of amplifier saturation and hence is less effective with prolonged amplifier saturation, unless care is taken in the design of the recording and stimulating circuitry to prevent or minimize amplifier saturation by decreasing the duration and amplitude of the artifacts [10–12]. On the other hand, the major advantage of this approach as compared to blanking (i.e., disconnecting the recording amplifier input during stimulation) is the potential to retain signal information during stimulation, while fully eliminating large stimulus artifacts from the contaminated data record in real time.

**Acknowledgments** This work was supported by the Department of Defense Traumatic Brain Injury—Investigator-Initiated Research Award Program under Award W81XWH-10-1-0741 (to P. Mohseni) and National Institutes of Health grant NS047073 (to H. J. Chiel). The authors would like to thank J. McManus, Case Western Reserve University, Cleveland, OH, for his assistance in conducting the neurobiological experiments, as well as Dr. D. Guggenmos and Prof. R. Nudo, University of Kansas Medical Center, Kansas City, KS, for providing the prerecorded rat neural dataset. The authors would also like to thank Dr. M. Azin, QualComm, San Diego, CA, and Prof. M. Buchner, Case Western Reserve University, for helpful discussions that made this work possible.

## References

- McGill, K. C., Cummins, K. L., Dorfman, L. J., Berlizot, B. B., Luettmeyer, K., Nishimura, D. G., & Widrow, B. (1982). On the nature and elimination of stimulus artifact in nerve signals evoked and recorded using surface electrodes. *IEEE Transactions on Biomedical Engineering*, 29(2), 129–137.
- Guggenmos, D. J., Azin, M., Barbay, S., Mahnken, J. D., Dunham, C., Mohseni, P., & Nudo, R. J. (2013). Restoration of function after brain damage using a neural prosthesis. *Proceedings of the National Academy of Sciences of the USA (PNAS)*, 110(52), 21177–21182.
- Azin, M., Guggenmos, D. J., Barbay, S., Nudo, R. J., & Mohseni, P. (2011). A battery-powered activity-dependent intracortical microstimulation IC for brain-machine-brain interface. *IEEE Journal of Solid-State Circuits*, 46(4), 731–745.
- Shahrokhi, F., Abdelhalim, K., Serletis, D., Carlen, P. L., & Genov, R. (2010). The 128-channel fully differential digital integrated neural recording and stimulation interface. *IEEE Transactions on Biomedical Circuits and Systems*, 4(3), 149–161.
- Sharma, V., McCreery, D. B., Han, M., & Pikov, V. (2010). Bidirectional telemetry controller for neuroprosthetic devices. *IEEE Transactions on Neural Systems and Rehabilitation Engineering*, 18(1), 67–74.
- DeMichele, G., & Troyk, P. R. (2003). Stimulus-resistant neural recording amplifier. In *Proceedings of the 25th Annual International IEEE Engineering in Medicine and Biology Conference (EMBC'03)* (pp. 3329–3332).
- Hines, A. E., Crago, P. E., Chapman, G. J., & Billian, C. (1996). Stimulus artifact removal in EMG from muscles adjacent to stimulated muscles. *Journal of Neuroscience Methods*, 64(1), 55–62.
- Nikolic, Z. M., Popovic, D. B., Stein, R. B., & Kenwell, Z. (1994). Instrumentation for ENG and EMG recordings in FES systems. *IEEE Transactions on Biomedical Engineering*, 41(7), 703–706.
- Jadvar, H., & Benson Jr., D. W. (1989). A stimulus artifact suppressor for esophageal pacing studies: Design and clinical testing. In *Proceedings of the 11th Annual International IEEE Engineering Medicine Biology Conference* (pp. 1401–1402).
- Brown, E. A., Ross, J. D., Blum, R. A., Nam, Y., Wheeler, B. C., & DeWeerth, S. P. (2008). Stimulus-artifact elimination in a multielectrode system. *IEEE Transactions on Biomedical Circuits and Systems*, 2(1), 10–21.
- Blum, R. A., Ross, J. D., Brown, E. A., & DeWeerth, S. P. (2007). An integrated system for simultaneous multichannel neuronal stimulation and recording. *IEEE Transactions on Circuits and Systems: Part I*, 54(12), 2608–2618.
- Hanson, T. L., Omarsson, B., O'Doherty, J. E., Peikon, I. D., Lebedev, M. A., & Nicolelis, M. A. L. (2012). High-side digitally current-controlled biphasic bipolar microstimulator. *IEEE Transactions on Neural Systems and Rehabilitation Engineering*, 20(3), 331–340.
- Wagenaar, D. A., & Potter, S. M. (2002). Real-time multichannel stimulus artifact suppression by local curve fitting. *Journal of Neuroscience Methods*, 120(2), 113–120.
- Hashimoto, T., Elder, C. M., & Vitek, J. L. (2002). A template subtraction method for stimulus artifact removal in high-frequency deep brain stimulation. *Journal of Neuroscience Methods*, 113(2), 181–186.
- Wichmann, T. (2000). A digital averaging method for removal of stimulus artifacts in neurophysiologic experiments. *Journal of Neuroscience Methods*, 98(1), 57–62.
- Wichmann, T., & Devergnas, A. (2011). A novel device to suppress electrical stimulus artifacts in electrophysiological experiments. *Journal of Neuroscience Methods*, 201(1), 1–8.
- Azin, M., Chiel, H. J., & Mohseni, P. (2007). Comparisons of FIR and IIR implementations of a subtraction-based stimulus artifact rejection algorithm. In *Proceedings of the 29th Annual International IEEE Engineering Medicine Biology Conference (EMBC'07)* (pp. 1437–1440).
- Limnuson, K., Lu, H., Chiel, H. J., & Mohseni, P. (2014). Real-time stimulus artifact rejection via template subtraction. *IEEE Transactions on Biomedical Circuits and Systems*, 8(3), 391–400.
- Limnuson, K., Lu, H., Chiel, H. J., & Mohseni, P. (2014). A bidirectional neural interface SoC with an integrated spike recorder, microstimulator, and low-power processor for real-time stimulus artifact rejection. In *Proceedings of IEEE Custom Integrated Circuits Conference (CICC'14)*.
- Hunter, J. S. (1986). The exponentially weighted moving average. *The Journal of Quality Technology*, 18(4), 203–210.
- Oppenheim, A. V., & Schafer, R. W. (2010). *Discrete-time signal processing*. Upper Saddle River, NJ: Prentice-Hall.
- Harrison, R. R., & Charles, C. (2003). A low-power low-noise CMOS amplifier for neural recording applications. *IEEE Journal of Solid-State Circuits*, 38(6), 958–965.
- Jackson, A., Mavoori, J., & Fetz, E. E. (2006). Long-term motor cortex plasticity induced by an electronic neural implant. *Nature*, 444, 56–60.

24. Shahroost, S., Frost, S., Van Acker, G., DeJong, S., Dunham, C., Barbay, S., Nudo, R., & Mohseni, P. (2014). Towards a miniaturized brain-machine-spinal cord interface (BMSI) for restoration of function after spinal cord injury. In *Proceedings of the 36th Annual International IEEE Engineering Medicine Biology Conference (EMBC'14)* (pp. 486–489).
25. Zimmermann, J. B., & Jackson, A. (2014). Closed-loop control of spinal cord stimulation to restore hand function after paralysis. *Frontiers in Neuroscience*, 8(87), 1–8.
26. Tsividis, Y. (1999). *Operation and modeling of the MOS transistor* (2nd ed.). New York, NY: Oxford University Press.
27. Demosthenous, A. (2014). Advances in microelectronics for implantable medical devices. *Advances in Electronics*. doi:[10.1155/2014/981295](https://doi.org/10.1155/2014/981295).
28. Sooksood, K., Stieglitz, T., & Ortmanns, M. (2008). An experimental study on passive charge balancing. In *Proceedings of the Annual Conference International Functional Electrical Stimulation Society (IFESS'08)*.
29. Ortmanns, M. (2007). Charge balancing in functional electrical stimulators: A comparative study. In *Proceedings of the IEEE International Symposium Circuits and Systems (ISCAS'07)* (pp. 573–576).
30. Arora, M. (2012). *The art of hardware architecture: Design methods and techniques for digital circuits*. New York, NY: Springer-Verlag.
31. Limnuson, K., Lu, H., Chiel, H. J., & Mohseni, P. (2011). FPGA implementation of an IIR temporal filtering technique for real-time stimulus artifact rejection. In *Proceedings of the IEEE Biomedical Circuits and Systems Conference (BioCAS'11)* (pp. 49–52).
32. McManus, J. M., Lu, H., & Chiel, H. J. (2012). An in vitro preparation for eliciting and recording feeding motor programs with physiological movements in *Aplysia californica*. *Journal of Visualized Experiments*, 70, e4320. doi:[10.3791/4320](https://doi.org/10.3791/4320).
33. Cullins, M. J., & Chiel, H. J. (2010). Electrode fabrication and implantation in *Aplysia californica* for multichannel neural and muscular recordings in intact, freely behaving animals. *Journal of Visualized Experiments*, 40, e1791. doi:[10.3791/1791](https://doi.org/10.3791/1791).



**Kanokwan Limnuson** (S'09) earned her B.Eng. degree from Chulalongkorn University, Bangkok, Thailand in 2004 and her M.S. degree from Case Western Reserve University, Cleveland, Ohio in 2008; both were in electrical engineering. She is presently a Ph.D. candidate in the BioMicroSystems Laboratory at Case Western Reserve University. Her research interests are the development of neural signal-processing algorithms and their low-power implementation with analog and VLSI circuitry for bidirectional neural interfaces.



**Hui Lu** was born in 1981. She received the B.S. degree in biology from Nanjing University, Nanjing, China in 2003. She is currently working toward her Ph.D. degree in biology at Case Western Reserve University. Her research focuses on neural motor control and neuromodulation of the adaptive feeding behaviors in the marine mollusk *Aplysia californica*. She has published seven peer-reviewed journal papers.



**Hillel J. Chiel** received the B.A. degree in English from Yale University, New Haven, CT, and the Ph.D. degree in neural and endocrine regulation from Massachusetts Institute of Technology (MIT), Cambridge. After postdoctoral work at the Center for Neurobiology and Behavior at Columbia University's College of Physicians and Surgeons and in the Department of Molecular Biophysics at AT&T Bell Laboratories, he joined the faculty of Case Western Reserve University, Cleveland, OH. He is currently a Professor of Biology, with secondary appointments in the Departments of Neurosciences and Biomedical Engineering. His research focuses on the biomechanical and neural mechanisms of adaptive behavior, using the marine mollusk *Aplysia californica* as a model system. His research has led to the development of novel technology for imaging muscle movements and neural activity in intact animals, and biologically inspired soft robots. He has been a Fellow of the Institute of Physics since 2004. He served as guest co-editor of a special issue on Applied Neurodynamics for the Journal of Neural Engineering with Dr. Peter Thomas in December 2011. Dr. Chiel also serves on the editorial boards of the Journal of Neural Engineering, Soft Robotics, and the Journal of Visualized Experiments. In 2012, he won a prize from the magazine Science (published by the American Association for the Advancement of Science) for Inquiry Based Education. He is a holder of four patents and has published over 115 peer-reviewed publications.



**Pedram Mohseni** (S'94–M'05–SM'11) was born in 1974. He received the B.S. degree from the Sharif University of Technology, Tehran, Iran, in 1996, and the M.S. and Ph.D. degrees from the University of Michigan, Ann Arbor, MI, USA, all in electrical engineering, in 1999 and 2005, respectively. Currently, he is a tenured Associate Professor in the Electrical Engineering and Computer Science Department at Case Western Reserve University,

Cleveland, OH, USA, with a secondary appointment in the Biomedical Engineering Department. His research interests include analog/mixed-signal/RF integrated circuits and microsystems for neural engineering, interface circuits for micro/nano-scale sensors/actuators,

wireless sensing/actuating systems for brain-machine interfaces, biomedical microtelemetry, and assembly/packaging of biomicrosystems. Dr. Mohseni has been an Associate Editor for the IEEE Transactions on Circuits and Systems-Part II (2010–2012), IEEE Transactions on Biomedical Circuits and Systems (2008–present), and IEEE Transactions on Neural Systems and Rehabilitation Engineering (2012–present). In addition he was a Guest Editor for the IEEE Journal on Emerging and Selected Topics in Circuits and Systems in 2011. He also serves on the Technical Program Committee of the IEEE CICC and RFIC Symposium. He was the recipient of the EECS Faculty Research Award for Exceptional Achievement in 2008, National Science Foundation CAREER Award in 2009, Case School of Engineering Research Award in 2011, EECS Mihajlo “Mike” Mesarovic Award for Extraordinary Impact in 2013, and earned the first-place prize of the Medical Device Entrepreneur’s Forum at the 58th annual conference of the ASAIO in 2012. He is a member of the IEEE Solid-State Circuits, Circuits and Systems, and Engineering in Medicine and Biology Societies, as well as the administrative committee (AdCom) of the IEEE Sensors Council.



# Current Challenges Facing the Translation of Brain Computer Interfaces from Preclinical Trials to Use in Human Patients

Maxwell D. Murphy<sup>1,2</sup>, David J. Guggenmos<sup>2</sup>, David T. Bundy<sup>2</sup> and Randolph J. Nudo<sup>2,3\*</sup>

<sup>1</sup> Bioengineering Graduate Program, University of Kansas, Lawrence, KS, USA, <sup>2</sup> Department of Rehabilitation Medicine, University of Kansas Medical Center, Kansas City, KS, USA, <sup>3</sup> Landon Center on Aging, University of Kansas Medical Center, Kansas City, KS, USA

Current research in brain computer interface (BCI) technology is advancing beyond preclinical studies, with trials beginning in human patients. To date, these trials have been carried out with several different types of recording interfaces. The success of these devices has varied widely, but different factors such as the level of invasiveness, timescale of recorded information, and ability to maintain stable functionality of the device over a long period of time all must be considered in addition to accuracy in decoding intent when assessing the most practical type of device moving forward. Here, we discuss various approaches to BCIs, distinguishing between devices focusing on control of operations extrinsic to the subject (e.g., prosthetic limbs, computer cursors) and those focusing on control of operations intrinsic to the brain (e.g., using stimulation or external feedback), including closed-loop or adaptive devices. In this discussion, we consider the current challenges facing the translation of various types of BCI technology to eventual human application.

## OPEN ACCESS

### Edited by:

Surjo R. Soekadar,  
University Hospital of Tübingen,  
Germany

### Reviewed by:

Euan Robert Brown,  
Heriot-Watt University, UK  
Junichi Ushiba,  
Keio University, Japan

### \*Correspondence:

Randolph J. Nudo  
mudo@kumc.edu

**Received:** 24 July 2015

**Accepted:** 10 December 2015

**Published:** 06 January 2016

### Citation:

Murphy MD, Guggenmos DJ, Bundy DT and Nudo RJ (2016) Current Challenges Facing the Translation of Brain Computer Interfaces from Preclinical Trials to Use in Human Patients. *Front. Cell. Neurosci.* 9:497. doi: 10.3389/fncel.2015.00497

**Keywords:** brain-computer interface (BCI), microelectrodes, electrocorticography (ECoG), electroencephalography (EEG), closed-loop neuroprosthetic devices, neural prostheses

## INTRODUCTION

Brain-computer interfaces (BCIs) and their applications for treatment of nervous system damage have shown enormous progress as functional restoration tools in pre-clinical studies. In general, most BCIs are designed to bypass damaged structures and fiber tracts. BCIs range from common devices, such as cochlear implants that use externally recorded sound to directly stimulate auditory nerve fibers, to devices that derive control signals from cortical activity, allowing individuals with paresis to operate a prosthetic device. Other BCIs are designed to aid in acute rehabilitation training sessions. Regardless of the type, the major purpose of BCIs is to improve the quality of life for the patients who use them.

Damage to the nervous system can result in profound sensory, motor, and cognitive deficits that strongly impact day-to-day functioning of afflicted individuals. The type and extent of these deficits are dependent upon the location and extent of the injury. Injuries affecting motor cortex, such as might occur after a focal traumatic brain injury or stroke, can lead to impaired use of digits, limbs, or whole regions of the body due to loss of descending corticospinal neurons or disruption of sensory-motor integration. Spinal cord injury impacts

communication of neural signals at the site of injury, leading to motor, sensory and autonomic deficits. For these types of injuries, there are no effective post-acute restorative treatments. Research in stem cell therapy to regenerate damaged neurons that could restore damaged pathways is currently underway (Gavins and Smith, 2015; Hosseini et al., 2015; Sharma et al., 2015; Sullivan et al., 2015), but is likely years from fruition. Recovery after central nervous system (CNS) injury is thought to manifest itself through neuroplastic mechanisms, which have been shown to be aided through rehabilitative therapy (Nudo et al., 1996; Nudo and Friel, 1999). Dramatic recovery from motor deficits has occurred in some cases (Bajaj et al., 2015; Warnecke et al., 2015), but recovery from neurological injuries rarely results in a full restitution of function. Effectiveness of any therapy is constrained by the type and extent of injury, efficiency of neuroplastic mechanisms involved, and type of intervention. BCIs offer a pathway, in conjunction with rehabilitative therapy, for promoting restitution of function.

Current technology available for clinical populations ranges from simple devices that stabilize a shaking hand (Popović Maneski et al., 2011; Grimaldi et al., 2013), to devices that augment the ability of a patient with locked-in syndrome to communicate with others (Holz et al., 2015). While these technologies offer promise for recovery from or for relief of symptoms of CNS injury, there are still many challenges in the integration of BCIs into effective prosthetic devices. These challenges include adequate spatiotemporal resolution in interpreting information recorded from the brain for naturalistic control, decoding a sufficient number of degrees of freedom to maintain natural movements, integration of feedback mechanisms, easing the technological support needed for integration of the BCI and reducing the invasiveness of components while maintaining the longevity of signal acquisition. Additionally, a number of recent studies have focused on devices contained entirely within the CNS that create artificial links between related areas. Here, we focus on the advantages and disadvantages of various approaches to interfacing BCI devices with the nervous system, based on results from both pre-clinical and clinical studies. We highlight the challenges associated with the implementation of high fidelity BCI devices to a clinical setting, possible methods for overcoming these challenges, and the distinction between devices that control extrinsic operations and those that control operations intrinsic to the CNS.

## BCI OPERATING MODES

When considering potential clinical interventions using neural prostheses, a convenient way of classifying devices is based on whether they control extrinsic or intrinsic operations. In this review, BCI devices that operate primarily by detection of electrical signals from the CNS are mainly considered, as techniques for recording other measures of CNS information (i.e., magnetic, metabolic) are typically unwieldy for chronic use or cost prohibitive.

## Control of Extrinsic Operations

Neural prostheses are classified as controlling extrinsic operations when the device contains a decoder that records CNS signals in real-time, modifies those signals via a control algorithm and outputs the translated and modified signal to a body-external device such as a prosthetic or robotic limb or a computer cursor. In this way the individual gains control over an artificial device that has the possibility to be incorporated into the body schema.

A limitation of devices controlling extrinsic operations is that accuracy in decoding movement intention is typically gained through an increase in the number of recording channels (Carmena et al., 2003); however, increasing recording channels brings the challenge of increasing channel density in a particular location of interest. Depending on the type of information being recorded and the decoding strategy, the increase in computational burden and power required from adding greater numbers of channels may also become nontrivial. Likewise, increasing the invasiveness of the electrodes can lead to increases in decoding accuracy, but at the cost of increased surgical risk and potential immune response (Ward et al., 2009). Additionally, chronic recordings are prone to drift in intent decoding, making repeated calibration necessary. Although these limitations prevent the widespread use of these BCI systems in clinical settings, studies to date are encouraging and represent tangible evidence of the type of functional restoration that can be achieved using BCIs. Here, BCIs controlling extrinsic operations are classified into three different categories based on the electrode interface used for signal acquisition from the CNS (**Figure 1**). These include two invasive electrode-CNS interface approaches [microelectrode array (MEA) recording, electrocorticography (ECoG)] and one non-invasive electrode-CNS interface (electroencephalography, EEG).

### Microelectrode Array Recording

MEA recording, used in animal models for decades, represents the most invasive BCI approach, as penetrating microelectrodes are placed within the brain structure itself, typically within the gray matter of cerebral cortex. Though the technology was initially developed in animal models, a relatively small number of human studies have now been conducted with implanted MEAs. Microelectrode probes can range from a single-shank electrode to arrays consisting of tens of thousands of recording sites. The specific pattern and distribution of sites allows for dense population recordings throughout a single or multiple regions of interest. MEAs allow the highest spatial and temporal resolution of any type of neurophysiological recording system used in BCIs (Obien et al., 2015), but at the expense of spatial coverage at the site of recording. The use of MEAs allows for detection of the extracellular electric field changes reflecting the membrane potential of the individual neurons closest to the tip of each microelectrode.

While the voltage changes are quite small, neuronal action potentials, or spikes, can be detected within the electrical signal since rapid changes in membrane potential associated with the opening and closing of membrane ion channels have a characteristic temporal pattern. Due to their rapid onset and

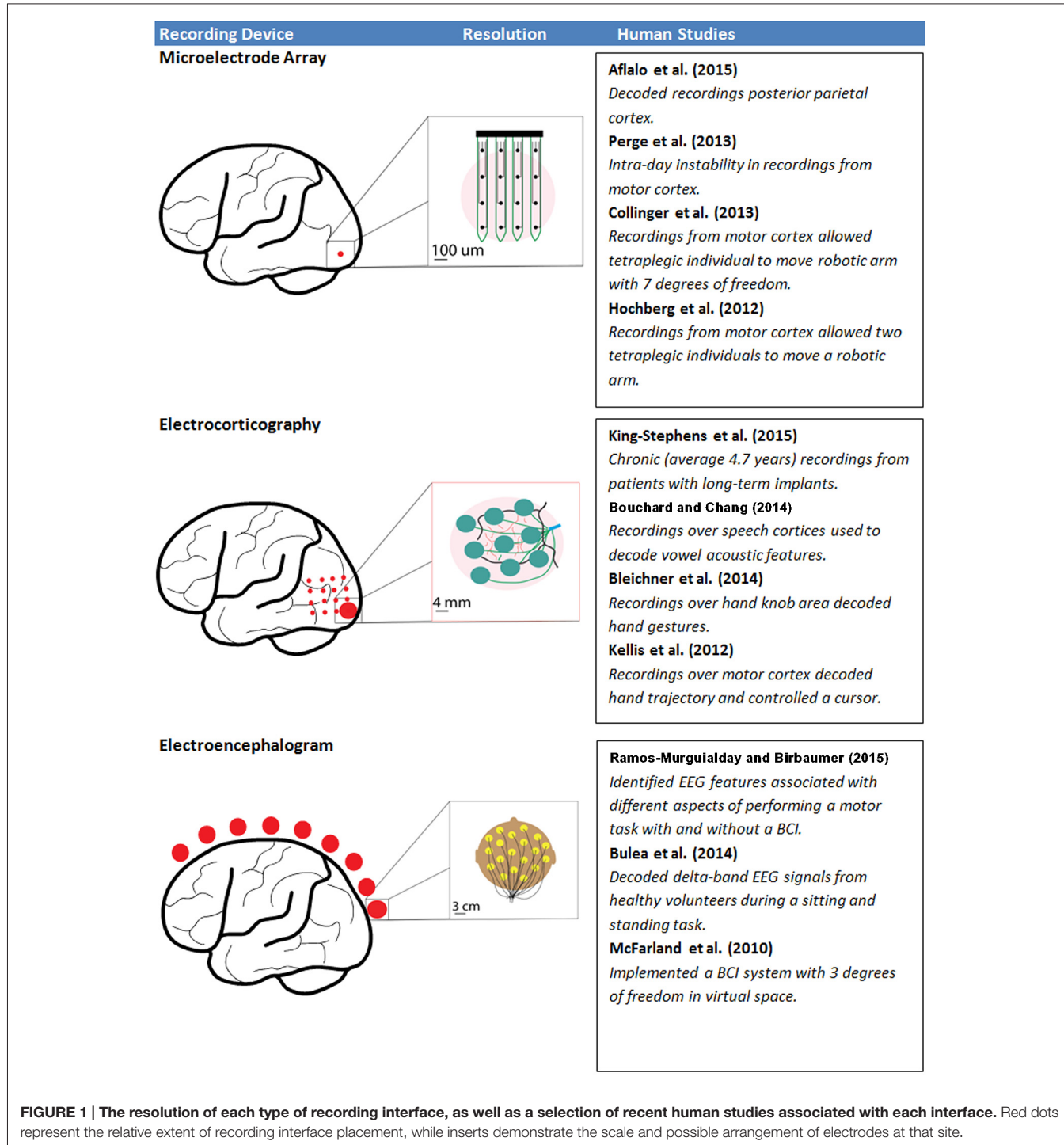


**FIGURE 1 |** The resolution of each type of recording interface, as well as a selection of recent human studies associated with each interface. Red dots represent the relative extent of recording interface placement, while inserts demonstrate the scale and possible arrangement of electrodes at that site.

offset, the resulting detected spikes can be effectively reduced to point processes using voltage thresholding, simplifying the design of decoding algorithms, especially when large MEAs are employed. Further analysis using automated or semi-automated clustering algorithms or manual feature detection allows classification of multiple individual neurons recorded from a given recording site, increasing the accuracy of decoding

(Todorova et al., 2014). It should, however, be noted that the process of detecting spikes introduces another source of error, with some techniques sacrificing accuracy for the sake of computational expedience (Rey et al., 2015). Depending on the information that needs to be obtained from spike trains, these errors can have a nontrivial significance (Pazienti and Grün, 2006).

Once spikes have been detected and multiple neuronal spikes discriminated (if desired), typically the rate of firing (i.e., spike rate) of the individual neuronal components is calculated. Both accuracy and ease of computational processing are dependent upon the combined choice of a spike rate estimator and a spike rate decoder, with simpler methods allowing computations to be performed on a millisecond time scale and more complex, probabilistic models limiting computations to seconds or even minutes (Cunningham et al., 2009). Based on these temporal limitations, the practical need for real-time adaptation when implementing a BCI makes some of the simpler methods more attractive (Cunningham et al., 2011). To this end, it has been demonstrated that the use of a closed-loop, adaptive decoder can also lead to increased simultaneous neural adaption, resulting in improved skill retention (Orsborn et al., 2014).

Preclinical BCI research in animal models has typically utilized implanted MEAs chronically embedded in the cortex for decoding movement intention. The rationale for this approach dates to the 1960s when Evarts found that neurons in the motor cortex of non-human primates (NHPs) altered their firing patterns immediately prior to the onset of movement (Evarts, 1966) and was later strengthened when Fetz (1969) demonstrated that neuronal firing rate could be volitionally controlled. More recent studies in NHPs demonstrate a consistent ability to decode signals to move transiently paralyzed limbs (Ethier et al., 2012), a simulated or robotic limb (Wessberg et al., 2000; Carmena et al., 2003; Velliste et al., 2008; Willett et al., 2013), or a cursor on a screen (Taylor et al., 2002; Wu et al., 2004; Nuyujukian et al., 2014), and even predict hand orientation with extremely high accuracy (Peng et al., 2014).

MEAs have proven resilient in producing reliable signals from a single area over periods of up to a year (Flint et al., 2013). However, longevity of single unit recordings with indwelling electrodes has been one of the major limitations of this approach. For example, studies have shown a decay in signal strength over the course of 100 days (Rousche and Normann, 1999), and large performance variability between trials and type of electrode used (Ward et al., 2009). Furthermore, information generated by decoders has been shown to diminish over extended implantations (Nuyujukian et al., 2014). This somewhat variable, and arguably short, lifetime limit for recording robust signals from implanted MEAs still needs to be addressed by future improvements in MEA materials technology. While estimates of the number of neurons needed to decode arm movements off-line range between 150 neurons with serial single unit recordings and 600 units from MEAs (Georgopoulos et al., 1986), accurate on-line BCI control is possible with far fewer recorded units due to the closed-loop adaptation that occurs when learning BCI skills (Taylor et al., 2002; Carmena et al., 2003). This phenomenon could be a key to improving long-term patency of indwelling MEAs. If it is possible to use only a subset of sites to generate information for decoding, then as those sites slowly lose functionality it may be possible to use redundant sites, allowing for an extended prosthetic lifespan.

Although MEA studies in humans are limited due to their invasive nature, recent results indicate the advantages of using such high-resolution paradigms. Aflalo et al. (2015) found that

the decoding of spike trains associated with motor imagery in a patient chronically implanted with MEAs embedded in the posterior parietal cortex resulted in the smooth movement of a robotic limb with 17 degrees-of-freedom. Two 96-channel MEAs were embedded for 21 months with no signs of adverse effects. The subject was asked to imagine reaching toward a specific goal, and channels that demonstrated preferential firing when the subject imagined achieving the goal were discriminated from neurons tuned to trajectory. When these goal-tuned units were used as tuners for accomplishing a specific task, decoding accuracy was higher for a given number of units. It should be noted, however, that the goal-tuned units changed over time, indicating that an adaptive decoder would be important for this sort of prosthetic device to be implemented in the future for long-term implantations. This problem of varying tuning is also seen in recordings from units in motor cortex (Perge et al., 2013).

These changes in tuning were most likely due to physiological changes in the neuronal firing patterns as a result of adaptation to the decoder. As the patient learns to operate the BCI, functional reorganization occurs in multiple brain areas, resulting from closed-loop feedback and adaptation to performing the new BCI-related task, and presumably allowing a smaller number of units to function in tuning the device (Taylor et al., 2002; Carmena et al., 2003). The ability to produce a smooth movement based on the decoding of a goal-tuned unit represents a significant divergence from previous studies involving chronically implanted MEAs in human patients. These studies used motor cortex (Hochberg et al., 2006, 2012; Collinger et al., 2013) as an area for control, and were quite successful; however, a noted limitation was that movements produced using these systems were slower and somewhat inflexible (Hochberg et al., 2012) when compared to natural reaching movements. Thus, the ability to use a goal-tuned unit in posterior parietal cortex as a control source for decoding intent using motor imagery could serve as an informative alternative to decoders focused on motor cortex.

There are several additional challenges related to using MEAs in BCIs for clinical populations. The insertion of MEAs into cortical tissue is an invasive procedure requiring a craniotomy and resection of the dura. The surgical procedure introduces a possible pathway for infection. MEA implantation can lead to small-scale tissue damage that increases with a greater number of implants. Glial scarring occurs at the insertion site, and is thought to be a major factor reducing the longevity of useable signals that can be recorded in a chronically implanted individual. Another major problem of chronically implanted MEAs is micro-motion, which causes the formation of scar tissue, leading to a decrease in the quality of recordings over time (Williams et al., 2007; Ersen et al., 2015). Current materials research is focusing on changing various properties affecting the stiffness of the microelectrode, in the hope that scar tissue formation caused by micro-motion will be minimized (De Faveri et al., 2014). Obien et al. (2015) provide a comprehensive review of the different types of MEAs currently in use. The viability of MEAs in clinical use may ultimately depend upon further advances in materials research (McCarthy et al., 2011; Tooker et al., 2012; Felix et al., 2013; De Faveri et al., 2014).

A potential solution for MEA signal stability would be to implement BCIs that utilize somewhat lower-fidelity neural signals. One signal that can be acquired by MEAs is the local field potential (LFP). The LFP represents the summation of active cellular processes nearest the site of each microelectrode. While the general process of analysing LFPs is similar to analysing spike data, the computational stage and filtering is somewhat different (**Figure 2**), and some delay is inherent due to the latency with which changes in spectral power occur and can be measured. Despite these limitations of LFPs, the advantages of increased recording stability may outweigh the loss in accuracy.

A combination of lower-fidelity LFP recordings and spike recordings might also be desirable. It is possible to generate predictions of the imagined single-joint movements in a tetraplegic individual by decoding the joint trajectory using the LFP frequency signals and multi-unit spike activity similarly to those predicted by decoding single-unit activity (Ajiboye et al., 2012). Recent work by Hall et al. (2014) indicates that it is possible to estimate single unit firing rates using the slow potentials from LFPs derived at several cortical locations. If this method can be applied to estimate the single unit firing rate of a single unit, without the need for first gathering spike data to calibrate the estimation, it could lead to the development of a BCI with sufficient longevity that still offers good spatiotemporal resolution. However, it is important to note that the filters used to perform the necessary calculations to deconvolve the firing rate of a single neuron from the low frequency LFP signals using current methods require prior knowledge of spike train information from multiple neurons. Furthermore, when using single-unit activity decoded from LFPs, there is an additional step of transforming the data during which accuracy could be lost. Despite these limitations, the method described by Hall et al. (2014) offers the added benefit of allowing accurate single unit firing rate predictions over the course of several weeks, which is an improvement on intra-day instabilities in decoding from single-unit activity itself (Perge et al., 2013). In this way, using LFP decoders in conjunction with single- and multi-unit activity may be a key step in implementing long-term implants.

### Electrocorticography Grids

ECoG consists of a mesh or grid of electrodes distributed across the cortical surface that can be placed either subdurally or epidurally. This technique can detect the LFPs from the cortical surface at specific locations, but does not have the resolution to detect individual spikes. As less invasive interface approaches are used, the focality of the recorded signal necessarily is degraded. What ECoG lacks in spatiotemporal precision with respect to individual spiking profiles, it makes up for in patency. ECoG has shown resilience in long-term recordings in human patients implanted for up to 7.1 years (King-Stephens et al., 2015). In addition, ECoG has the ability to expand the extent of spatial coverage relative to MEAs. For example, signals can be detected and decoded simultaneously from M1, PMd, and S1. Additionally, using this method, it is possible to detect not only recordings from gyrus, but also from the sulcal wall (Yanagisawa et al., 2009), albeit via a more invasive process.

In humans, most studies investigating the use of ECoG for BCI applications have used clinical electrodes implanted in epilepsy patients for localization of epileptic foci with an electrode size on the order of a few millimeters and an interelectrode distance of approximately 1 cm. In particular, movement-related spectral power changes have been shown to occur not only during overt movements of skeletal musculature, but also during imagined movements (Leuthardt et al., 2004), indicating that these spectral power changes may be useful in motor-impaired patients who are unable to perform overt movements. Furthermore, several studies have demonstrated that functionally motor-intact human patients can modulate the spectral power of ECoG signals to achieve on-line control of a computer cursor (Leuthardt et al., 2004; Wilson et al., 2006; Felton et al., 2007; Schalk et al., 2008).

ECoG has also been used to implement BCI devices in motor-impaired patients. A study in a hemiparetic patient demonstrated that it is possible to use ECoG to control a prosthetic arm using recordings from sensorimotor cortex (Yanagisawa et al., 2011). Additionally, the use of ECoG signals for control of a BCI system with three degrees-of-freedom based upon motor imagery of movements at multiple independent joints has been demonstrated in a quadriplegic patient with good signal quality for durations up to 1 month (Wang et al., 2013). While on-line BCI control in human patients with ECoG has been limited to short durations, with relatively large electrode sizes, arrays with sub-millimeter electrode sizes have been proposed as a means to obtain signals with increased spatial specificity. These micro-scale arrays have been utilized for online BCI control experiments in NHPs (Leuthardt et al., 2009; Rouse et al., 2013). Importantly, these studies utilized chronic epidural recordings, demonstrating the stability of ECoG signals as well as the potential to implant ECoG BCI systems on the surface of the dura, which would reduce the risks of infection due to isolating the implant from the subdural space.

While closed-loop BCI systems generally have used changes in spectral power associated with imagined movements of a single joint in humans or high gamma power in arbitrary electrodes in NHPs, a more natural control algorithm may be to use signals decoded from natural movements or behaviors. The potential for this type of BCI using ECoG has been demonstrated by studies that have used ECoG signals to decode 2D movement directions in rats (Slutzky et al., 2011) and NHPs (Flint et al., 2012) and to continuously decode movement kinematics of 2D (Flint et al., 2012; Marathe and Taylor, 2013) and 3D arm movements in NHPs (Chao et al., 2010). Along with animal models, ECoG recordings from human epilepsy patients have been used to decode information about voluntary movements. ECoG recordings have been used to classify movement directions of arm and hand movements (Reddy et al., 2009; Wang et al., 2012; Chestek et al., 2013). Similarly, it is possible to decode continuous finger flexion/extension (Chestek et al., 2013) and 2D arm and hand trajectories using ECoG with modest accuracy (Schalk et al., 2007; Pistohl et al., 2008; Sanchez et al., 2008; Kellis et al., 2012), as well as move a cursor to an onscreen target using full neural control with no trajectory decoding (Kellis et al., 2012). Flint et al. (2014) extended these findings

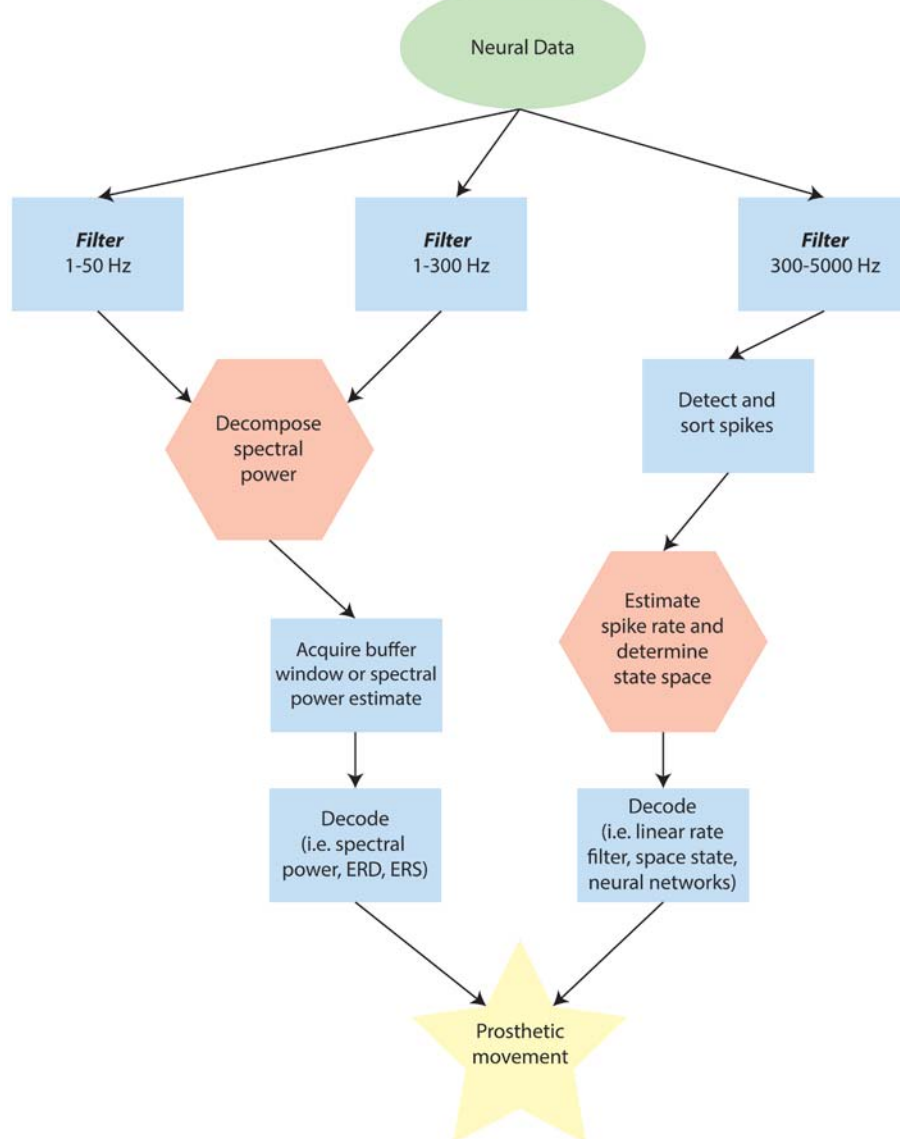


**FIGURE 2 | Schematic of possible differences in analysing point-processes and waveforms when using externally interfaced motor prosthetics.** Note that this flow may change depending on the specific device, but is designed to provide a broad overview for comparison. In the diagram, the green ellipse represents data that has been recorded and amplified from the neural source. Blue rectangles are stages along the processing pathway that are typical for many devices. Red hexagons represent potential rate-limiting steps in determining the latency of the Brain Computer Interface (BCI) response to immediate internal changes in patterns of neural activity.

to show that it is possible not only to determine trajectory, but kinetics for use in functional electrical stimulation as well using ECoG (Flint et al., 2014). There are also preliminary indications that ECoG in patients with stroke and epilepsy can be used to predict three degrees-of-freedom in arm trajectory during motor imagery (Nakanishi et al., 2013). Other recent experiments have used high-density ECoG placed over specific areas to yield high accuracy decoding. Placement over the speech cortices yielded accurate prediction of vowel acoustics during speech (Bouchard and Chang, 2014), and placement over the hand knob area in sensorimotor cortex resulted in decoding of hand gesturing

(Bleichner et al., 2014), with high frequency signals ( $>65$  Hz) showing the most accurate results. In general, it should be noted that the higher frequency signals tend to produce more accurate results, presumably in part because there is a shorter latency between intent and decoding/feedback.

### Electroencephalography Caps

EEG is the least invasive technique, but also provides signals with the broadest spatiotemporal coverage of the cortex. Similar to ECoG, EEG detects general electric fields that are a sum of the electrical activity for a given region. However, as the

EEG signal detection is somewhat distant to the site of interest (e.g., the precentral gyrus) there is an inherent limitation to spatial and spectral resolution during signal acquisition. Because the voltage from a dipole falls off with the inverse of the square of the distance from the dipole, the extra distance between neural sources in the cortex and EEG electrodes causes a summation over a wider range of cortex (Cooper et al., 1965). The spectral resolution limitation is due primarily to the fact that higher frequency signals, which are more focal, tend to be averaged out by the low spatial resolution. In addition, high frequency activity in general is lower in amplitude than low frequency activity, and can be filtered out from the inherent dampening of the bone and tissue that it must travel through (Cooper et al., 1965) and Pfurtscheller and Cooper (1975). Finally, EEG signals are also susceptible to contamination from electromyographical (EMG) artifacts or eye blinks (Cooper et al., 1965; Wolpaw and McFarland, 2004). Due to these complications, trajectory predictions using EEG are generally not as accurate as those using MEA recording or ECoG.

Despite these limitations, EEG provides an excellent method for obtaining neural information from patients in a clinical setting without the need for surgery. EEG is also promising for use in acute settings that could be associated with rehabilitation and behavioral recovery, since it is non-invasive in nature. One of the hopes for EEG is that by using proper placement of a sufficient number of leads and a significant amount of prior data in healthy patients, it will be possible to use frequency signatures from different areas to overcome some of the spatiotemporal problems listed previously. As noted previously, EEG has the advantage of broad spatial coverage in recordings. It may be possible to turn this broad spatial coverage into an advantage in resolving the origin of activity in the brain. There is a large body of work in EEG source imaging that focuses on estimating the location of current sources for scalp measurements by solving the so-called static electromagnetic inverse problem. This is done using the collection of scalp measurements as well as a set of reasonable *a priori* constraints based on the assumed or measured physiology of the brain to determine the most likely origin of the current source or sources. As Michel et al. (2004) detail in their review of such techniques, such estimates depend on a number of factors, including but not limited to the number and position of electrodes on the scalp, the solution algorithm used to solve the inverse problem, and the integration of MRI data to serve as a prior. Recent studies demonstrate that it is possible to incorporate such source estimation techniques to EEG recordings for potential use in future BCI applications (Aihara et al., 2012; Yoshimura et al., 2012).

Although a variety of signal analyses have been used for EEG BCI systems (Blankertz et al., 2004), a more traditional approach has been to utilize average features of the frequency spectrum in relation to a motor event. A common strategy is to identify periods of event-related desynchronization (ERD) as a cue for some BCI output. ERD itself is a decrease in a pre-defined spectral frequency band that can have a different physiological interpretation depending on the context of the task. Controlling a BCI system with ERD associated with motor movements has

particular relevance to motor-impaired populations. Because ERD has been shown to occur with imagined in addition to overt movements, it is applicable as a BCI control signal in patient populations that are unable to execute motor actions (Pfurtscheller et al., 1997). The application of EEG ERD-based BCI systems has been demonstrated in normal controls and patient populations (Wolpaw et al., 1991; Pfurtscheller et al., 2003; Blankertz et al., 2004; Wolpaw and McFarland, 2004; McFarland et al., 2010). While EEG is a powerful tool due to its ease of use and non-invasiveness, its use in BCI system development is hampered by the limitations described above. To date the best performance of an EEG BCI system in control of extrinsic operations is three degrees-of-freedom, which was only achieved after months of intensive training (McFarland et al., 2010).

Although EEG-based BCI that use ERD and event related synchronization (ERS) in various frequency bands are common, recent work has aimed at providing a more comprehensive picture of changes through various power bands through the duration of a variety of tasks. Depending on the task, and thereby, the neural circuits involved, different signal features may be important at different times relative to the event of interest. A recent study identified EEG features in healthy subjects related to several stages of motor activities (Ramos-Murguialday and Birbaumer, 2015). Ideally, when using EEG to control a BCI, the different components of a movement would have distinct feature signatures that could be detected. Indeed, in this study it was noted that there were distinct features during active and passive proprioception, active intention, and passive involvement in motor activity. Importantly, these features were significantly different when performing a BCI task as compared to other motor tasks, indicating that decoder design must take into account changes in EEG features depending on the type of activity involved.

Other less time-sensitive applications than fine motor movement may lend themselves to BCIs that utilize even lower frequency signals, sometimes referred to as slow cortical potentials (SCPs) or movement-related cortical potentials (MRPs). In these cases accuracy can be added by including pre-processing steps using a variety of methods to reject false positive signals. A recent study has demonstrated that it may even be possible to decode movement intent from delta-band (0.1–4 Hz) features, showing high accuracy in movement classification during a sitting-to-standing task in healthy volunteers (Bulea et al., 2014). In fact, BCIs using slow signals have application even beyond motor tasks, such as allowing communication via a spelling device for patients with locked-in syndrome (Birbaumer et al., 1999) or even allowing web-browsing for paralyzed patients (Bensch et al., 2007). Another recent direction for improving accuracy is seen in the development of the brain/neuronal computer interface (BCI). The recent distinction between BCI and BCI devices draws on the fact that the BCI makes use of other signals or current sources recorded from the body that are not located directly in the brain. Soekadar et al. (2015b) demonstrated that it is possible to use electrooculography (EOG) in conjunction with EEG to improve use of a grasping hand exoskeleton.

## Control of Intrinsic Operations

Some implantable devices operate by modifying the flow of information or causing modifications in the functional neural networks of the brain. These devices control what can be considered intrinsic operations in the brain. Devices in this category fall into two sets: open-loop and closed-loop stimulators. In open-loop stimulation, some form of stimulation is applied to a region of the brain with a frequency that is often determined using physiological parameters, but not necessarily correlated to the immediate activity of the brain. Such open-loop devices deliver a constant stream of current to the site of interest, as is predominant in deep brain stimulation (DBS), although recent studies have used closed-loop DBS for treatment of Parkinson's Disease (PD), epilepsy, and intention tremors, as will be noted. There is also interest in the application of open-loop stimulation in conjunction with BCI therapy; however, in the scope of this review we will mainly cover closed-loop devices.

### Closed-Loop Controlled Intrinsic Operations

By nature of their application in primarily remedying some sort of functional deficit to patients, most BCIs could be broadly considered as closed-loop devices by virtue of the feedback a patient receives, typically visually, from the device when using it. In this review, we will be more precise with the definition of closed-loop strategies, and break "closed-loop" into two subcategories. The first subcategory of closed-loop strategies incorporates the ongoing activity patterns in individual neurons or ensembles of neurons to determine when an electrical stimulus will be applied in another location. Thus, intrinsic control can facilitate the flow of information from one region of the brain to another (**Figure 3**). These strategies are not driven by patient recognition of some extrinsic goal, but rather form a completely internal closed-loop. Feedback from an applied stimulus that controls intrinsic operations is typically less overt, as electrical stimulation is generally at subthreshold levels for generating sensation or movement, and measures of functional outcome are harder to ascertain on a trial-by-trial basis. In contrast, such feedback results in gradual changes in network connectivity, cognitive function or memory. This feature of intrinsic control provides an additional challenge since the network changes are thought to rely on Hebbian learning mechanisms, as are discussed below. While it is true that at the synapse such a circuit would comprise a feed-forward system, it is generally the case that reciprocal anatomical projections exist between cortical areas (Donoghue and Parham, 1983; Zhang and Deschenes, 1998), leading to bi-directional information flow and thus closing the loop. Stimulation in this paradigm requires not only a high-fidelity signal to detect and decode trigger events, but a highly focal, transient stimulus delivery. This is relatively simple when using MEAs to deliver the stimulus, but becomes more challenging when using less focal types of stimulation such as epidural stimulators or transcranial magnetic stimulation that stimulate relatively large volumes of tissue.

In PD, it is thought that DBS can improve motor functioning by disrupting abnormal activity. To improve upon existing, open-loop DBS methods, one study in eight PD patients used frequency characteristics of LFPs recorded from the subthalamic

nucleus (STN) to determine when to stimulate. Since beta frequencies (13–30 Hz) are thought to correlate with impairment in PD, stimulating the STN only during periods of high beta activity provides an adaptive, or closed-loop, approach to DBS (Little et al., 2013). This adaptive DBS caused a significant increase in subjects' neurological scores compared with continuous or random DBS. A closed-loop BCI to control intrinsic operations has also been used in epilepsy patients. In a randomized multicenter double-blinded controlled trial of 191 subjects, ECoG electrodes were used to detect epileptiform activity in the recorded signal (Heck et al., 2014). Following detection of epileptiform activity, brief pulses of electrical stimulation were applied to the seizure focus, an approach known as responsive focal cortical stimulation (RNS). Subjects receiving RNS showed a significant reduction in partial-onset seizures after 2 years in the study. In treatment of intention tremors, surface electrodes recording EMG activity have been used to create a sort of closed-loop on-demand control system for DBS that may reduce patient resistance to treatment by stimulation (Yamamoto et al., 2013).

Aborting pathological activity using feedback-controlled electrical stimulation is just one application for closed-loop control of intrinsic operations. Another application is to facilitate synaptic efficacy of specific neural connections, using the natural timing of neuronal firing between groups of neurons. This approach derives its rationale from Hebbian plasticity theory, which posits that neuronal connections are strengthened when presynaptic activity is temporally linked with post-synaptic activity. Because synaptic efficacy changes rely on precise millisecond by millisecond timing relationships, approaches to investigate closed-loop control in this context necessarily require the highest temporal resolution possible. To date, this has been achieved only with MEAs recording individual neuronal spikes. Jackson et al. (2006) showed that it is possible to modulate activity of neurons within the motor cortex based on a spike-dependent stimulation paradigm. In this model, monkeys with chronically implanted microelectrodes in two nearby populations of neurons in the motor cortex were trained on a torque-tracking task. The two populations were tuned to different trajectories. However, when one of the microelectrodes was stimulated based on the spikes recorded from the other microelectrode, the trajectory tuning became similar between the two populations. This study suggested that it is possible to alter existing cortical connections by "linking" two areas together using closed-loop stimulation. Of added interest is the fact that these changes persisted even after the closed-loop period ended, indicating that it was possible to induce long-term changes in synaptic efficacy using this paradigm.

Extending this idea to a traumatic brain injury model, Guggenmos et al. (2013) showed that it is possible to restore a reaching function in rats following damage to motor cortex by linking the premotor and somatosensory areas using activity-dependent stimulation (ADS; Guggenmos et al., 2013). In this study, a focal impact was made over the rat's caudal forelimb area in motor cortex, abolishing its ability to perform the reaching task effectively, largely due to the disruption in somatosensory motor integration. A recording microelectrode was implanted

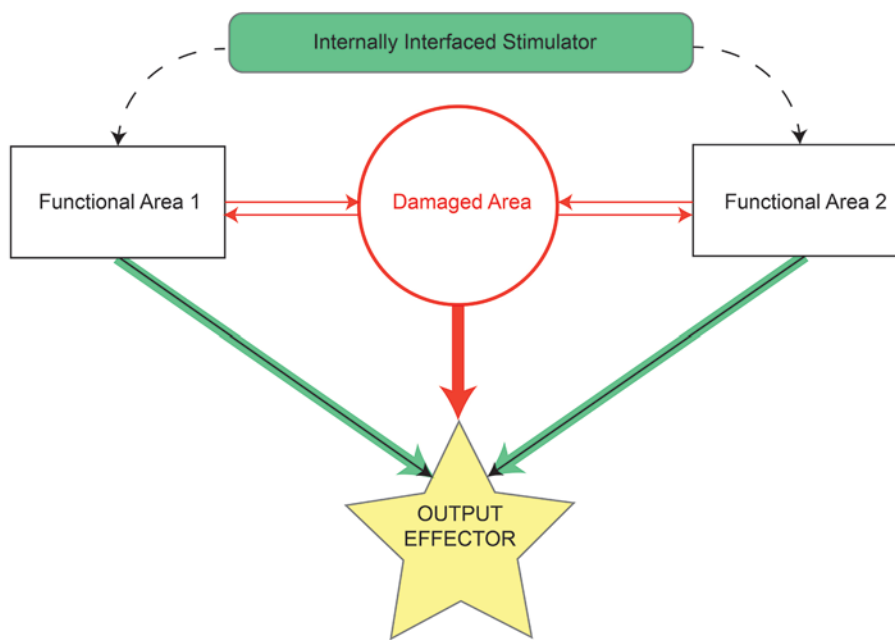


**FIGURE 3 | Schematic by which internally contained stimulation devices restore lost function resulting from damaged or missing tissue.** Before damage, the area of interest (red circle) and functionally related areas (rectangles) relay information between each other and effectors (solid arrows) of some output task (yellow star). The majority of information in controlling task output initially comes from the damaged area (thick red arrow), but may also arrive, although to a lesser extent, from functionally related areas (thin black arrows). Following injury, connections to and from the damaged area are lost (all red elements). The stimulation device serves as a direct bridge between functional areas, allowing strengthened output (thick green arrows) from those areas to the output effectors and thereby restoring some degree of lost functionality.

in the spared rostral forelimb area (RFA), which is somewhat analogous to the primate premotor area. A stimulating electrode, which was triggered by a wireless, battery-operated, head-mounted chip, was implanted in the primary somatosensory (S1) forelimb area. In the ADS paradigm, which ran continuously 24 h a day for up to 28 days, spikes detected in RFA were used to trigger stimulation in S1 after a brief delay (7.5 ms). Remarkably, rats in the ADS protocol demonstrated a significant recovery of functional reaching behavior within a few weeks of ADS treatment. In conjunction with behavioral improvement, synaptic potentiation between S1 and RFA increased as well. Recently, a version of this paradigm has been applied to the rat cervical spinal cord as well, demonstrating a possible treatment mechanism for spinal cord injury, although the trigger signal was EMG activity and not primary CNS activity (McPherson et al., 2015).

There are still a number of unanswered questions regarding the effects of ADS in the context of neuronal pathologies. For example, it is not yet known how long the effects last, or the duration of the therapeutic window. Nevertheless, such a strategy of changing synaptic efficacy is an attractive option for use in a temporary implant because it raises the possibility of a removable or degradable device that only needs to function transiently. Thus, the simplicity of use of the device would mean a one-time surgical operation for patients, with the possibility of having a degradable or removable device that could then either be left *in situ* or explanted after treatment. In addition, aside from setting the thresholds for spike detection, there are a minimum

of decoding algorithms that must be customized for individual patients, increasing the feasibility of such an approach in a clinical setting.

Other devices that control intrinsic operations have utilized a different approach. These devices restore cognitive function by replacing circuitry of the brain that is missing or malfunctioning (Berger et al., 2011, 2012; Hampson et al., 2012; Opris et al., 2012; Bonifazi et al., 2013). Berger's group demonstrated that it is possible to improve rat memory scores in a delayed non-match-to-sample task by implanting a device to translate spike trains detected in CA3 into stimulus trains in CA1 (Berger et al., 2012). Presumably, this closed-loop stimulation acts as a proxy for lost hippocampal function, modifying the spatiotemporal coding of the neural spike information in a similar way to the intact brain.

A major remaining challenge for these types of devices is that in order to increase the degree of complexity of information transmitted, it is necessary to increase the number of inputs. This problem presents a similar challenge as in the externally operating device case in that there is a density limit to the number of electrode sites that can record from a given area at a particular time. As the number of inputs increases, the computational difficulty increases as well. Put in context, a 2004 study by Izhikevich that modeled 100,000 neurons with 8.5 million connections between them took roughly 60 s of computation time for every 1 s of simulation time (Izhikevich et al., 2004). While technology has improved substantially since 2004, it is easy to imagine that as the number of neurons increases the computational difficulty will increase quickly, too. Thus, the

complexity of the cognitive task being recovered will most likely determine the feasibility of employing such techniques.

As mentioned previously, a second strategy exists when incorporating closed-loop strategies for control of intrinsic operations. These types of devices are commonly classified as “restorative” BCI, as they are primarily used in rehabilitation treatments as a means to train patients to overcome some form of impairment. While they technically do affect some element extrinsic to the patient, the goal is to cause lasting intrinsic plastic changes that remedy deficits and eventually allow the patient to no longer need the use of the BCI; thus they are classified here with the other intrinsic devices. For example, a BCI designed to reward desynchronization of particular oscillatory rhythms in stroke patients with corresponding proprioceptive feedback by movement of an orthosis demonstrated a clinically meaningful change in assessment scores of patients receiving the orthotic treatment against controls (Ramos-Murguiaday et al., 2013). This type of training BCI has been the subject of much interest in the field. One direction is the adjunctive use of non-invasive electrical stimulation with training BCI to enhance learning by amplifying the ERD signal using anodal transcranial direct current stimulation (Soekadar et al., 2014; Kasashima-Shindo et al., 2015; Soekadar et al., 2015a). Another avenue is the use of graded velocity feedback in response to the relative strength of the ERD signal to improve learning by providing improved visual and proprioceptive feedback during BCI-triggered orthotic movement (Soekadar et al., 2011). In this study, even stroke patients demonstrated improved modulation of ipsilesional activity; a similar study demonstrated evidence that this paradigm could lead to new voluntary EMG activity in hemiparetic patients (Shindo et al., 2011). There are a few case studies involving BCI for modulating intrinsic operations as well. One study used visual feedback for the control of excessive levels of beta band activity detected by EEG, providing some evidence that this paradigm could cause voluntary changes in pathological brain activity and improve handwriting for a patient suffering chronic writer’s cramps (Hashimoto et al., 2014). A within-subject withdrawal design in functional EEG BCI-driven neuromuscular electrical stimulation showed some restoration of voluntary EMG activity in a paretic patient where previous rehabilitation treatments had failed (Mukaino et al., 2014). Methods of non-invasive stimulation that could tentatively be used with some of the aforementioned strategies have been proposed, but are still in preliminary stages (Soekadar et al., 2013; Wilde et al., 2015; Zrenner et al., 2015).

### Evaluating Intrinsic Operation Efficacy

While many of the restorative closed-loop BCI devices have demonstrated substantial clinical efficacy, one common theme among closed-loop devices that do not fall under this category is that they are still farther from clinical application when compared to their externally interfaced counterparts. This may be, in part, because the underlying mechanisms of some of the internally interfaced devices are still not well understood. For example, in a device attempting to recreate the firing patterns connecting one region to another, what sort of simulated

pattern would be important to use? Or in the stimulation-dependent closed-loop system, how does the “linkage” between the two areas occur? Before the translation of these devices to a clinical setting, there remains a large amount of investigation to understand the mechanistic means by which these devices work. Even in those devices that are closer to widespread clinical implementation, the neuronal substrates for improved control and use of BCIs are not entirely understood (Soekadar et al., 2015a).

A large remaining area of study is to demonstrate specific features of how these internally interfaced devices affect changes in network connectivity. For example, a method to measure the putative changes in anatomical connectivity between two artificially linked areas would be to look at the number of projections from one area to the other in animals with and without the device post mortem; this provides a statistical means for comparison between groups, but is limited in the description of functional connectivity that may take place. Alternatively, means of visualizing connections in the brain such as diffusion tensor imaging has been used in rats *in vivo* (Laitinen et al., 2015), and could be employed for such a within-subject comparison study; however, it can be cumbersome to use such methods to map animals pre- and post- implantation. Additionally, implanted devices can obscure the accuracy of such data collection methods.

Rather than tracking changes in anatomical connectivity, it may be easier to track changes in effective connectivity directly using electrophysiological means. It is common practice to use methods such as finding the cross correlation over a sliding window to determine the average cross correlation for spike train firing in two areas in *in vitro* studies (Perkel et al., 1967). This method has also been used *in vivo* (Murphy et al., 1985), and has recently been used in conjunction with delayed mutual information to provide insight to the direction of connections as well as the specific patterns of connectivity of individual neurons (Taghva et al., 2012; Endo et al., 2015). Using statistical analyses such as cross correlation and time delayed mutual information may allow for the quantification of these effective changes over time in BCI models.

Eventually, these methods could pinpoint the time scale over which permanent changes take place, or help to identify other parameters necessary for the optimization of such devices. For example, for the closed-loop system used by Guggenmos et al. (2013) to be generalized to multiple areas of the brain, it will be necessary to test whether the delay between trigger and stimulation is a general property of ADS, or if other factors such as distance and intrinsic connectivity between areas plays a role as well. In order to test different delay times and how well they change the effective connectivity between areas, having a good metric to describe and compare changes will be critical.

## CONCLUSION

An ideal high fidelity BCI would both sample and allow stimulation of precise neural features non-invasively. In reality, such a combination is unlikely. Nonetheless, current work across several types of BCIs provides promising results for the clinical

applicability of these technologies. Despite the positive outlook for the future of BCIs, several challenges remain before high fidelity recording and stimulating devices are made available for common clinical use. For MEA recordings, two major challenges remain. The first is to improve the patency of chronically implanted microelectrodes so that they can continue to be used for recordings for the duration of the patient's lifespan. The second challenge is to find reliable recording sites and decoding algorithms that do not need to be recalibrated on a daily or weekly basis, and adaptive decoders that would allow for automatic recalibration as patients learn to use implanted BCIs more efficiently.

For ECoG and EEG, the challenge is less from a materials perspective, and more from a computational perspective. The primary goal remains similar to MEA-based BCIs: it is most important to find regions from which task-related information can be reliably decoded and translated into repeatable intent. It may first be necessary to find a means to identify reliable neural substrates for BCI learning using MEAs, then demonstrate that the activity patterns of these substrates can be reliably decoded using less invasive measures. Emerging methods incorporating structural and metabolic information into current source estimates may provide the additional information necessary to increase decoding accuracy (Aihara et al., 2012). Additionally, as frequency-domain based decoders improve in accuracy, it will be important to continue to incorporate signals with greater numbers of independent features into BCI decoders in order to improve the ease of adaptation for implanted patients. In ECoG, this could potentially be improved by optimizing location and spacing.

In terms of decoded output, goal-tuned single units in MEA-based BCIs have shown great promise for decoding intent in complex movements. Meanwhile, work involving less-invasive approaches such as ECoG and EEG continues to improve in decoding accuracy. The future combination of these lines of work will be critical for progress towards increased clinical use of neural prosthetics. In order to demonstrate the complete neural electrophysiological basis for learned BCI behavior, elements from all types of recording paradigms may be necessary. Such an understanding may lead to new therapeutic targets for BCI devices.

As non-invasive electrical stimulation becomes a more realistic possibility in restorative devices that use overt, extrinsic goals for patient rehabilitation, combination stimulation

approaches may increase the utility and effectiveness of BCIs. Devices controlling intrinsic operations, which offer a more subtle form of closed-loop stimulation, face a different set of challenges going forward. The primary challenge will be to find a way to generalize their use to many parts of the CNS. Whether that is finding the optimal delay for ADS between two areas, or finding the right recorded or computed pattern of neural stimulation to recreate lost functionality, the challenges facing internally interfaced devices are also numerous.

Thus, the current state of progress in implementing a high fidelity BCI depends on the type of device. Restorative closed-loop devices for rehabilitation therapy have already demonstrated some clinical effect in paretic patients (Ramos-Murguialday et al., 2013), but are limited to treatment of patient populations that retain spared neural pathways following injury. Devices that control extrinsic operations have attained clinical use in the sense that they have been implemented in limited human trials (Hochberg et al., 2012; Aflalo et al., 2015). However, the practicality of such devices for widespread use remains questionable until such time that costs are reduced and devices made more widely available. In addition, decoders must be made generalizable and receive more accurate input from a higher density of sources. Completely intrinsic closed-loop devices offer tantalizing possibilities due to the possibility of not only use in motor recovery (Guggenmos et al., 2013; McPherson et al., 2015), but potentially cognitive therapy as well (Berger et al., 2012). Still, many important questions remain unanswered about these devices. Can they show reliability in animal models at a large scale? How long must such a therapeutic device remain in effect before clinical results are demonstrated? Thus, each type of device has its potential benefits and drawbacks, but importantly, an abundance of paths remain toward a future where BCIs are commonplace in a variety of clinical settings.

## FUNDING

This work was made possible by a generous gift from the Robert D. Deffenbaugh Foundation as well as by support from Department of Defense Congressionally Directed Medical Research Program (grant no. PT090167P1), National Institute of Neurological Disorders and Stroke/NIH (grant no. R37 NS30853), and the Kansas Training Program in Neurological and Rehabilitation Sciences (grant no. NIH 5 T32 HD 57850).

## REFERENCES

- Aflalo, T., Kellis, S., Klaes, C., Lee, B., Shi, Y., Pejsa, K., et al. (2015). Neurophysiology. Decoding motor imagery from the posterior parietal cortex of a tetraplegic human. *Science* 348, 906–910. doi: 10.1126/science.aaa5417
- Aihara, T., Takeda, Y., Takeda, K., Yasuda, W., Sato, T., Otaka, Y., et al. (2012). Cortical current source estimation from electroencephalography in combination with near-infrared spectroscopy as a hierarchical prior. *Neuroimage* 59, 4006–4021. doi: 10.1016/j.neuroimage.2011.09.087
- Ajiboye, A. B., Simeral, J. D., Donoghue, J. P., Hochberg, L. R., and Kirsch, R. F. (2012). Prediction of imagined single-joint movements in a person with high-level tetraplegia. *IEEE Trans. Biomed. Eng.* 59, 2755–2765. doi: 10.1109/tbme.2012.2209882
- Bajaj, S., Butler, A. J., Drake, D., and Dhamala, M. (2015). Functional organization and restoration of the brain motor-execution network after stroke and rehabilitation. *Front. Hum. Neurosci.* 9:173. doi: 10.3389/fnhum.2015.00173
- Bensch, M., Karim, A. A., Mellinger, J., Hinterberger, T., Tangermann, M., Bogdan, M., et al. (2007). Nessi: an EEG-controlled web browser for severely paralyzed patients. *Comput. Intell. Neurosci.* 2007:71863. doi: 10.1155/2007/71863
- Berger, T. W., Hampson, R. E., Song, D., Goonawardena, A., Marmarelis, V. Z., and Deadwyler, S. A. (2011). A cortical neural prosthesis for restoring and enhancing memory. *J. Neural Eng.* 8:046017. doi: 10.1088/1741-2560/8/4/046017

Berger, T. W., Song, D., Chan, R. H., Marmarelis, V. Z., Lacoss, J., Wills, J., et al. (2012). A hippocampal cognitive prosthesis: multi-input, multi-output nonlinear modeling and VLSI implementation. *IEEE Trans. Neural Syst. Rehabil. Eng.* 20, 198–211. doi: 10.1109/TNSRE.2012.2189133

Birbaumer, N., Ghanayim, N., Hinterberger, T., Iversen, I., Kotchoubey, B., Kübler, A., et al. (1999). A spelling device for the paralysed. *Nature* 398, 297–298. doi: 10.1038/18581

Blankertz, B., Müller, K. R., Curio, G., Vaughan, T. M., Schalk, G., Wolpaw, J. R., et al. (2004). The BCI competition 2003: progress and perspectives in detection and discrimination of EEG single trials. *IEEE Trans. Biomed. Eng.* 51, 1044–1051. doi: 10.1109/tbme.2004.826692

Bleichner, M. G., Freudenburg, Z. V., Jansma, J. M., Aarnoutse, E. J., Vansteensel, M. J., and Ramsey, N. F. (2014). Give me a sign: decoding four complex hand gestures based on high-density ECoG. *Brain Struct. Funct.* doi: 10.1007/s00429-014-0902-x [Epub ahead of print].

Bonifazi, P., Difato, F., Massobrio, P., Breschi, G. L., Pasquale, V., Levi, T., et al. (2013). *In vitro* large-scale experimental and theoretical studies for the realization of bi-directional brain-prostheses. *Front. Neural Circuits* 7:40. doi: 10.3389/fncir.2013.00040

Bouchard, K. E., and Chang, E. F. (2014). Neural decoding of spoken vowels from human sensory-motor cortex with high-density electrocorticography. *Conf. Proc. IEEE Eng. Med. Biol. Soc.* 2014, 6782–6785. doi: 10.1109/EMBC.2014.6945185

Bulea, T. C., Prasad, S., Kilicarslan, A., and Contreras-Vidal, J. L. (2014). Sitting and standing intention can be decoded from scalp EEG recorded prior to movement execution. *Front. Neurosci.* 8:376. doi: 10.3389/fnins.2014.00376

Carmena, J. M., Lebedev, M. A., Crist, R. E., O'Doherty, J. E., Santucci, D. M., Dimitrov, D. F., et al. (2003). Learning to control a brain-machine interface for reaching and grasping by primates. *PLoS Biol.* 1:E42. doi: 10.1371/journal.pbio.0000042

Chao, Z. C., Nagasaka, Y., and Fujii, N. (2010). Long-term asynchronous decoding of arm motion using electrocorticographic signals in monkeys. *Front. Neuroeng.* 3:3. doi: 10.3389/fneng.2010.00003

Chestek, C. A., Gilja, V., Blabe, C. H., Foster, B. L., Shenoy, K. V., Parvizi, J., et al. (2013). Hand posture classification using electrocorticography signals in the gamma band over human sensorimotor brain areas. *J. Neural Eng.* 10:026002. doi: 10.1088/1741-2560/10/2/026002

Collinger, J. L., Wodlinger, B., Downey, J. E., Wang, W., Tyler-Kabara, E. C., Weber, D. J., et al. (2013). High-performance neuroprosthetic control by an individual with tetraplegia. *Lancet* 381, 557–564. doi: 10.1016/S0140-6736(12)61816-9

Cooper, R., Winter, A. L., Crow, H. J., and Walter, W. G. (1965). Comparison of subcortical, cortical and scalp activity using chronically indwelling electrodes in man. *Electroencephalogr. Clin. Neurophysiol.* 18, 217–228. doi: 10.1016/0013-4694(65)90088-x

Cunningham, J. P., Nuyujukian, P., Gilja, V., Ryu, S. I., and Shenoy, K. V. (2009). Methods for estimating neural firing rates and their application to brain-machine interfaces. *Neural Netw.* 22, 1235–1246. doi: 10.1016/j.neunet.2009.02.004

Cunningham, J. P., Nuyujukian, P., Gilja, V., Chestek, C. A., Ryu, S. I., and Shenoy, K. V. (2011). A closed-loop human simulator for investigating the role of feedback control in brain-machine interfaces. *J. Neurophysiol.* 105, 1932–1949. doi: 10.1152/jn.00503.2010

De Faveri, S., Maggiolini, E., Miele, E., De Angelis, F., Cesca, F., Benfenati, F., et al. (2014). Bio-inspired hybrid microelectrodes: a hybrid solution to improve long-term performance of chronic intracortical implants. *Front. Neuroeng.* 7:7. doi: 10.3389/fneng.2014.00007

Donoghue, J. P., and Parham, C. (1983). Afferent connections of the lateral agranular field of the rat motor cortex. *J. Comp. Neurol.* 217, 390–404. doi: 10.1002/cne.902170404

Endo, W., Santos, F. P., Simpson, D., Maciel, C. D., and Newland, P. L. (2015). Delayed mutual information infers patterns of synaptic connectivity in a proprioceptive neural network. *J. Comput. Neurosci.* 38, 427–438. doi: 10.1007/s10827-015-0548-6

Ersen, A., Elkabes, S., Freedman, D. S., and Sahin, M. (2015). Chronic tissue response to untethered microelectrode implants in the rat brain and spinal cord. *J. Neural Eng.* 12:016019. doi: 10.1088/1741-2560/12/1/016019

Ethier, C., Oby, E. R., Bauman, M. J., and Miller, L. E. (2012). Restoration of grasp following paralysis through brain-controlled stimulation of muscles. *Nature* 485, 368–371. doi: 10.1038/nature10987

Evarts, E. V. (1966). Pyramidal tract activity associated with a conditioned hand movement in the monkey. *J. Neurophysiol.* 29, 1011–1027.

Felix, S. H., Shah, K. G., Tolosa, V. M., Sheth, H. J., Tooker, A. C., Delima, T. L., et al. (2013). Insertion of flexible neural probes using rigid stiffeners attached with biodegradable adhesive. *J. Vis. Exp.* 79:e50609. doi: 10.3791/50609

Felton, E. A., Wilson, J. A., Williams, J. C., and Garell, P. C. (2007). Electrocorticographically controlled brain-computer interfaces using motor and sensory imagery in patients with temporary subdural electrode implants. Report of four cases. *J. Neurosurg.* 106, 495–500. doi: 10.3171/jns.2007.106.3.495

Fetz, E. E. (1969). Operant conditioning of cortical unit activity. *Science* 163, 955–958. doi: 10.1126/science.163.3870.955

Flint, R. D., Lindberg, E. W., Jordan, L. R., Miller, L. E., and Slutsky, M. W. (2012). Accurate decoding of reaching movements from field potentials in the absence of spikes. *J. Neural Eng.* 9:046006. doi: 10.1088/1741-2560/9/4/046006

Flint, R. D., Wang, P. T., Wright, Z. A., King, C. E., Krucoff, M. O., Schuele, S. U., et al. (2014). Extracting kinetic information from human motor cortical signals. *Neuroimage* 101, 695–703. doi: 10.1016/j.neuroimage.2014.07.049

Flint, R. D., Wright, Z. A., Scheid, M. R., and Slutsky, M. W. (2013). Long term, stable brain machine interface performance using local field potentials and multiunit spikes. *J. Neural Eng.* 10:056005. doi: 10.1088/1741-2560/10/5/056005

Gavins, F. N., and Smith, H. K. (2015). Cell tracking technologies for acute ischemic brain injury. *J. Cereb. Blood Flow Metab.* 35, 1090–1099. doi: 10.1038/jcbfm.2015.93

Georgopoulos, A. P., Schwartz, A. B., and Kettner, R. E. (1986). Neuronal population coding of movement direction. *Science* 233, 1416–1419. doi: 10.1126/science.3749885

Grimaldi, G., Manto, M., and Jdaoudi, Y. (2013). Quality parameters for a multimodal EEG/EMG/kinematic brain-computer interface (BCI) aiming to suppress neurological tremor in upper limbs. *F1000Res.* 2:282. doi: 10.12688/f1000research.2-282.v2

Guggenmos, D. J., Azin, M., Barbay, S., Mahnken, J. D., Dunham, C., Mohseni, P., et al. (2013). Restoration of function after brain damage using a neural prosthesis. *Proc. Natl. Acad. Sci. U S A* 110, 21177–21182. doi: 10.1073/pnas.1316885110

Hall, T. M., Nazarpour, K., and Jackson, A. (2014). Real-time estimation and biofeedback of single-neuron firing rates using local field potentials. *Nat. Commun.* 5:5462. doi: 10.1038/ncomms6462

Hampson, R. E., Gerhardt, G. A., Marmarelis, V., Song, D., Opris, I., Santos, L., et al. (2012). Facilitation and restoration of cognitive function in primate prefrontal cortex by a neuromprosthesis that utilizes minicolumn-specific neural firing. *J. Neural Eng.* 9:056012. doi: 10.1088/1741-2560/9/5/056012

Hashimoto, Y., Ota, T., Mukaino, M., Liu, M., and Ushiba, J. (2014). Functional recovery from chronic writer's cramp by brain-computer interface rehabilitation: a case report. *BMC Neurosci.* 15:103. doi: 10.1186/1471-2202-15-103

Heck, C. N., King-Stephens, D., Massey, A. D., Nair, D. R., Jobst, B. C., Barkley, G. L., et al. (2014). Two-year seizure reduction in adults with medically intractable partial onset epilepsy treated with responsive neurostimulation: final results of the RNS system pivotal trial. *Epilepsia* 55, 432–441. doi: 10.1111/epi.12534

Hochberg, L. R., Bacher, D., Jarosiewicz, B., Masse, N. Y., Simeral, J. D., Vogel, J., et al. (2012). Reach and grasp by people with tetraplegia using a neurally controlled robotic arm. *Nature* 485, 372–375. doi: 10.1038/nature11076

Hochberg, L. R., Serruya, M. D., Friehs, G. M., Mukand, J. A., Saleh, M., Caplan, A. H., et al. (2006). Neuronal ensemble control of prosthetic devices by a human with tetraplegia. *Nature* 442, 164–171. doi: 10.1038/nature04970

Holz, E. M., Botrel, L., Kaufmann, T., and Kübler, A. (2015). Long-term independent brain-computer interface home use improves quality of life of a patient in the locked-in state: a case study. *Arch. Phys. Med. Rehabil.* 96, S16–S26. doi: 10.1016/j.apmr.2014.03.035

Hosseini, S. M., Farahmandnia, M., Razi, Z., Delavari, S., Shakibajahromi, B., Sarvestani, F. S., et al. (2015). Combination cell therapy with mesenchymal stem cells and neural stem cells for brain stroke in rats. *Int. J. Stem Cells* 8, 99–105. doi: 10.15283/ijsc.2015.8.1.99

Izhikevich, E. M., Gally, J. A., and Edelman, G. M. (2004). Spike-timing dynamics of neuronal groups. *Cereb. Cortex* 14, 933–944. doi: 10.1093/cercor/bhh053

Jackson, A., Mavoori, J., and Fetz, E. E. (2006). Long-term motor cortex plasticity induced by an electronic neural implant. *Nature* 444, 56–60. doi: 10.1038/nature05226

Kasashima-Shindo, Y., Fujiwara, T., Ushiba, J., Matsushika, Y., Kamatani, D., Oto, M., et al. (2015). Brain-computer interface training combined with transcranial direct current stimulation in patients with chronic severe hemiparesis: proof of concept study. *J. Rehabil. Med.* 47, 318–324. doi: 10.2340/16501977-1925

Kellis, S., Hanrahan, S., Davis, T., House, P. A., Brown, R., and Greger, B. (2012). Decoding hand trajectories from micro-electrocorticography in human patients. *Conf. Proc. IEEE Eng. Med. Biol. Soc.* 2012, 4091–4094. doi: 10.1109/EMBC.2012.6346866

King-Stephens, D., Mirro, E., Weber, P. B., Laxer, K. D., Van Ness, P. C., Salanova, V., et al. (2015). Lateralization of mesial temporal lobe epilepsy with chronic ambulatory electrocorticography. *Epilepsia* 56, 959–967. doi: 10.1111/epi.13010

Laitinen, T., Sierra, A., Bolkvadze, T., Pitkänen, A., and Gröhn, O. (2015). Diffusion tensor imaging detects chronic microstructural changes in white and gray matter after traumatic brain injury in rat. *Front. Neurosci.* 9:128. doi: 10.3389/fnins.2015.00128

Leuthardt, E. C., Schalk, G., Roland, J., Rouse, A., and Moran, D. W. (2009). Evolution of brain-computer interfaces: going beyond classic motor physiology. *Neurosurg. Focus* 27:E4. doi: 10.3171/2009.4.FOCUS0979

Leuthardt, E. C., Schalk, G., Wolpaw, J. R., Ojemann, J. G., and Moran, D. W. (2004). A brain-computer interface using electrocorticographic signals in humans. *J. Neural Eng.* 1, 63–71. doi: 10.1088/1741-2560/1/2/001

Little, S., Pogosyan, A., Neal, S., Zavala, B., Zrinzo, L., Hariz, M., et al. (2013). Adaptive deep brain stimulation in advanced Parkinson disease. *Ann. Neurol.* 74, 449–457. doi: 10.1002/ana.23951

Marathe, A. R., and Taylor, D. M. (2013). Decoding continuous limb movements from high-density epidural electrode arrays using custom spatial filters. *J. Neural Eng.* 10:036015. doi: 10.1088/1741-2560/10/3/036015

McCarthy, P. T., Otto, K. J., and Rao, M. P. (2011). Robust penetrating microelectrodes for neural interfaces realized by titanium micromachining. *Biomed. Microdevices* 13, 503–515. doi: 10.1007/s10544-011-9519-5

McFarland, D. J., Sarnacki, W. A., and Wolpaw, J. R. (2010). Electroencephalographic (EEG) control of three-dimensional movement. *J. Neural Eng.* 7:036007. doi: 10.1088/1741-2560/7/3/036007

McPherson, J. G., Miller, R. R., and Perlmuter, S. I. (2015). Targeted, activity-dependent spinal stimulation produces long-lasting motor recovery in chronic cervical spinal cord injury. *Proc. Natl. Acad. Sci. U S A* 112, 12193–12198. doi: 10.1073/pnas.1505383112

Michel, C. M., Murray, M. M., Lantz, G., Gonzalez, S., Spinelli, L., and Grave de Peralta, R. (2004). EEG source imaging. *Clin. Neurophysiol.* 115, 2195–2222. doi: 10.1016/j.clinph.2004.06.001

Mukaino, M., Ono, T., Shindo, K., Fujiwara, T., Ota, T., Kimura, A., et al. (2014). Efficacy of brain-computer interface-driven neuromuscular electrical stimulation for chronic paresis after stroke. *J. Rehabil. Med.* 46, 378–382. doi: 10.2340/16501977-1785

Murphy, J., Kwan, H., and Wong, Y. (1985). Cross correlation studies in primate motor cortex: synaptic interaction and shared input. *Can. J. Neurol. Sci.* 12, 11–23.

Nakanishi, Y., Yanagisawa, T., Shin, D., Fukuma, R., Chen, C., Kambara, H., et al. (2013). Prediction of three-dimensional arm trajectories based on ECoG signals recorded from human sensorimotor cortex. *PLoS One* 8:e72085. doi: 10.1371/journal.pone.0072085

Nudo, R. J., and Friel, K. M. (1999). Cortical plasticity after stroke: implications for rehabilitation. *Rev. Neurol. (Paris)* 155, 713–717.

Nudo, R. J., Milliken, G. W., Jenkins, W. M., and Merzenich, M. M. (1996). Use-dependent alterations of movement representations in primary motor cortex of adult squirrel monkeys. *J. Neurosci.* 16, 785–807.

Nuyujukian, P., Kao, J. C., Fan, J. M., Stavisky, S. D., Ryu, S. I., and Shenoy, K. V. (2014). Performance sustaining intracortical neural prostheses. *J. Neural Eng.* 11:066003. doi: 10.1088/1741-2560/11/6/066003

Obien, M. E., Deligkaris, K., Bullmann, T., Bakum, D. J., and Frey, U. (2015). Revealing neuronal function through microelectrode array recordings. *Front. Neurosci.* 8:423. doi: 10.3389/fnins.2014.00423

Opriš, I., Fuqua, J. L., Huettl, P. F., Gerhardt, G. A., Berger, T. W., Hampson, R. E., et al. (2012). Closing the loop in primate prefrontal cortex: inter-laminar processing. *Front. Neural Circuits* 6:88. doi: 10.3389/fncir.2012.00088

Orsborn, A. L., Moorman, H. G., Overduin, S. A., Shanechi, M. M., Dimitrov, D. F., and Carmena, J. M. (2014). Closed-loop decoder adaptation shapes neural plasticity for skillful neuroprosthetic control. *Neuron* 82, 1380–1393. doi: 10.1016/j.neuron.2014.04.048

Pazienti, A., and Grün, S. (2006). Robustness of the significance of spike synchrony with respect to sorting errors. *J. Comput. Neurosci.* 21, 329–342. doi: 10.1007/s10827-006-8899-7

Peng, Z., Xuan, M., Hailong, H., and Jiping, H. (2014). Predicting hand orientation in reach-to-grasp tasks using neural activities from primary motor cortex. *Conf. Proc. IEEE Eng. Med. Biol. Soc.* 2014, 1306–1309. doi: 10.1109/EMBC.2014.6943838

Perge, J. A., Homer, M. L., Malik, W. Q., Cash, S., Eskandar, E., Friehs, G., et al. (2013). Intra-day signal instabilities affect decoding performance in an intracortical neural interface system. *J. Neural Eng.* 10:036004. doi: 10.1088/1741-2560/10/3/036004

Perkel, D. H., Gerstein, G. L., and Moore, G. P. (1967). Neuronal spike trains and stochastic point processes. II. Simultaneous spike trains. *Biophys. J.* 7, 419–440. doi: 10.1016/s0006-3495(67)86597-4

Pfurtscheller, G., and Cooper, R. (1975). Frequency dependence of the transmission of the EEG from cortex to scalp. *Electroencephalogr. Clin. Neurophysiol.* 38, 93–96. doi: 10.1016/0013-4694(75)90215-1

Pfurtscheller, G., Müller, G. R., Pfurtscheller, J., Gerner, H. J., and Rupp, R. (2003). ‘Thought’-control of functional electrical stimulation to restore hand grasp in a patient with tetraplegia. *Neurosci. Lett.* 351, 33–36. doi: 10.1016/s0304-3940(03)00947-9

Pfurtscheller, G., Neuper, C., Flotzinger, D., and Pregenzer, M. (1997). EEG-based discrimination between imagination of right and left hand movement. *Electroencephalogr. Clin. Neurophysiol.* 103, 642–651. doi: 10.1016/s0013-4694(97)00080-1

Pistohl, T., Ball, T., Schulze-Bonhage, A., Aertsen, A., and Mehring, C. (2008). Prediction of arm movement trajectories from ECoG-recordings in humans. *J. Neurosci. Methods* 167, 105–114. doi: 10.1016/j.jneumeth.2007.10.001

Popović Maneski, L., Jorgovanović, N., Ilić, V., Doseň, S., Keller, T., Popović, M. B., et al. (2011). Electrical stimulation for the suppression of pathological tremor. *Med. Biol. Eng. Comput.* 49, 1187–1193. doi: 10.1007/s11517-011-0803-6

Ramos-Murguialday, A., and Birbaumer, N. (2015). Brain oscillatory signatures of motor tasks. *J. Neurophysiol.* 113, 3663–3682. doi: 10.1152/jn.00467.2013

Ramos-Murguialday, A., Broetz, D., Rea, M., Läer, L., Yilmaz, O., Brasil, F. L., et al. (2013). Brain-machine interface in chronic stroke rehabilitation: a controlled study. *Ann. Neurol.* 74, 100–108. doi: 10.1002/ana.23879

Reddy, C. G., Reddy, G. G., Kawasaki, H., Oya, H., Miller, L. E., and Howard, M. A. 3rd (2009). Decoding movement-related cortical potentials from electrocorticography. *Neurosurg. Focus* 27:E11. doi: 10.3171/2009.4.FOCUS0990

Rey, H. G., Pedreira, C., and Quian Quiroga, R. (2015). Past, present and future of spike sorting techniques. *Brain Res. Bull.* 119(Pt. B), 106–117. doi: 10.1016/j.brainresbull.2015.04.007

Rousche, P. J., and Normann, R. A. (1999). Chronic intracortical microstimulation (ICMS) of cat sensory cortex using the Utah intracortical electrode array. *IEEE Trans. Rehabil. Eng.* 7, 56–68. doi: 10.1109/86.750552

Rouse, A. G., Williams, J. J., Wheeler, J. J., and Moran, D. W. (2013). Cortical adaptation to a chronic micro-electrocorticographic brain computer interface. *J. Neurosci.* 33, 1326–1330. doi: 10.1523/JNEUROSCI.0271-12.2013

Sanchez, J. C., Gunduz, A., Carney, P. R., and Principe, J. C. (2008). Extraction and localization of mesoscopic motor control signals for human ECoG neuroprosthetics. *J. Neurosci. Methods* 167, 63–81. doi: 10.1016/j.jneumeth.2007.04.019

Schalk, G., Kubánek, J., Miller, K. J., Anderson, N. R., Leuthardt, E. C., Ojemann, J. G., et al. (2007). Decoding two-dimensional movement trajectories using electrocorticographic signals in humans. *J. Neural Eng.* 4, 264–275. doi: 10.1088/1741-2560/4/3/012

Schalk, G., Miller, K. J., Anderson, N. R., Wilson, J. A., Smyth, M. D., Ojemann, J. G., et al. (2008). Two-dimensional movement control using electrocorticographic signals in humans. *J. Neural Eng.* 5, 75–84. doi: 10.1088/1741-2560/5/1/008

Sharma, A., Sane, H., Kulkarni, P., Yadav, J., Gokulchandran, N., Biju, H., et al. (2015). Cell therapy attempted as a novel approach for chronic traumatic

brain injury—a pilot study. *Springerplus* 4:26. doi: 10.1186/s40064-015-0794-0

Shindo, K., Kawashima, K., Ushiba, J., Ota, N., Ito, M., Ota, T., et al. (2011). Effects of neurofeedback training with an electroencephalogram-based brain-computer interface for hand paralysis in patients with chronic stroke: a preliminary case series study. *J. Rehabil. Med.* 43, 951–957. doi: 10.2340/16501977-0859

Slutzky, M. W., Jordan, L. R., Lindberg, E. W., Lindsay, K. E., and Miller, L. E. (2011). Decoding the rat forelimb movement direction from epidural and intracortical field potentials. *J. Neural Eng.* 8:036013. doi: 10.1088/1741-2560/8/3/036013

Soekadar, S. R., Witkowski, M., Birbaumer, N., and Cohen, L. G. (2015a). Enhancing Hebbian learning to control brain oscillatory activity. *Cereb. Cortex* 25, 2409–2415. doi: 10.1093/cercor/blu043

Soekadar, S. R., Witkowski, M., Vitiello, N., and Birbaumer, N. (2015b). An EEG/EOG-based hybrid brain-neural computer interaction (BCNI) system to control an exoskeleton for the paralyzed hand. *Biomed. Tech. (Berl.)* 60, 199–205. doi: 10.1515/bmt-2014-0126

Soekadar, S. R., Witkowski, M., Garcia Cossio, E., Birbaumer, N., and Cohen, L. (2014). Learned EEG-based regulation of motor-related brain oscillations during application of transcranial electric currents: feasibility and limitations. *Front. Behav. Neurosci.* 8:93. doi: 10.3389/fnbeh.2014.00093

Soekadar, S. R., Witkowski, M., Mellinger, J., Ramos, A., Birbaumer, N., and Cohen, L. G. (2011). ERD-based online brain-machine interfaces (BMI) in the context of neurorehabilitation: optimizing BMI learning and performance. *IEEE Trans. Neural Syst. Rehabil. Eng.* 19, 542–549. doi: 10.1109/TNSRE.2011.2166809

Soekadar, S. R., Witkowski, M., Robinson, S. E., and Birbaumer, N. (2013). Combining electric brain stimulation and source-based brain-machine interface (BMI) training in neurorehabilitation of chronic stroke. *J. Neurol. Sci.* 333:e542. doi: 10.1016/j.jns.2013.07.1906

Sullivan, R., Duncan, K., Dailey, T., Kaneko, Y., Tajiri, N., and Borlongan, C. V. (2015). A possible new focus for stroke treatment—migrating stem cells. *Expert Opin. Biol. Ther.* 15, 949–958. doi: 10.1517/14712598.2015.1043264

Taghva, A., Song, D., Hampson, R. E., Deadwyler, S. A., and Berger, T. W. (2012). Determination of relevant neuron-neuron connections for neural prosthetics using time-delayed mutual information: tutorial and preliminary results. *World Neurosurg.* 78, 618–630. doi: 10.1016/j.wneu.2011.09.002

Taylor, D. M., Tillery, S. I., and Schwartz, A. B. (2002). Direct cortical control of 3D neuroprosthetic devices. *Science* 296, 1829–1832. doi: 10.1126/science.1070291

Todorova, S., Sadtler, P., Batista, A., Chase, S., and Ventura, V. (2014). To sort or not to sort: the impact of spike-sorting on neural decoding performance. *J. Neural Eng.* 11:056005. doi: 10.1088/1741-2560/11/5/056005

Tooker, A., Tolosa, V., Shah, K. G., Sheth, H., Felix, S., Delima, T., et al. (2012). Polymer neural interface with dual-sided electrodes for neural stimulation and recording. *Conf. Proc. IEEE Eng. Med. Biol. Soc.* 2012, 5999–6002. doi: 10.1109/EMBC.2012.6347361

Velliste, M., Perel, S., Spalding, M. C., Whitford, A. S., and Schwartz, A. B. (2008). Cortical control of a prosthetic arm for self-feeding. *Nature* 453, 1098–1101. doi: 10.1038/nature06996

Wang, W., Collinger, J. L., Degenhart, A. D., Tyler-Kabara, E. C., Schwartz, A. B., Moran, D. W., et al. (2013). An electrocorticographic brain interface in an individual with tetraplegia. *PLoS One* 8:e55344. doi: 10.1371/journal.pone.0055344

Wang, Z., Gunduz, A., Brunner, P., Ritaccio, A. L., Ji, Q., and Schalk, G. (2012). Decoding onset and direction of movements using electrocorticographic (ECOG) signals in humans. *Front. Neuroeng.* 5:15. doi: 10.3389/fneng.2012.00015

Ward, M. P., Rajdev, P., Ellison, C., and Irazoqui, P. P. (2009). Toward a comparison of microelectrodes for acute and chronic recordings. *Brain Res.* 1282, 183–200. doi: 10.1016/j.brainres.2009.05.052

Warnecke, J., Devine, N., and Olen, C. (2015). Inpatient physical therapy rehabilitation provided for a patient with complete vision loss following a traumatic brain injury. *Brain Inj.* 29, 993–999. doi: 10.3109/02699052.2015.1022877

Wessberg, J., Stambaugh, C. R., Krlik, J. D., Beck, P. D., Laubach, M., Chapin, J. K., et al. (2000). Real-time prediction of hand trajectory by ensembles of cortical neurons in primates. *Nature* 408, 361–365. doi: 10.1038/35042582

Wilde, C., Bruder, R., Binder, S., Marshall, L., and Schweikard, A. (2015). Closed-loop transcranial alternating current stimulation of slow oscillations. *Curr. Dir. Biomed. Eng.* 1, 85–88. doi: 10.1515/cdbme-2015-0022

Willett, F. R., Suminski, A. J., Fagg, A. H., and Hatsopoulos, N. G. (2013). Improving brain-machine interface performance by decoding intended future movements. *J. Neural Eng.* 10:026011. doi: 10.1088/1741-2560/10/2/026011

Williams, J. C., Hippenstein, J. A., Dilgen, J., Shain, W., and Kipke, D. R. (2007). Complex impedance spectroscopy for monitoring tissue responses to inserted neural implants. *J. Neural Eng.* 4, 410–423. doi: 10.1088/1741-2560/4/4/007

Wilson, J. A., Felton, E. A., Garell, P. C., Schalk, G., and Williams, J. C. (2006). ECoG factors underlying multimodal control of a brain-computer interface. *IEEE Trans. Neural Syst. Rehabil. Eng.* 14, 246–250. doi: 10.1109/tnsre.2006.875570

Wolpaw, J. R., and McFarland, D. J. (2004). Control of a two-dimensional movement signal by a noninvasive brain-computer interface in humans. *Proc. Natl. Acad. Sci. U S A* 101, 17849–17854. doi: 10.1073/pnas.0403504101

Wolpaw, J. R., McFarland, D. J., Neat, G. W., and Forneris, C. A. (1991). An EEG-based brain-computer interface for cursor control. *Electroencephalogr. Clin. Neurophysiol.* 78, 252–259. doi: 10.1016/0013-4694(91)90040-b

Wu, W., Shaikhouni, A., Donoghue, J. P., and Black, M. J. (2004). Closed-loop neural control of cursor motion using a Kalman filter. *Conf. Proc. IEEE Eng. Med. Biol. Soc.* 6, 4126–4129. doi: 10.1109/emb.2004.1404151

Yamamoto, T., Katayama, Y., Ushiba, J., Yoshino, H., Obuchi, T., Kobayashi, K., et al. (2013). On-demand control system for deep brain stimulation for treatment of intention tremor. *Neuromodulation* 16, 230–235; discussion 235. doi: 10.1111/j.1525-1403.2012.00521.x

Yanagisawa, T., Hirata, M., Saitoh, Y., Goto, T., Kishima, H., Fukuma, R., et al. (2011). Real-time control of a prosthetic hand using human electrocorticography signals. *J. Neurosurg.* 114, 1715–1722. doi: 10.3171/2011.1.JNS101421

Yanagisawa, T., Hirata, M., Saitoh, Y., Kato, A., Shibuya, D., Kamitani, Y., et al. (2009). Neural decoding using gyral and intrasulcal electrocorticograms. *Neuroimage* 45, 1099–1106. doi: 10.1016/j.neuroimage.2008.12.069

Yoshimura, N., Dasalla, C. S., Hanakawa, T., Sato, M. A., and Koike, Y. (2012). Reconstruction of flexor and extensor muscle activities from electroencephalography cortical currents. *Neuroimage* 59, 1324–1337. doi: 10.1016/j.neuroimage.2011.08.029

Zhang, Z. W., and Deschenes, M. (1998). Projections to layer VI of the posteromedial barrel field in the rat: a reappraisal of the role of corticothalamic pathways. *Cereb. Cortex* 8, 428–436. doi: 10.1093/cercor/8.5.428

Zrenner, C., Tünnerhoff, J., Zipser, C., Müller-Dahlhaus, F., and Ziemann, U. (2015). V38. Brain-state dependent non-invasive brain stimulation using closed-loop real-time EEG signal analysis to trigger a TMS pulse with millisecond accuracy. *Clin. Neurophysiol.* 126:e85. doi: 10.1016/j.clinph.2015.04.116

**Conflict of Interest Statement:** The authors declare that the research was conducted in the absence of any commercial or financial relationships that could be construed as a potential conflict of interest.

Randolph J. Nudo is co-founder and interim CEO of NeuraLink Technologies, LLC.

Copyright © 2016 Murphy, Guggenmos, Bundy and Nudo. This is an open-access article distributed under the terms of the Creative Commons Attribution License (CC BY). The use, distribution and reproduction in other forums is permitted, provided the original author(s) or licensor are credited and that the original publication in this journal is cited, in accordance with accepted academic practice. No use, distribution or reproduction is permitted which does not comply with these terms.